

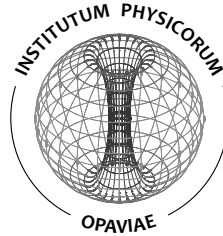
# Computer modelling of accretion processes in binary systems with black holes and neutron stars

Debora Lančová

DISSERTATION



Silesian University in Opava  
Institute of Physics



# Computer modelling of accretion processes in binary systems with black holes and neutron stars

Debora Lančová

Supervisor: doc. RNDr. Gabriel Török, Ph.D.  
Mentor: Prof. Marek Abramowicz, Ph.D.

DISSERTATION

OPAVA 2023



## Acknowledgment

*I would like to express my heartfelt gratitude to my advisors, colleagues, family, and friends for their unwavering support and guidance throughout my doctoral journey.*

*“So long and thanks for all the fish.”  
Douglas Noël Adams*



# Contents

## Preface

Full list of papers published in international journals . . . . .	2
List of proceedings and submitted papers . . . . .	2
Presentations at international conferences and invited seminars . . . . .	3

## Part I. Annotation

<b>Chapter 1. Introduction: Accretion onto compact objects</b> . . . . .	7
1.1. Black holes . . . . .	9
1.2. Binaries with compact objects . . . . .	12
1.3. Microquasars and their phenomenology . . . . .	13
<b>Chapter 2. Physics of accretion disks</b> . . . . .	21
2.1. Spherical accretion and the Eddington limit . . . . .	22
2.2. Accretion in strong gravity . . . . .	23
2.3. Black hole spacetimes . . . . .	27
2.4. Analytical models of accretion disks . . . . .	31
2.5. Overview of analytical models . . . . .	33
2.6. Modelling the accretion disk in microquasars . . . . .	38
<b>Chapter 3. GRRMHD simulation of sub-Eddington accretion</b> . . . . .	41
3.1. GRRMHD equations . . . . .	42
3.2. Numerical methods . . . . .	50
3.3. Running KORAL . . . . .	56
<b>Chapter 4. Puffy accretion disk</b> . . . . .	63
4.1. Simulating a sub-Eddington accretion disk . . . . .	63
4.2. Initial configuration for the Puffy disk simulations . . . . .	65
4.3. Properties of the puffy disk . . . . .	68
4.4. Observational picture . . . . .	71
<b>Chapter 5. Modelling the rapid time variability of XRBs</b> . . . . .	77
5.1. Fast time variability of black holes and neutron stars in XRBs . . . . .	78
5.2. Foundations of the orbital models of QPOs . . . . .	79
5.3. Marginally overflowing tori and the CT model . . . . .	82

5.4. Oscillations of accretion tori and estimations of parameters of compact objects . . . . .	84
5.5. Oscillations of accretion tori and QPO modulation . . . . .	86
<b>Summary</b> . . . . .	95
Overview of the collection of papers . . . . .	95
<b>List of Symbols</b> . . . . .	99
<b>List of Abbreviations</b> . . . . .	105
<b>References</b> . . . . .	107
<b>Part II. Collection of papers</b>	
<b>Paper 1: Puffy Accretion Disks: Sub-Eddington, Optically Thick, and Stable</b>	127
<b>Paper 2: Observational properties of puffy discs: radiative GRMHD spectra of mildly sub-Eddington accretion</b> . . . . .	135
<b>Paper 3: Spectra of puffy accretion discs: the <math>kynbb</math> fit</b> . . . . .	147
<b>Paper 4: Models of high-frequency quasi-periodic oscillations and black hole spin estimates in Galactic microquasars</b> . . . . .	155
<b>Paper 5: Simple Analytic Formula Relating the Mass and Spin of Accreting Compact Objects to Their Rapid X-Ray Variability</b> . . . . .	165
<b>Paper 6: Oscillations of non-slender tori in the external Hartle-Thorne geometry</b> . . . . .	175



# Preface

This dissertation is written as an annotated collection of selected papers presenting the results I achieved during my doctoral studies at the Institute of Physics of the Silesian University in Opava. I was a co-author of six papers published in prestigious international journals and four proceedings papers. In one paper and two proceeding papers, I was the leading author. One additional paper is submitted for peer review. For the annotation, I selected a total of 6 papers<sup>1</sup>.

The first part of the thesis is devoted to an overview of the topics addressed within the selected papers. Chapter 1 summarizes the astrophysical picture of accreting systems, focusing on the behaviour of X-ray binaries that exhibit effects of the general relativity in combination with radiation magnetohydrodynamic in a complex interplay. In Chapter 2, a more detailed introduction to the modelling of accretion disks in general relativity is given. Chapter 3 introduces general relativistic radiative magnetohydrodynamics, a method that enables the self-consistent modelling of magnetized fluids in general relativity, including the dynamical interaction with radiation and the exchange of energy and momentum between matter and radiation. Then, in Chapter 4, the puffy disk is introduced, an accretion disk model resembling an ultraluminous state of microquasars derived from the results of numerical simulations. Finally, the 5 chapter focuses on modelling X-ray variability and quasi-periodic oscillations using analytical models of accretion disks but employing an advanced description of the oscillations and outlining the implications of the complex modelling for observational data.

---

<sup>1</sup> Papers selected for the annotation are denoted by an asterisk symbol in the list of my publications.

## Full list of papers published in international journals

- Wielgus, M., Lančová, D., Straub, O., Kluźniak, W., Narayan, R., Abarca, D., Róžańska, A., Vincent, F., Török, G., & Abramowicz, M.; Observational properties of puffy discs: radiative GRMHD spectra of mildly sub-Eddington accretion (2022), *Mon. Not. R. Astron. Soc.*, 514, 780, DOI: [10.1093/mnras/stac1317](https://doi.org/10.1093/mnras/stac1317)\*
- Török, G., Kotrlová, A., Matuszková, M., Klimovičová, K., Lančová, D., Urbancová, G., & Šrámková, E.; Simple Analytic Formula Relating the Mass and Spin of Accreting Compact Objects to Their Rapid X-Ray Variability (2022), *Astrophys. J.*, 929, 28, DOI: [10.3847/1538-4357/ac5ab6](https://doi.org/10.3847/1538-4357/ac5ab6)\*
- Kotrlová, A., Šrámková, E., Török, G., Goluchová, K., Horák, J., Straub, O., Lančová, D., Stuchlík, Z., & Abramowicz, M. A.; Models of high-frequency quasi-periodic oscillations and black hole spin estimates in Galactic microquasars (2020), *Astron. Astrophys.*, 643, A31, DOI: [10.1051/0004-6361/201937097](https://doi.org/10.1051/0004-6361/201937097)\*
- Bakala, P., De Falco, V., Battista, E., Goluchová, K., Lančová, D., Falanga, M., & Stella, L.; Three-dimensional general relativistic Poynting-Robertson effect. II. Radiation field from a rigidly rotating spherical source (2019), *Phys. Rev. D*, 100, 104053, DOI: [10.1103/PhysRevD.100.104053](https://doi.org/10.1103/PhysRevD.100.104053).
- Lančová, D., Abarca, D., Kluźniak, W., Wielgus, M., Sądowski, A., Narayan, R., Schee, J., Török, G., & Abramowicz, M.; Puffy Accretion Disks: Sub-Eddington, Optically Thick, and Stable (2019), *Astrophys. J. Lett.*, 884, L37, DOI: [10.3847/2041-8213/ab48f5](https://doi.org/10.3847/2041-8213/ab48f5)\*
- De Falco, V., Bakala, P., Battista, E., Lančová, D., Falanga, M., & Stella, L.; Three-dimensional general relativistic Poynting-Robertson effect: Radial radiation field (2019), *Phys. Rev. D*, 99, 023014, DOI: [10.1103/PhysRevD.99.023014](https://doi.org/10.1103/PhysRevD.99.023014).

## List of proceedings and submitted papers

- Lančová, D., Yilmaz, A., Wielgus, M., Dovčiak, M., Straub, O., & Török, G.; Spectra of puffy accretion discs: the kynbb fit (2023), *Astronomische Nachrichten*, 344, e20230023, DOI: [10.1002/asna.20230023](https://doi.org/10.1002/asna.20230023)\*

- Šrámková, E., Matuszková, M., Klimovičová, K., Horák, J., Straub, O., Urbancová, G., Urbanec, M., Karas, V., Török, G., & Lančová, D.; Oscillations of fluid tori around neutron stars (2023), *Astronomische Nachrichten*, 344, e20220114, DOI: [10.1002/asna.20220114](https://doi.org/10.1002/asna.20220114).
- Matuszková, M., Klimovičová, K., Urbancová, G., Lančová, D., Šrámková, E., & Török, G.; Oscillations of non-slender tori in the external Hartle-Thorne geometry (2022), arXiv e-prints, arXiv:2203.10653, DOI: [10.48550/arXiv.2203.10653](https://doi.org/10.48550/arXiv.2203.10653)\*
- Lančová, D., Bakala, P., Goluchová, K., Falanga, M., De Falco, V., & Stella, L.; The study on behaviour of thin accretion disc affected by Poynting-Robertson effect (2017), *RAGtime 17-19: Workshops on Black Holes and Neutron Stars*, 127.
- Karas, V., Klimovičová, K., Lančová, D., Svoboda, J., Török, G., Matuszková, M., Šrámková, E., Šprňa, R., & Urbanec, M.; Timing of accreting neutron stars with future X-ray instruments: towards new constraints on dense matter equation of state (2023), submitted to *Contrib. Astron. Obs. Skalnaté Pleso*

## Presentations at international conferences and invited seminars

- RAGtime 20, Opava, Czech Republic; October 2018; *GRRMHD simulation of thin accretion disk stabilized by magnetic field*, talk
- Heraeus Seminar on Accretion in Strong Gravity, Wilhelm und Else Heraeus Stiftung, Bad Honnef, Germany; February 2019; *Global GRRMHD simulation of thin accretion disk*, talk
- 12th Integral Conference, Geneva, Switzerland; February 2019; *Global GRMHD simulation of thin accretion disk*, poster
- RAGtime 21, Opava, Czech Republic; September 2019; *Puffy accretion disks: sub-Eddington, optically thick, and stable*, talk
- Future of X-ray Timing 2019, Amsterdam, Netherlands; October 2019; *Global GRRMHD simulation of thin accretion disk*, talk
- BHI colloquium, Harvard University, USA; December 2019; *Puffy accretion disks: sub-Eddington, optically thick, and stable*
- RAGtime 23, Opava, Czech Republic; September 2021; *Puffy accretion disk: observational properties and inner structure*, talk

- 9th Microquasar Workshop, Cagliari, Italy; September 2021; *Puffy accretion disk: sub-Eddington, optically thick, and stable*, poster
- Seminar, NORDITA, Stockholm, Sweden; November 2021; *Puffy accretion disks: new results and plans*
- Seminar, Institute of Astronomy, Cambridge University, Cambridge, United Kingdom; November 2021; *Global GRRMHD simulation of stable, optically thick sub-Eddington accretion disk – the Puffy disk*
- Seminar, INAF Sicily, Palermo, Italy; March 2022; *Puffy accretion disk: sub-Eddington, optically thick, and stable*
- Pharos conference, Rome, Italy; May 2022; *Broadened iron lines exhibited by accreting relativistic compact object*, poster
- XMM-Newton meeting, Black hole accretion under the x-ray microscope, Madrid, Spain; June 2022; *Observational properties of puffy accretion disk*, poster
- Ten Years of High-Energy Universe in Focus - NuSTAR 2022, Cagliari, Italy; June 2022, *Numerical model of a stable sub-Eddington accretion disk – the puffy disk*, talk
- COSPAR 2022, Athens, Greece; July 2022; *Observational properties of puffy accretion disk*, talk
- 31st Texas Symposium on Relativistic Astrophysics, Prague, Czech Republic; September 2022; *GRRMHD simulation of sub-Eddington accretion onto stellar mass black hole*, talk
- RAGtime 23, Opava, Czech Republic; October 2022; *GRRMHD simulation of sub-Eddington accretion onto stellar mass black hole*, talk
- Third Athena Scientific Conference, Barcelona, Spain; November 2022; *Observational properties of puffy accretion disk*, poster
- Timescales in Astrophysics Conference, Abu Dhabi, UAE; January 2023; *Timescales of BH accretion disks*, talk/poster
- HEAD meeting, Waikoloa Village, Hawaii, USA, March 2023; *Puffy accretion disks: sub-Eddington, optically thick, and stable*, poster
- IBWS 2023, Karlovy Vary, Czech Republic; May 2023; *Puffy accretion disks: sub-Eddington, optically thick, and stable*, poster

Part I

Annotation



## Chapter 1

# Introduction: Accretion onto compact objects

Compact objects such as black holes (BHs) or neutron stars (NSs) power some of the most energetic sources observed in the Universe. By studying these sources across different wavelengths, various parameters of their central engines have been determined through different methods and techniques, including multi-messenger astronomy. The emission of electromagnetic radiation from these objects spans across a wide range of energies, and modern observatories, both on Earth and in space, cover nearly the entire electromagnetic spectrum (see Figure 1.1).

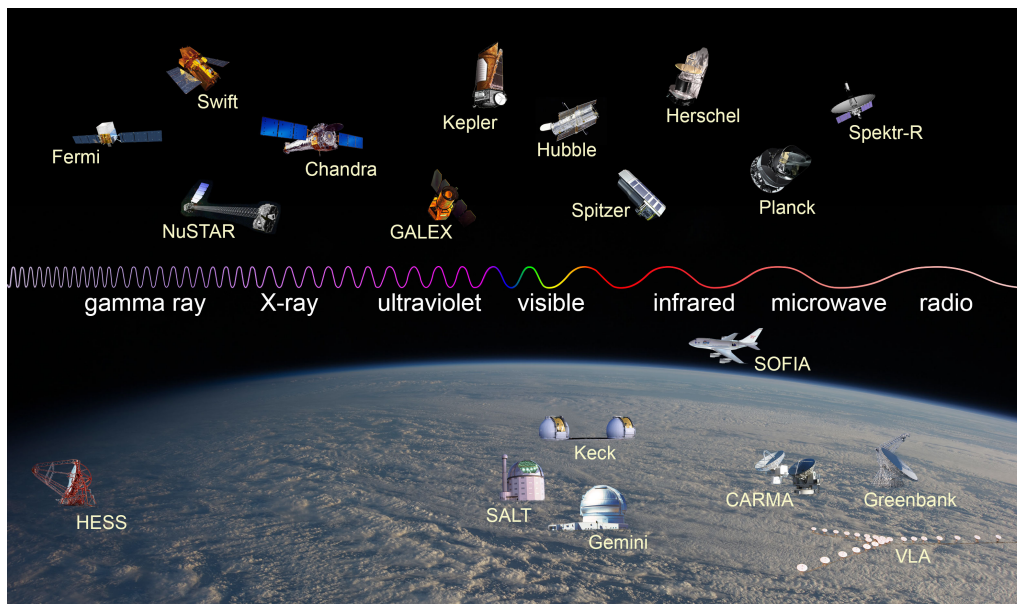


**Figure 1.1.** Space and land-based observatories from the NASA fleet, covering almost the whole electromagnetic spectrum (NASA).

A broad spectrum of accreting compact object sources can be observed and studied thanks to these advanced facilities, even though they are often spatially unresolved and appear as point sources. These multi-wavelength observations provide valuable insights into the composition, variability, and spectral properties of these sources. To date, over 500 Galactic X-ray binaries (XRBs) containing a compact object have been discovered (Avakyan et al. 2023; Neumann et al. 2023), and even more extragalactic sources, such as BHs in the centres of other galaxies, isolated NSs wandering across the Galaxy (Treves et al. 2000), (extra)galactic NSs or intermediate mass BHs, e.g., in the ultra-luminous X-ray sources (ULXs, Kaaret et al. 2017), and isolated BHs only observed while consuming a random passing-by object as a tidal disruption event (TDE, Hills 1975), and many others.

In our Galaxy, the brightest sources are expected to contain compact objects. Among them, the NS systems are usually easily distinguishable due to the observation of periodic pulsations or by the occasional occurrence of thermonuclear bursts, which are not observed in BH sources. The pulsations arise from the rotation of the NS and the misalignment between its rotational and magnetic axes (see Figure 1.2). NS systems undergo a complex life cycle, from being bright in the radio band to bright in the X-ray band, dimming down and being reborn, and occasionally emitting fast and intense X-ray bursts. Fast time variability, often manifested as high-frequency quasi-periodic oscillations (QPOs), is also more prominent in NS sources compared to BH sources, see Chapter 5, Török et al. (2022), and references therein.

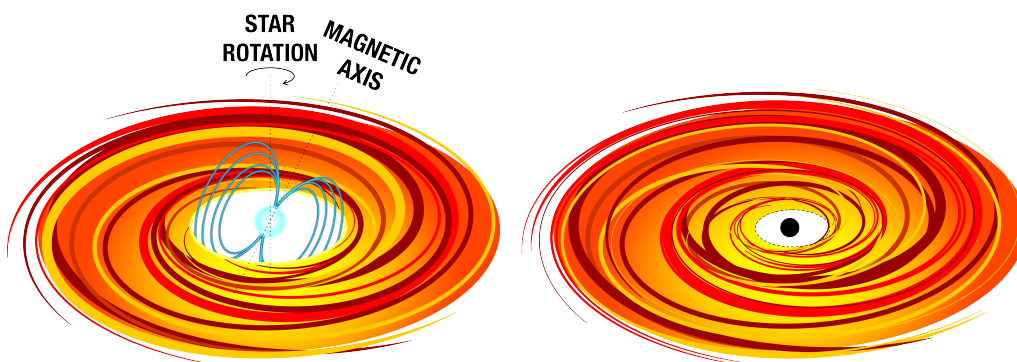


**Figure 1.2.** Accretion disk in a NS system (*left*) with the disk truncated at the magnetospheric radius due to the presence of a strong magnetic field, and in a BH system (*right*) extending all the way to the innermost stable circular orbit (dashed line).



## 1.1. Black holes

Since the discovery of the first BH systems in the 1970s ([Webster & Murdin 1972](#)), they have become the focus of numerous observation campaigns across the electromagnetic (EM) spectrum. BHs have served as laboratories for testing fundamental theories and expanding our understanding of the Universe. Explorations of the BH systems have also revealed their crucial role in galaxy formation and evolution. They have helped to understand processes that govern the behaviour of matter and energy in the most extreme environments.

BHs exist across a wide range of masses in the Universe, spanning from very light stellar-mass BHs with mass  $M \sim 10 M_{\odot}$  (where  $M_{\odot}$  is the solar mass) to supermassive BHs in the centres of galaxies with mass up to  $10^{10} M_{\odot}$  ([Dullo et al. 2021](#)). Despite the enormous range of masses, many properties of BH systems are remarkably similar. They are observed due to the accretion of matter from their surroundings, often appearing as highly luminous sources, particularly in the X-ray band. BH systems can also produce jets, collimated fast outflows originating in the polar regions, which are bright in radio wavelengths. In specific orientations, the jets may be Doppler-boosted in the observer's direction, which makes the system even more luminous.

In the case of BHs, the source of the radiation is not the compact object itself

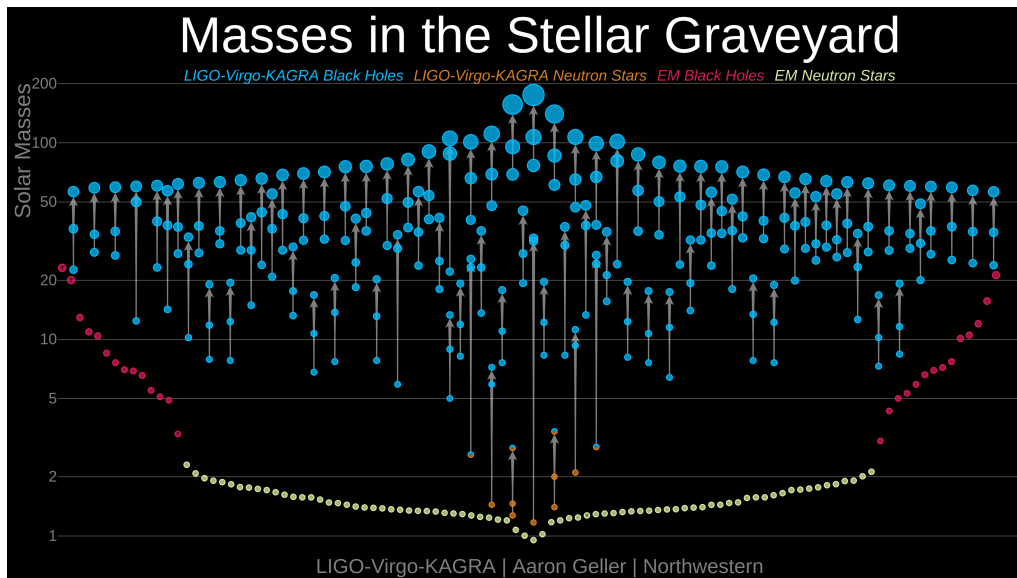


**Figure 1.3.** Range of masses of known BHs and NSs observed in the EM spectrum or in the GW. Some sources are still to be confirmed, denoted with question marks. Visualization: LIGO-Virgo-KAGRA / Aaron Geller / Northwestern.

but rather its immediate surroundings. When the material with a non-zero angular momentum falls onto a BH, it forms an accretion disk that can extract and radiate away a significant portion, up to 42 %, of the rest-mass energy from the infalling matter. This process is one of the most efficient mechanisms for converting matter into radiation, second only to annihilation. The presence of a compact object and the extreme gravitational curvature of spacetime in its vicinity profoundly impact the behaviour of matter, leading to observable properties that differ significantly from those expected in a flat spacetime. As a result, the effects of general relativity (GR) are often crucial for an accurate description of accretion and other processes near compact objects ([Bardeen et al. 1972](#); [Frank et al. 2002](#); [Lynden-Bell 1969](#); [Salpeter 1964](#)).

### 1.1.1. Supermassive black holes

Supermassive BHs are commonly found at the centers of galaxies, a fraction of which (about 1 %) accrete matter at very high rates from their surroundings environment. Depending on the density of material accumulated in their vicinity, some of these BHs can release a tremendous amount of energy in the form of radiation from the accretion disk and powerful jets from the polar regions. These objects are often referred to as active galactic nuclei (AGN, [Ambartsumian 1958](#)).

The discovery of AGN was closely linked to the observation of quasars (quasi-stellar objects). Quasars were initially unidentified sources with extremely high luminosity and peculiar spectral properties that did not contain the usual spectral lines of known elements ([Fath 1909](#)). This posed a significant puzzle for astronomers and physicists for quite some time until it was realized that these lines corresponded to the conventional spectral lines of hydrogen, helium, and other elements but heavily redshifted to much lower frequencies. This redshift indicated that the sources were extremely distant and located in an expanding Universe ([Schmidt 1963](#)).

The presence of standard spectral lines raised a new question: How can a source be so luminous when also exhibiting fast variability that suggests a relatively compact size? The answer came in the form of accretion onto a compact object in an AGN. No other process could steadily release such an enormous amount of energy within such a small volume. At the same time, more luminous sources were found – blazars and Seyfert galaxies, with similar properties to quasars. Blazars are believed to be AGN observed on-axis, with their jets pointing directly toward Earth ([Urry & Padovani 1995](#)).

### 1.1.2. Stellar mass black holes

Another family of BHs are the stellar-mass (or low-mass) BHs, with mass ranging from a few to tens of  $M_{\odot}$ . These BHs are formed during the final stage of the life of a very massive star ( $M \gtrsim 40M_{\odot}$ ) in supernova explosions. If a stellar-mass BH is a part of a binary system and accretes matter from its companion star, the system can be easily observed, particularly within our own Galaxy, since it is highly luminous.

Stellar-mass BH systems serve as excellent laboratories for testing the effects of GR in strong gravitational fields, studying the behaviour of matter under extreme conditions, and other aspects of modern astrophysics, including alternative theories of gravity. As such, they have the potential to advance our understanding of fundamental physics and contribute to the development of new theories that can explain some of the most enigmatic phenomena in the Universe.

The mass range of the stellar mass BHs is theoretically determined by the Tolman–Oppenheimer–Volkoff limit on one side, which sets the maximum mass on a NS at approximately  $3M_{\odot}$  (Bombaci 1996; Rhoades & Ruffini 1974), which is considered to be the minimal mass of a BH of stellar origin. The upper mass limit for BHs created through supernova explosions is proportional to the maximum mass of the progenitor star, yielding a mass limit of around  $80M_{\odot}$  (see,

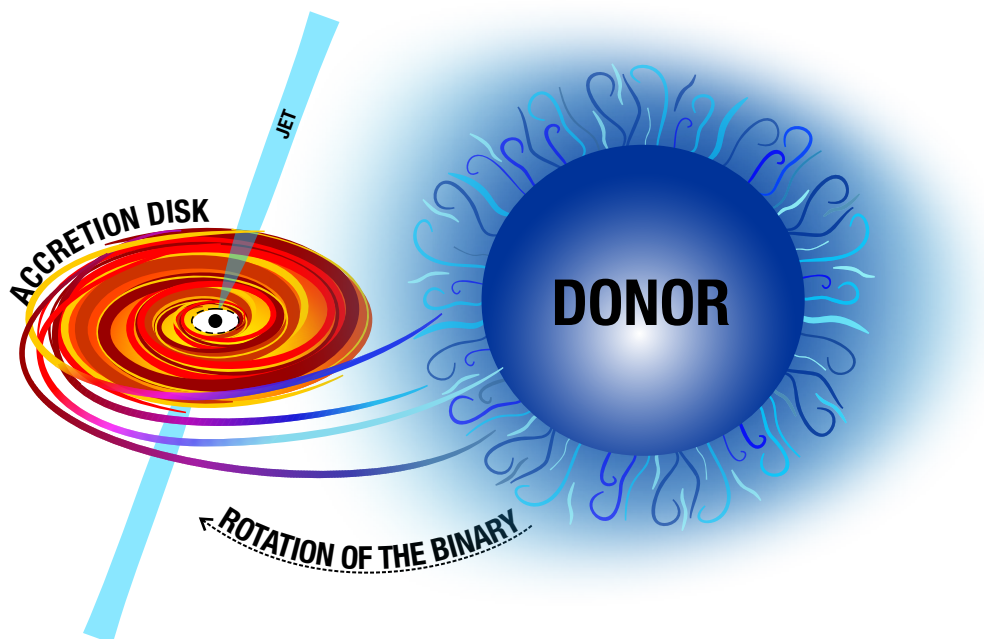


Figure 1.4. Illustration of typical HMXB in a microquasar source with radio loud jet.

e.g., [Belczynski et al. 2010](#)) and references therein). The upper limit existence follows from the fact that supernova explosions of very massive stars are more sensitive to the pair instability, and no remnant is left behind. However, the gravitational wave (GW) observations ([Abbott et al. 2016](#)) showed that the mass range of BHs (and NSs as well) is much broader than obtained through the EM observations since BHs can also be formed through mergers of less massive objects, see Figure 1.3.

## 1.2. Binaries with compact objects

XRBs are one of the brightest sources in our Galaxy. A typical XRB consists of a compact object and a companion star that transfers material onto the compact object ([Remillard & McClintock \(2006\)](#) and references therein). This material forms an accretion disk, and as it spirals inward, it liberates gravitational energy, leading to the emission of the X-rays in the innermost regions closest to the compact objects.

XRBs can be divided into two categories based on the mass of the companion and the mechanism of mass transfer: High mass and low mass XRBs (HMXBs and LMXBs, [Bradt & McClintock 1983](#)). The essential properties of both are summarized in Table 1.2, and see also illustration in Figures 1.4 and 1.5. A key parameter in these systems is the mass of the *donor* ( $M_D$ ), from which the material is transported onto the compact object, known as the *accretor* of mass  $M_A$ .

Type	Companion	Mass ratio ( $M_D/M_A$ )	Orbital period	Mass transfer mechanism	Example	Observed in
<b>HMXB</b>	Supergiant (O-B)	> 1	days	Wind accretion	Cygnus X-1	Optical, UV, X-rays
<b>LMXB</b>	Main sequence star	< 1	hours	Roche lobe overflow	GRS 1915+105 (BH) 4U 0614+091 (NS)	X-rays

**Table 1.1.** Typical properties of LMXBs and HMXBs.

In LMXBs, a low-mass donor star fills its Roche lobe and transfers material onto a companion compact object through the  $L_1$  point. Suppose the LMXB originates from the evolution of a binary star (as opposed to dynamical interactions of two or three bodies in dense clusters). In that case, the angular momentum of the BH or NS and the accretion disk will likely be parallel to that of the binary system since it was accreted from the disk matter over millions of years of co-evolution of both components.

LMXBs predominantly emit radiation in the X-ray band and are relatively faint in other wavelengths. Due to the source of X-rays lying deep in the strong

gravitational field of the compact object, studying LMXBs provides an opportunity to obtain valuable insights into the properties and behaviour of matter under extreme gravitational conditions.

### 1.3. Microquasars and their phenomenology

Jets from the central regions are frequently observed in the XRBs, which resemble scaled-down quasars. As a result, these systems are often referred to as microquasars. (Mirabel et al. 1992).

Microquasars are primarily observed in X-rays, and when jets are present, they can also be detected in the radio wavelengths. The comparison of observational data obtained from these two bands, which originates from very different physical processes, provides valuable insights into the extreme environment surrounding compact objects. It makes the microquasars a popular target of observations and a hot research topic, see Méndez et al. (2022).

BHs microquasars are known to undergo irregular cycles of outbursts and quiescent periods (see Figure 1.8), characterized by distinct spectral and timing properties of the observed signal (Done et al. 2007; Tetarenko et al. 2016). During the quiescent phase, which can last for years, the luminosity of the

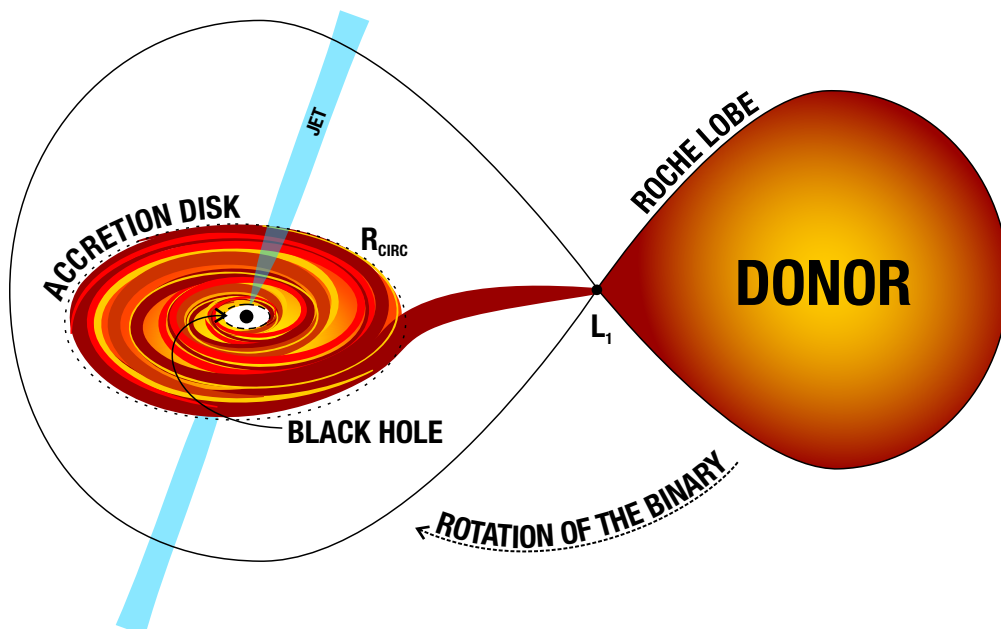


Figure 1.5. Illustration of typical LMXB in a microquasar source with a radio-loud jet.

source is extremely low, making some sources undetectable. However, during an outburst, an active period of very high luminosity lasting on average for 100 days (Tetarenko et al. 2016), the spectral and timing properties change rapidly. The evolution of the outburst is often represented by a  $q$ -shaped curve on a hardness-intensity diagram (HID), where the X-ray intensity is plotted against the observed X-rays hardness ratio (typically  $(4 - 10)/(2 - 4)$  keV). The HID traces the X-ray luminosity and energy spectrum variations throughout the outburst; see Figure 1.8.

This behaviour is characteristic for all known microquasars (most of which are BH LMXBs), regardless of the donor’s mass or accretion regime, even in systems with a NS instead of a BH at the centre (Muñoz-Darias et al. 2014). NS systems are generally more persistent, with relatively high X-ray luminosity, and do not exhibit the transient behaviour typical for BH microquasars. However, several transient NS systems have been observed.

The evolution of transient NS LMXBs during an outburst appears to be more complex than that of BHs systems, likely due to the presence of a solid surface and an anchored magnetic field. Some of the spectral states the NS systems exhibit are similar to those of BH systems (Van der Klis 2006), although the curve on the HID differs. In the case of NS systems, a colour-colour diagram (CCD) is often used instead of the HID, which shows the ratio of harder and softer counts against each other.

NS systems can be classified as Z sources or Atoll sources (Hasinger & van der Klis 1989) based on their luminosity and shape on the CCD, and a few sources have been observed to transition between these two states (Lin et al. 2009; Seward & Charles 2010), see Figure 1.7.

The outburst behaviour is driven by fundamental physical processes occurring in the accretion disk, leading to state transitions regardless of environmental

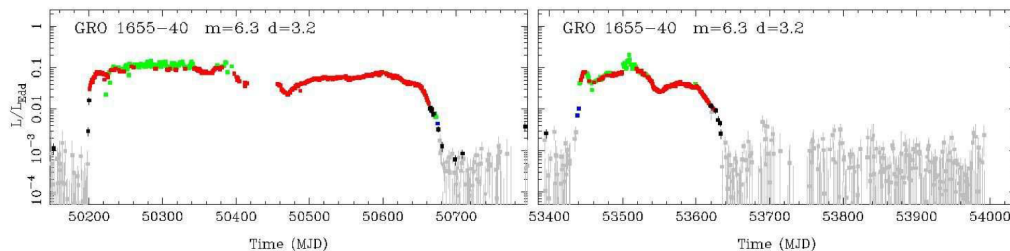


**Figure 1.6.** Observed light-curve of typical Galactic microquasar GRO 1655-40 showing two episodes of luminous outburst (colours) and quiescent (grey) periods, adopted from Done et al. (2007).

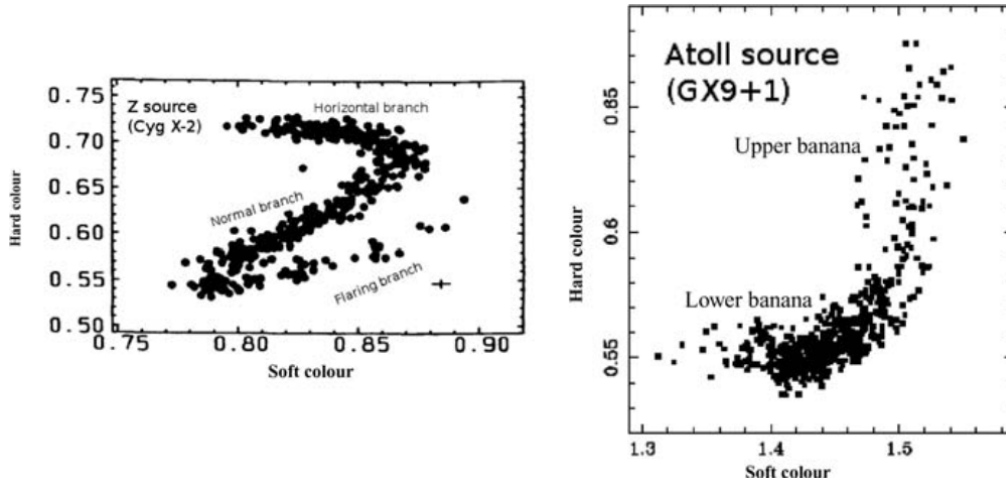


**Figure 1.7.** CCD for a Z source Cygnus X-2 (left) and atoll source GX9+1. The different spectral states recognized in both kinds of sources are labelled, adapted from [Seward & Charles \(2010\)](#).

factors. Therefore, modelling the outbursts and the accretion disk during state transitions is crucial for understanding the physics of accretion.

### 1.3.1. Spectral states of black hole microquasars

Several spectral states can be distinguished during an outburst in BH systems, corresponding to different accretion regimes. The state transitions between these states strictly follow the order shown in Figure 1.8, meaning that the system must go through the hard and intermediate states before reaching the soft state ([Miyamoto et al. 1995](#)). These spectral states are commonly classified into five categories as follows:

- **Hard state:** In the hard state, the majority of emitted photons are in the hard X-ray band, and spectral shape corresponds to a combination of low-temperature thermal emission and strong non-thermal processes. This state can be modelled by a truncated thin disk, with a hot geometrically thick optically thin disk formed in the inner region. The photon energy distribution follows a power law with a photon index typically ranging from 1.5 to 2 ([Zdziarski et al. 1996](#); [Życki et al. 1999](#)), which is usually modelled as upscattering of the thermal seed photons from the truncated disk in the inner optically thin disk or a corona. The system can remain in the hard state for weeks. Strong variability is observed in this state, especially as a red noise component plus low frequency (LF) QPOs.

- **Intermediate states:** From the hard state, the system rapidly transitions into intermediate hard and intermediate soft states, distinguished by their timing properties (Van der Klis 2006). The frequency of QPOs typically shifts to higher values as the system moves from the intermediate hard state to the intermediate soft state (Wang et al. 2013), suggesting that the inner edge of the accretion disk moves inward.
- **Ultra-luminous state:** In some sources, an extremely luminous state is observed (Motta et al. 2021), characterized by a thermal spectrum with a strong, high-energy tail. This state can be modelled, e.g., using the puffy accretion disk (Lančová et al. 2019; Wielgus et al. 2022).
- **Soft state:** In the soft state, the peak of the spectral energy distribution (SED) is in the soft X-ray band, and the shape corresponds to a multi-colour thermal spectrum with a high-energy tail. The luminosity is high, particularly in the soft X-ray band (Miyamoto et al. 1995). This state is modelled as the thermal emission from a geometrically thin optically thick disk extending to the innermost stable circular orbit (ISCO), with a Comptonizing corona responsible for the high-energy tail. The time variability is significantly reduced in the soft state.

An integral aspect of spectral state modelling is a hot corona, responsible for the up-scattering of photons to very high energies. The geometry of the corona

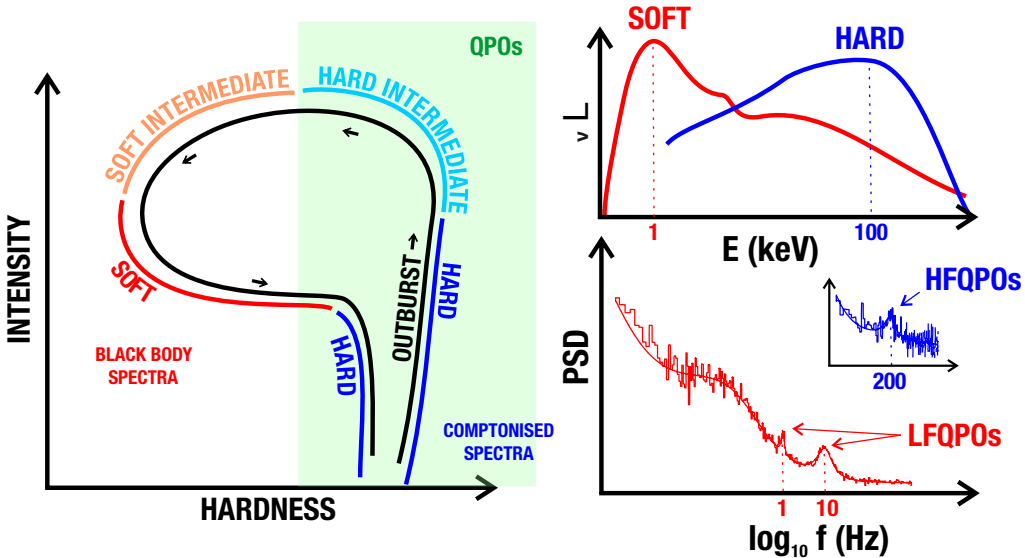


Figure 1.8. The  $q$  curve in the HID of a BH microquasar during an outburst (left), spectral and timing properties (right). Data for the spectra and PSD from Gierliński et al. (1999) and Motta et al. (2022)



has been the subject of extensive discussion in microquasar astrophysics, with preferred models including the lamp-post, sandwich, or spherical corona models (Bambi 2017). However, recent measurements of polarization angles from XRB observations have placed additional constraints on the corona's geometry (Podgorny et al. 2023).

During a complete outburst, the source undergoes a sequence of spectral states, starting from the hard state and transitioning through the intermediate hard and intermediate soft states before reaching the soft state. Then it transitions back to a less luminous hard state and eventually returns to quiescence<sup>1</sup>. In some cases, an outburst may not progress beyond the hard or intermediate hard state, as was observed, e.g., in 2019, in a newly discovered XRB MAXI J1348-630 (Alabarta et al. 2021).

### 1.3.2. Timing properties of XRBs

XRBs exhibit variability across a wide range of timescales in all wavelengths, with the fastest variation reaching frequencies of approximately 1 kHz in X-rays. This subsection focuses on rapid variability, particularly on the QPOs, which are observed as strong, broad peaks in the power spectral density (PSD) diagram, obtained as a result of Fourier analysis of observed X-ray light curves (see Figures 1.9 and 1.8). The properties of QPOs evolve in conjunction with spectral state transitions in the accretion disk.

QPOs originate in the innermost and hottest regions of the accretion disk. However, the exact physical mechanism behind QPOs still needs to be fully understood, although several theoretical models have been proposed (a short overview of selected models can be found in Chapter 5). QPOs provide valuable insight into the accretion processes in binary systems. For instance, the frequency and amplitude of the QPOs can be used to estimate the mass and spin of a compact object (Goluchová et al. 2019; Kotrlová et al. 2020; Motta et al. 2014; Török et al. 2022) or, in the case of a NS, it can put constraints on the dense matter equation of state, (Urbancová et al. 2019; Urbanec et al. 2013), as well as the size and structure of the accretion disk, and the properties of the surrounding gas. Thus, QPOs can serve as a valuable tool for studying the physics of extreme environments.

---

<sup>1</sup>Originally, these states were labelled as soft/high and hard/low, but this originated in the early stages of the X-ray astronomy when the observatories were unable to detect the hard X-rays emitted during the hard state. It is now understood that the luminosity in both states can be similar.

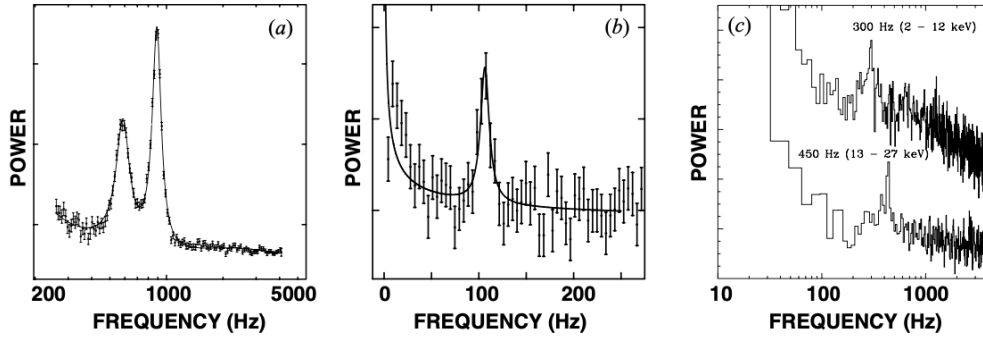


**Figure 1.9.** A typical PSD diagram of a NS source, showing the kHz QPOs (*left*), and LF QPOs (*middle*), and the HF QPOs from a BH source (*right*). The peaks in the high frequencies are typically weaker in BHs XRBs than those of NS sources. From [Van der Klis \(2006\)](#).

QPOs are observed across a wide range of frequencies, from mHz to kHz. QPOs are typically classified based on their characteristic frequencies and the type of source in which they are observed. The most common classification distinguishes low-frequency (LF) and high-frequency (HF) QPOs. LF QPOs in BH systems are usually labelled as Type A, B, or C, while in NS systems, they are referred to as HBO (horizontal branch oscillations), NBO (normal branch oscillations), and FBO (flaring branch oscillations) ([Casella et al. 2005](#); [van der Klis 2004](#)). HF QPOs are primarily associated with BH sources, whereas in NS sources, they are commonly known as kHz QPOs, or the twin-peak QPOs. Observed frequencies of HF QPOs can be directly linked to the characteristic frequencies of orbital motion in the innermost areas of an accretion disk surrounding a compact object, where the GR effects govern the dynamics

Another intriguing phenomenon is the burst oscillations observed in bursting NS systems. These oscillations have frequencies that closely match the rotational frequency of the NS itself. They are observed in a few sources exhibiting coherent pulsations due to magnetospheric accretion. Moreover, QPOs with mHz frequencies were also discovered, likely linked to unstable nuclear reactions on the surface of NS ([Revnivtsev et al. 2001](#)).

Figure 1.9 demonstrates the significant differences between BH and NS HF QPO signals. However, there are also many similarities. The kHz QPOs in NS sources are typically observed as two strong simultaneous peaks with strongly correlated lower and higher frequency variations. These peaks are distinct and prominent, clearly rising above the noise level. In contrast, HF QPOs in BH systems are more challenging to observe and have been detected as simultane-

---

ous pairs in only a few cases. In the case of the NS sources, the properties of observed QPOs can be explained by the source of oscillations connected to the boundary layer on a NS surface and modulation of its luminosity by oscillations of accreting structures in the innermost region close to the NS affected by the quadrupole momentum of the NS (Matuszková et al. 2022). In BH sources, the absence of a boundary layer results in matter from the innermost regions of the disk drifting toward the event horizon, making it challenging for emitted radiation to escape the powerful gravitational pull.



## Chapter 2

# Physics of accretion disks

Apart from annihilation, accretion is the most energetic process in the universe, capable of releasing up to 42% of the binding rest-mass energy from the accreting material in the form of EM radiation. Due to the extremely high temperatures in the innermost area of the disk, which can reach up to  $10^8$  K, it is mainly in the X-ray band. Consequently, the study of accretion is a hot topic in high-energy astrophysics, particularly when it involves sources with compact objects, especially BHs.

Accretion plays a crucial role in understanding the mechanisms driving the growth of celestial objects and is an essential process in studying the formation and behaviour of BHs. However, accretion physics is a complex research field requiring various physical effects from different disciplines. These include plasma physics, hydrodynamics, electrodynamics, and GR. Furthermore, implementing advanced computational and numerical methods is essential for the realistic modelling of accreting systems.

In an accretion disk, the material experiences strong gravitational forces from the central object, and the presence of a strong magnetic field can significantly influence the disk's structure, dynamics, and the generation of powerful jets observable in radio wavelengths. Moreover, nuclear physics is crucial for understanding the behaviour of matter at high densities and temperatures. Finally, GR is necessary to accurately describe the behaviour of matter in the strong gravitational field near the central compact object, accounting for relativistic effects such as frame dragging and gravitational lensing.

Incorporating these effects into a realistic model of an accretion disk presents a major challenge that requires a multi-disciplinary approach and advanced computational techniques. However, the potential rewards are significant, as a deeper understanding of accretion disks can provide valuable insights into the formation and evolution of BHs and the behaviour of matter under extreme conditions. This chapter introduces analytical models of accretion within the framework of GR, with a specific focus on accretion disks in galactic XRBs.

## 2.1. Spherical accretion and the Eddington limit

The simplest accretion case is the spherical one, also known as the Bondi accretion, first described by Bondi (1952). It calculates the spherically symmetric accretion of a homogeneous gas cloud surrounding a gravitating body. Further studies by Parker (1958) investigated the spherically symmetric outflow, describing phenomena such as solar winds.

The description of spherical accretion allows the definition of several fundamental characteristics that can also describe general properties of accretion flows in different regimes. One such characteristic is the mass accretion rate, denoted as  $\dot{M}$ , representing the rate at which material falls onto the central object. The mass accretion rate is proportional to the radial velocity of the gas and its density, given by  $\dot{M} \propto -v^r \rho$ , where the negative sign indicates that a positive value of  $\dot{M}$  represents accretion, while a negative value represents outflow.

Assuming a steady spherical accretion onto a radiating body, a maximal value of the luminosity of the central object can be established, at which the radiation pressure balances the gravitational pull on the infalling matter. Beyond this critical luminosity, spherical accretion cannot take place. This limit is the Eddington luminosity, one of the most essential concepts in astrophysics. The exact value can be derived considering a radiating body of mass  $M$  and luminosity  $L$ , surrounded by a cloud of fully ionized hydrogen gas. Then the effective cross-section is taken as the Thomson cross-section  $\sigma_T$ , and the proton mass  $m_{p^+}$  is used as the mass of the hydrogen atoms. By balancing the radiation force on each electron at a radius  $r$ ,

$$F_r = \frac{\sigma_T L}{4\pi c r^2} \quad (2.1)$$

with the gravitational pull on a hydrogen core at the same radius,

$$F_g = \frac{GMm_{p^+}}{r^2}, \quad (2.2)$$

where  $c$  is the speed of light and  $G$  the gravitational constant, we can derive the value of the Eddington luminosity  $L_{\text{Edd}}$  using the electron scattering opacity  $\kappa_{es} = \sigma_T/m_{p^+}$ , as

$$L_{\text{Edd}} = \frac{4\pi c GM}{\kappa_{es}} = 1.3 \times 10^{38} \left( \frac{M}{M_\odot} \right) \text{ erg} \cdot \text{s}^{-1}. \quad (2.3)$$

From this value, a critical  $\dot{M}_{\text{Edd}}$  can be derived,

$$\dot{M}_{\text{Edd}} = \frac{L_{\text{Edd}}}{\eta c^2}, \quad (2.4)$$

where  $\eta$  is the energy conversion efficiency. In the case of the BH accretion,  $\eta$  can be derived from the specific angular momentum of the BH, reaching values up to  $\eta = 0.42$  for Keplerian rotation of the disk and maximally rotating BH. It is common to use  $\eta = 1$ , which is also used in this thesis.

However, the GR corrections are neglected in these calculations. The strong gravity influences the photon trajectories, which leads to the formation of an Eddington capture sphere, studied in [Stahl et al. \(2012\)](#). Effects of the radiation from a compact star on the motion of a test particle were also studied in [De Falco et al. \(2019\)](#) and for a rotating star in [Bakala et al. \(2019\)](#)<sup>1</sup>.

Although the  $L_{\text{Edd}}$  derivation is based on simple assumptions, the value is also valid for disk accretion. Nevertheless, the accretion can also become super-Eddington in the case of geometrically thick accreting tori ([Abramowicz et al. 1978](#); [Jaroszyński et al. 1980](#)), as discussed in Section 2.5.

## 2.2. Accretion in strong gravity

BHs are very simple objects, as Chandrasekhar said in his famous monograph [Chandrasekhar \(1998\)](#). They can be described by only three parameters: mass  $M$ , specific angular momentum (spin)  $a$ , and electric charge  $Q$ . As a result, simple units can be used to describe BH spacetime across the whole range of masses, such as the gravitational radius,  $r_g = GM/c^2$ , for length and  $t_g = r_g/c$  for time. These geometrized units will be used from here forward, laying  $G = c = 1$ .

Parameters describing the accretion flow can be written in simple forms using this units,

$$m = \frac{M}{M_{\odot}} \quad \dot{m} = \frac{\dot{M}}{\dot{M}_{\text{Edd}}} \quad r = \frac{r_*}{r_g}$$

where  $M$  is the mass of the compact object,  $\dot{M}$  is the mass-accretion rate, and  $r_*$  is the radius in cm.

---

<sup>1</sup> I was a co-author of these two papers; however, they are not a part of the collections of papers commented in this thesis, since their topic is far from the main subject of this thesis.

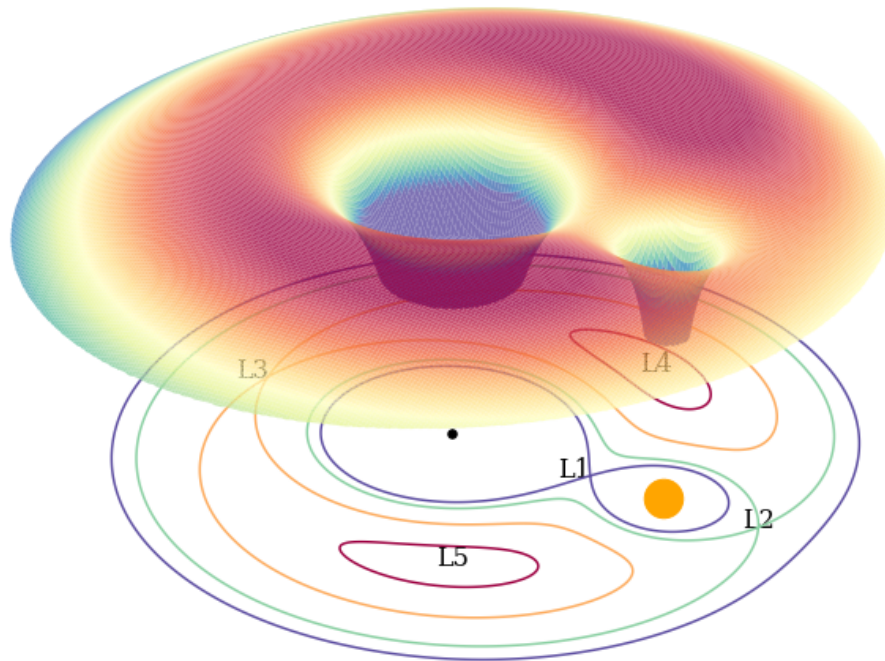


**Figure 2.1.** Roche potential of two orbiting bodies with a mass ratio  $q = 0.1$ , representing a BH and a main sequence star in LMXBs. The bottom part of the figure shows the contours of the Roche potential, with the Lagrange points  $L_1$ - $L_5$  highlighted. The potential wells are cut off to enhance the bottom part's visibility.

In a LMXB, an accretion disk forms when a companion star fills up its Roche lobe (see Figure 2.1), and its material starts to flow onto the compact object through the  $L_1$  point. A Roche lobe is the largest closed equipotential surface of the Roche potential, which combines the effects of gravitational forces acting on components of a binary system, the gravitational pull and centrifugal force. The companion can fill the Roche lobe during the final stage of life of the companion star as it depletes its hydrogen reserves and begins burning heavier elements like helium, or if the orbit shrinks due to the binary evolution.

The matter from the companion object has a non-zero angular momentum, and the conservation laws prevent it from radially falling into the centre. Instead, it forms a disk-like structure in the rotational plane of the binary system. Within this accretion disk, thermal and viscous processes lead to the angular momentum transport outward, gradually causing the material to lower its orbit until it reaches the inner edge of the disk. Nevertheless, the situation is more complex in the case of a NS disk and will be discussed below.

At the  $L_1$  point, the material from the companion star is injected into the



potential well of the accretor with high angular momentum and settles gradually into the lowest energy state, which corresponds to a Keplerian circular orbit with the same angular momentum as the gas had when it passed through the  $L_1$  point. The radius of this orbit, known as the circularization radius  $R_{\text{circ}}$ , can be easily derived from the mass ratio  $q$  and the separation  $s$  of the binary system as

$$R_{\text{circ}}/s = (1 + q) (0.5 - 0.227 \log q)^4, \quad (2.5)$$

using a fitted formula for the location of the  $L_1$  point. The  $R_{\text{circ}}$  corresponds to the outer edge of an accretion disk (Frank et al. 2002), see also Figure 1.5.

### 2.2.1. Inner edge of an accretion disk

Accretion disks around standard stars or white dwarfs are expected to extend all the way to the surface of the central object. In the case of compact objects, the accretion disk is strongly influenced by strong gravitational and magnetic fields and fast rotation. In NS systems, the disk can reach the surface of the NS under certain conditions, and it is typically truncated further away due to interactions with the NS's magnetic field.

Three important radii in NS systems determine the position of the inner edge of the accretion disk and the accretion regime. The position of these radii depends on the parameter of the NS itself and the accretion flow. These radii are the light cylinder radius  $r_{\text{lc}}$ , the corotation radius  $r_{\text{co}}$ , and the magnetospheric radius  $r_{\text{mag}}$ . Accretion can only occur if the following conditions are met:  $r_{\text{mag}} < r_{\text{co}} < r_{\text{lc}}$ , see Figure 2.2.

The three radii can be derived as Frank et al. (2002)

$$r_{\text{lc}} = (4.709 \times 10^{10} \text{ cm}) P, \quad (2.6)$$

$$r_{\text{co}} = (1.5 \times 10^8 \text{ cm}) m^{1/3} P^{2/3}, \quad (2.7)$$

$$r_{\text{mag}} = (2.9 \times 10^8 \text{ cm}) m^{-1/7} \mu_{30}^{4/7} \dot{m}^{-2/7}, \quad (2.8)$$

where  $P$  is the rotation period of the NS with mass  $m$ . The expression for the  $r_{\text{mag}}$  is given for a dipole magnetic field on the NS surface and other assumptions.  $\mu_{30}$  is there the magnetic moment  $\mu = \frac{B_*}{R_*^3}$  in the units of  $10^{30} \text{ G} \cdot \text{cm}^3$ ,  $B_*$  is the magnetic field strength at the surface of NS, and  $R_*$  is the star's radius. The  $r_{\text{mag}}$  corresponds to the location where the ram pressure in the accretion disk balances

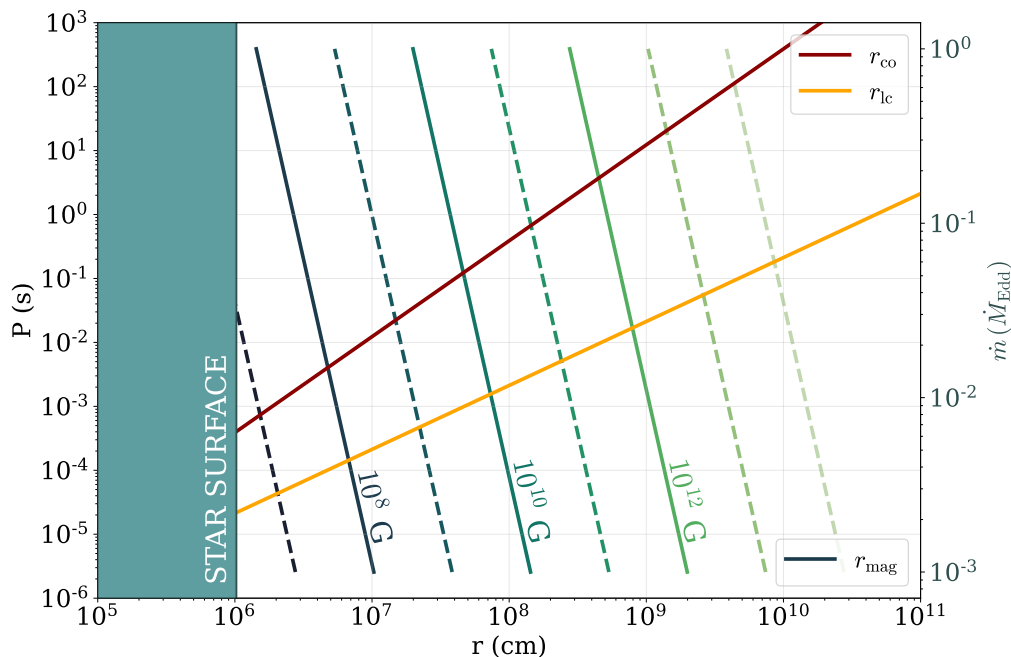


**Figure 2.2.** The three important radii in a NS system: The  $r_{\text{co}}$  and  $r_{\text{lc}}$  are plotted as a function of the period on the left axis, while the  $r_{\text{mag}}$  is shown as a function of luminosity on the right axis for magnetic field strength  $B_*$  ranging from  $10^7$  to  $10^{14}$  G. The calculations are performed for a NS with  $M = 1.4M_{\odot}$  and  $R_* = 10^6$  cm in the Newtonian gravity.

the magnetic pressure of the NS's magnetic field, and it indicates the inner edge of the accretion disk, see also Figure 1.2.

NS systems can exhibit three regimes. In the accreting regime, where  $r_{\text{mag}} < r_{\text{co}}$ , the angular velocity of the disk is lower than that of the NS, allowing the material to accrete onto the NS's surface. In the propeller regime, where  $r_{\text{co}} < r_{\text{mag}} < r_{\text{lc}}$ , the disk's angular velocity is higher than that of the NS, and the material is ejected from the system or accumulated on the  $r_{\text{mag}}$ . Lastly, in the radio pulsar regime, where  $r_{\text{mag}} > r_{\text{lc}}$ , no accretion can take place.

In the BH systems, where there is no hard surface or anchored magnetic field of the central object, the position of the inner edge of the accretion disk is solely determined by the system's geometry, which is governed by the GR effects. An important effect of the GR is the existence of a last stable orbit – a specific radius below which no stable circular orbit can exist. This orbit is usually labelled as ISCO, the innermost stable circular orbit. In the analytical model of a thin accretion disk, the ISCO is commonly considered as the inner edge of the accretion disk, based on the assumption that the shear of the fluid

drops rapidly on ISCO and the torque vanishes. These models assume that the material is too hot in the plunging region (between ISCO and the horizon), the flow is there laminar, and cannot contribute to the observed thermal spectra. The position of ISCO depends purely on the properties of the BH spacetime, such as its mass or angular momentum, see equation (2.20).

## 2.3. Black hole spacetimes

The framework of GR is necessary to describe the vicinity of BHs or other compact objects due to the strong curvature of spacetime caused by their extreme compactness. GR describes curved spacetimes using the metric tensor  $g_{\mu\nu}$  (Misner et al. 1973). The spacetime interval between two infinitesimally close events with spacetime coordinates  $(x)^A$  and  $(x)^B$  can be calculated using the metric tensor  $g_{\mu\nu}$  as

$$ds^2 = g_{\mu\nu} dx^\mu dx^\nu, \quad (2.9)$$

where  $dx = (x)^A - (x)^B$  and using the Einstein notation

$$x_\mu x^\mu = \sum_{\mu=0}^{N-1} x_\mu x^\mu = x_0 x^0 + x_1 x^1 + \dots + x_N x^N, \quad (2.10)$$

where  $N$  is the dimension of the vectors.

The spacetime interval is independent of the choice of coordinates, and the metric tensor provides us with complete information about the curvature of spacetime and how to measure distances at a given point.

### 2.3.1. Static spacetime - Schwarzschild metric

The Schwarzschild metric describes a non-rotating BH with zero charge (Schwarzschild 1916). The metric is static, spherically symmetric, and in the Schwarzschild coordinates  $(t, r, \theta, \phi)$ , using the  $(-, +, +, +)$  (space-like) signature<sup>2</sup>, the spacetime element is given by

$$ds^2 = - \left(1 - \frac{2M}{r}\right) dt^2 + \left(1 - \frac{2M}{r}\right)^{-1} dr^2 + r^2 d\theta^2 + (r^2 \sin^2 \theta) d\phi^2. \quad (2.11)$$

<sup>2</sup> which is used everywhere within this thesis

In these coordinates, the metric becomes singular at the gravitational radius  $r_{Schw} = 2r_g$ , where  $g_{tt} = 0$ , which also corresponds to the surface of infinite redshift. The spacetime is within this surface causally disconnected, so this surface is referred to as the event horizon. However, this singularity is only a coordinate one and can be eliminated by choosing a different coordinate system, unlike the singularity at  $r = 0r_g$  corresponding to  $g_{rr} = 0$ , which is physical.

Several significant surfaces can be found for the geodesical motion of a test particle around a Schwarzschild BH. Apart from the ISCO at  $r_{ISCO} = 6r_g$ , there is the marginally bound orbit (circular but unstable) at  $r_{mb} = 4r_g$ , and the photon orbit  $r_{ph} = 3r_g$ , an unstable circular orbit for mass-less particles like photons.

### 2.3.2. Rotating black holes: the Kerr metric

Both EM and GW observations suggest that most BHs, especially stellar-mass BHs, are rapidly rotating (Reynolds 2021). A rotating BH can be described using the Kerr metric, based on a solution of the Einstein equations for a rotating BH with zero charge in vacuum (Kerr 1963). The rotation is parameterized with a dimensionless spin parameter  $a = J/M^2$ , where  $J$  is the BH angular momentum. The most convenient coordinate system for the Kerr metric is the Boyer-Lindquist (BL) coordinates  $(t, r, \theta, \phi)$ , the spacetime element is then given by

$$ds^2 = - \left( 1 - \frac{2Mr}{\Sigma} \right) dt^2 - \frac{4Mar}{\Sigma} \sin^2 \theta dt d\phi + \frac{\Sigma}{\Delta} dr^2 + \Sigma d\theta^2 + \frac{A}{\Sigma} \sin^2 \theta d\phi, \quad (2.12)$$

where

$$\Sigma = r^2 + a^2 \cos^2 \theta, \quad (2.13)$$

$$\Delta = r^2 - 2Mr + a^2, \quad (2.14)$$

$$A = (r^2 + a^2)^2 - a^2 \Delta \sin^2 \theta, \quad (2.15)$$

which reduces to the Schwarzschild metric for  $a = 0$  and BL coordinates reduces to the Schwarzschild coordinates.

Two event horizons (surfaces where  $g^{rr} = 0$ ) exist for the Kerr metric,  $r_h^\pm$ , where (+) denotes the outer and (-) the inner horizon. These horizons do not coincide with the surfaces of infinite redshift, the ergosphere  $r_e^\pm$ , where  $g_{tt} = 0$ :

$$r_e^\pm = M \pm \sqrt{M^2 - a^2 \cos^2 \theta}, \quad (2.16)$$

$$r_h^\pm = M \pm \sqrt{M^2 - a^2}. \quad (2.17)$$

These surfaces, specifically  $r_e^+$  and  $r_h^+$ , define the ergoregion, an area where no static observers can exist and the spacetime corotates with the BH. This effect extends the boundary of the ergoregion, causing the spacetime to be dragged into corotation with the BH. This phenomenon is known as frame dragging. Consequently, a frame of an observer with zero angular momentum (ZAMO) can be found, which appears to orbit the BH for an observer at infinity, even though its angular momentum is locally zero.

The existence of the ergosphere allows for the extraction of rotational energy from the BH (Blandford & Znajek 1977; Penrose & Floyd 1971), powering jets in AGN and microquasars, which has also been confirmed in numerical simulations (Tchekhovskoy et al. 2011).

Describing the geodesic motion in the vicinity of a rotating BH becomes significantly more complex than the static one, particularly for non-equatorial motion. It is important to distinguish between prograde (+) and retrograde (−) motion with respect to the rotation of the BH. The radii of important orbits as a function of  $a$  are shown in Figure 2.3, where for  $a = 0$ , the values transition to those corresponding to a non-rotating BH. The expressions on the equatorial plane are given by

$$r_{\text{ph}}^\pm = 2M \left\{ 1 + \cos \left[ \frac{2}{3} \cos^{-1} \left( \mp \frac{a}{M} \right) \right] \right\}, \quad (2.18)$$

$$r_{\text{mb}}^\pm = 2M \mp a + 2\sqrt{M(M \mp a)}, \quad (2.19)$$

$$r_{\text{ISCO}}^\pm = M \left[ 3 + Z_2 \mp \sqrt{(3 - Z_1)(3 + Z_1 + 2Z_2)} \right], \quad (2.20)$$

where

$$Z_1 = 1 + (1 - a^2)^{\frac{1}{3}} \left[ (1 + a)^{\frac{1}{3}} + (1 - a)^{\frac{1}{3}} \right], \quad (2.21)$$

$$Z_2 = \sqrt{3a^2 + Z_1^2}. \quad (2.22)$$

These radii are important for modelling the structure and temporal variability of accretion disks. The photon orbit radius provides insights into the properties

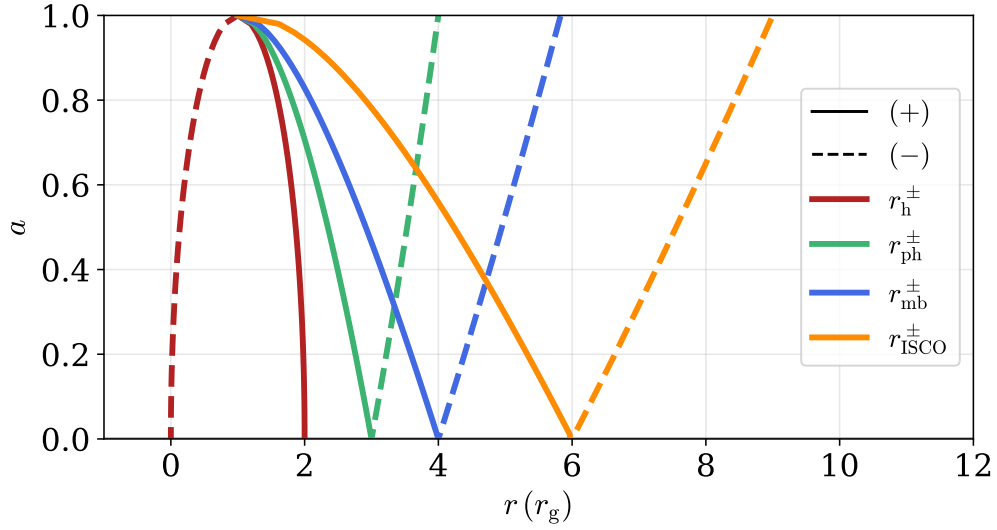


**Figure 2.3.** The inner  $r_h^-$  and outer  $r_h^+$  event horizons and important radii of the Kerr metric at the equatorial plane as a function of  $a$ . The full lines represent the prograde motion, while the dashed lines represent the retrograde motion (or the inner and outer event horizon). The values transition to the Schwarzschild metric ones at  $a = 0$ .

of the compact object that can be used to test the predictions of GR, which may become possible in the era of BH imaging within the Event Horizon Telescope (EHT) collaboration, (Paugnat et al. 2022; Wielgus et al. 2020). The ISCO, on the other hand, is often associated with the inner edge of the accretion disk and can be inferred from observations using the spectral-based fitting methods (Dauser et al. 2016; Zhang et al. 1997), enabling measurements of the mass and spin of a compact object. Finally, the location of the marginally bound orbit determines the maximal radial extension of the marginally overflowing accretion tori. In principle, comparison of the expected frequencies of oscillations of these tori with frequencies of observed HF QPOs allows for estimation of the mass and spin of the central object as well (Török et al. 2022).

In most cases, the Kerr or even the Schwarzschild metric is sufficient to describe accretion disks' structure and observational pictures in the case of the BH system. For the NS case, the Schwarzschild metric is generally acceptable, although the Hartle-Thorne metric (Hartle & Thorne 1968) is used when considering the effects of the star's quadrupole moment. The Hartle-Thorne metric describes the spacetime around a compact, rigidly rotating, axially symmetric body accurately to the second order of angular momentum of the star and the first order of its quadrupole moment.

## 2.4. Analytical models of accretion disks

Analytical solutions for a flow of plasma in an accretion disk are derived based on the energy, mass, and momentum conservation principles. However, in order to obtain these solutions, several assumptions are typically made. These assumptions include:

- Neglecting self-gravitation effects, assuming that the gravitational influence of the disk on itself is negligible.
- Assuming that the disk midplane lies in the equatorial plane of the central object.
- Using the ideal gas approximation.
- Assuming a steady and axisymmetric disk ( $\partial/\partial t = 0$ ,  $\partial/\partial\phi = 0$ ).
- Neglecting the effects of a large-scale magnetic field.
- Assuming hydrostatic equilibrium in the vertical direction.
- Assuming Keplerian motion of the fluid, setting  $\Omega = \Omega_K = \sqrt{\frac{GM}{r^3}}$ ,

These assumptions lead to analytical solutions for the disk structure. However, these solutions may not fully capture the complexities of real-world accretion processes, and more sophisticated numerical simulations are often needed for a more accurate description.

The first analytical model of accretion disk was introduced by [Shakura & Sunyaev \(1973\)](#), who described a geometrically thin, optically thick disk. In the same year, [Novikov & Thorne \(1973\)](#) and then [Page & Thorne \(1974\)](#) extended the solution to include the effects of GR, providing corrections for a rotating Kerr BH.

The thin disk model assumes a small vertical extension. It is radiatively efficient, and the inner edge is located at  $r_{\text{ISCO}}$ , where the boundary condition is such that the stress is zero. The thin disk quickly gained popularity and has been widely used to fit observational data from sources with compact objects ([Li et al. 2005a](#)). In this model, the viscosity responsible for the transport of angular momentum is parameterized by the viscous coefficient  $\alpha$ , the viscous stress  $t_{r\phi}$  in the disk is assumed to be proportional to the pressure  $p$ ,

$$t_{r\phi} = \alpha p. \tag{2.23}$$

The  $\alpha$  parametrization used in the thin disk model operates well even though the specific source of viscosity remained unknown for quite a long time. For many years, various possibilities were considered to explain the origin of viscosity in astrophysical plasma. It was not until almost 20 years after the thin disk model was constructed that [Balbus & Hawley \(1991, 1998\)](#) introduced the con-

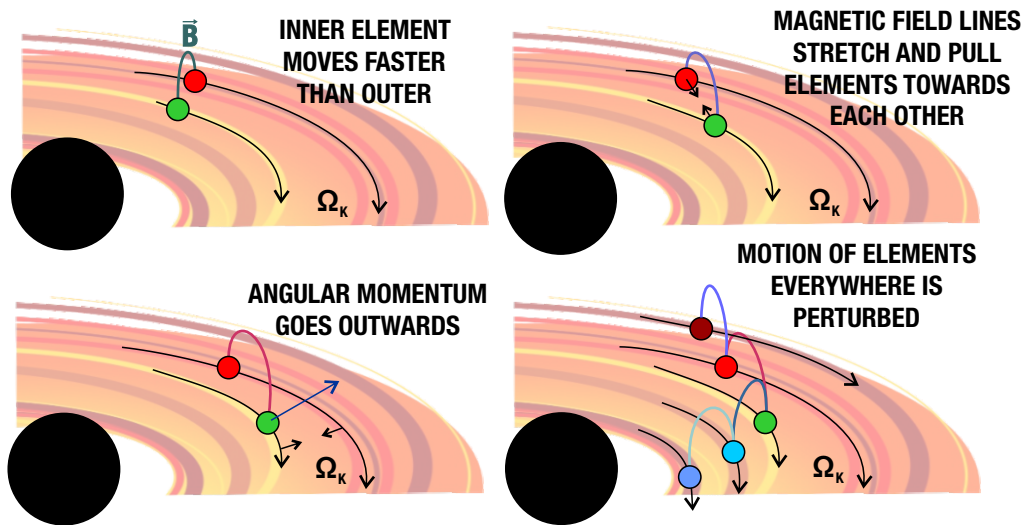


Figure 2.4. Schematic explanation of the MRI

cept of the magnetorotational instability (MRI) as a potential source of viscosity. The observations of accretion in astrophysical sources showed that the value of  $\alpha$  is typically in the range between  $\alpha = 0.01 - 0.1$  (e.g. [Gou et al. 2011](#)). Similar values were obtained in numerical simulations ([Penna et al. 2010](#)). However, the simulations showed that the value of  $\alpha$  is far from constant in the disk, with a distinct peak in the inner parts of the disk and the plunging region ([Penna et al. 2013b](#)).

#### 2.4.1. Magnetorotational instability

The MRI is an instability occurring in magnetized rotating systems, such as accretion disks. It is caused by the differential rotation of the ionized gas carrying a low-scale magnetic field. The stretching of magnetic field lines gives rise to turbulences in the accretion flow and carries the angular momentum outward, even in the case of a very weak magnetic field.

In the ideal MHD approximation, where the fluid is considered a perfect conductor, the electric field vanishes in the frame comoving with the fluid, and the magnetic field lines are frozen into the fluid. As a result, the field lines act as springs connecting two fluid elements, one on a larger orbit with lower angular velocity and the other on a lower orbit with higher angular velocity. As the fluid orbits, the inner element moves away from the outer one due to the differential rotation, causing the magnetic spring to stretch and pull the inner element back. Consequently, the inner element loses angular momentum and slows down, while the outer element gains this angular momentum and speeds



up. This process occurs continuously throughout the disk, gradually transferring angular momentum outward and rising turbulences throughout the fluid. Figure 2.4 shows a schematic picture of the MRI.

The MRI mechanism is often employed in MHD simulation to trigger turbulences and force the matter to flow towards the central object without implementing an artificial viscosity term into the source terms of the flow equations. Simulations showed that the  $\alpha$  disk assumptions agree with the simulations results, e.g. in Penna et al. (2012) or Penna et al. (2013b). Even though MRI is not the only magnetic instability present in a disk, it matches the  $\alpha$  viscosity in magnitude. The value of  $\alpha$  derived from simulations is lower in the disk body by order of magnitude than fitted from observations using an analytical model, which, however, assumes the value of  $\alpha$  constant throughout the whole disk.

The presence of a magnetic field in the disk is also likely to play a crucial role in stabilizing the luminous regimes of the thin disk model, as extensively discussed and analytically explored (Begelman & Pringle 2007; Oda et al. 2009), and confirmed in simulations (Huang et al. 2023; Lančová et al. 2019; Mishra et al. 2022; Sądowski 2016).

## 2.5. Overview of analytical models

Many analytical models of accretion disks have been proposed over the years, corresponding to different accretion regimes, typically characterized by  $\dot{M}$ . These models differ in terms of the optical depth  $\tau$ , half-thickness ratio to radius  $H/r$ , radiative efficiency, or temperature  $T$  (see Figure 2.5).

For a very low mass accretion rate, such as in the case of the BH in the centre of the Galaxy, Sgr A\*, the accretion disk is optically thin, and the gas density is so low that Coulomb interactions are no longer effective. As a result, the electrons and ions have significantly different temperatures, with the electrons being much colder than the ions (Narayan & McClintock 2008). In this regime, radiative cooling is insufficient, and the dominant cooling mechanism is advection; These types of disks are often referred to as Advection-Dominated Accretion Flows (ADAFs) and emit a power-law spectrum with a strong Compton component.

As the mass accretion rate increases, the gas density also increases, Coulomb coupling becomes efficient, and the ions and electrons temperatures become equal. The disk becomes optically thick, and the radiation cooling becomes efficient. In this regime, the disk flattens into a thin disk of Shakura & Sunyaev (1976). However, once the radiation pressure starts to dominate, the thin disk

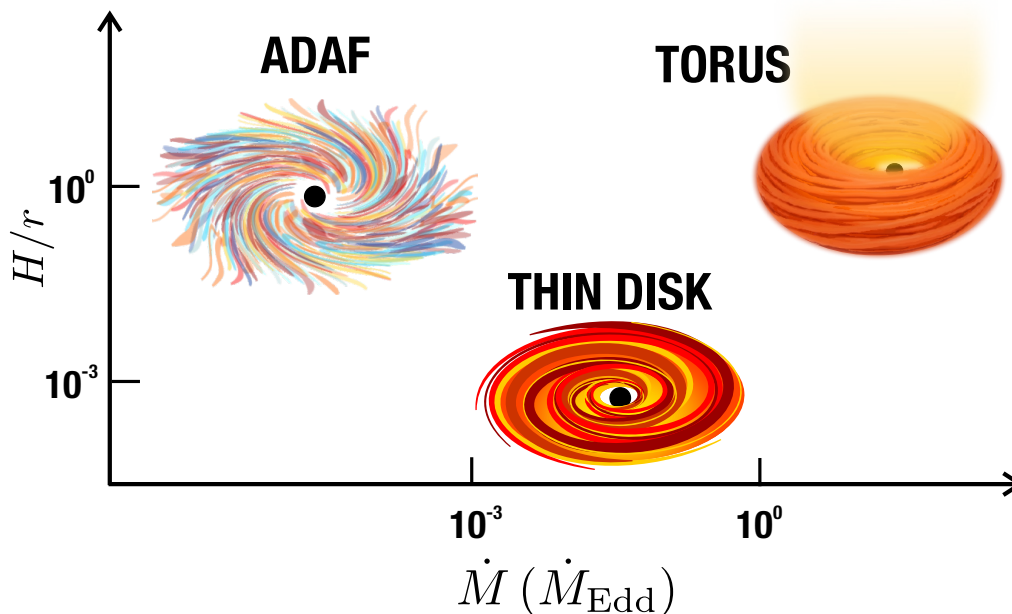


**Figure 2.5.** Illustration of three accretion disk models for various mass accretion rates and disk thicknesses.

model is known to be thermally and viscously unstable (Lightman & Eardley 1974; Shakura & Sunyaev 1976). This regime corresponds to mass accretion rates down to approximately  $\dot{m} \approx 0.01$  for a stellar mass compact object.

Nevertheless, observations have shown that thin disks can still be observed at luminosities corresponding to much higher mass accretion rates during outbursts (Li et al. 2005b; McClintock et al. 2014) when the disk is in a soft spectral state. The thin disk emits a multi-temperature black body spectrum, illustrated in Figure 2.6.

The local flux of a thin disk is given as (Page & Thorne 1974)

$$F = \frac{\mathcal{Q}}{\mathcal{B}\sqrt{\mathcal{C}}} \frac{3GM\dot{M}}{8\pi r^3}, \quad (2.24)$$

where  $\mathcal{Q}$ ,  $\mathcal{B}$  and  $\mathcal{C}$  are the relativistic correction, which can be found, e.g. in Appendix A of Kato et al. (2008). In the non-relativistic limit, it becomes  $(1 - \sqrt{r_{in}/r})$ . The local flux is zero under the inner edge and maximal close to the inner edge, e.g., for a non-rotating BH at  $\sim 10r_g$ . The flux strongly depends on the position of the inner edge, which is linked to the spin of the central BH, while the dependence on the  $\dot{m}$  is not so strong, as shown in Figure 2.7. This

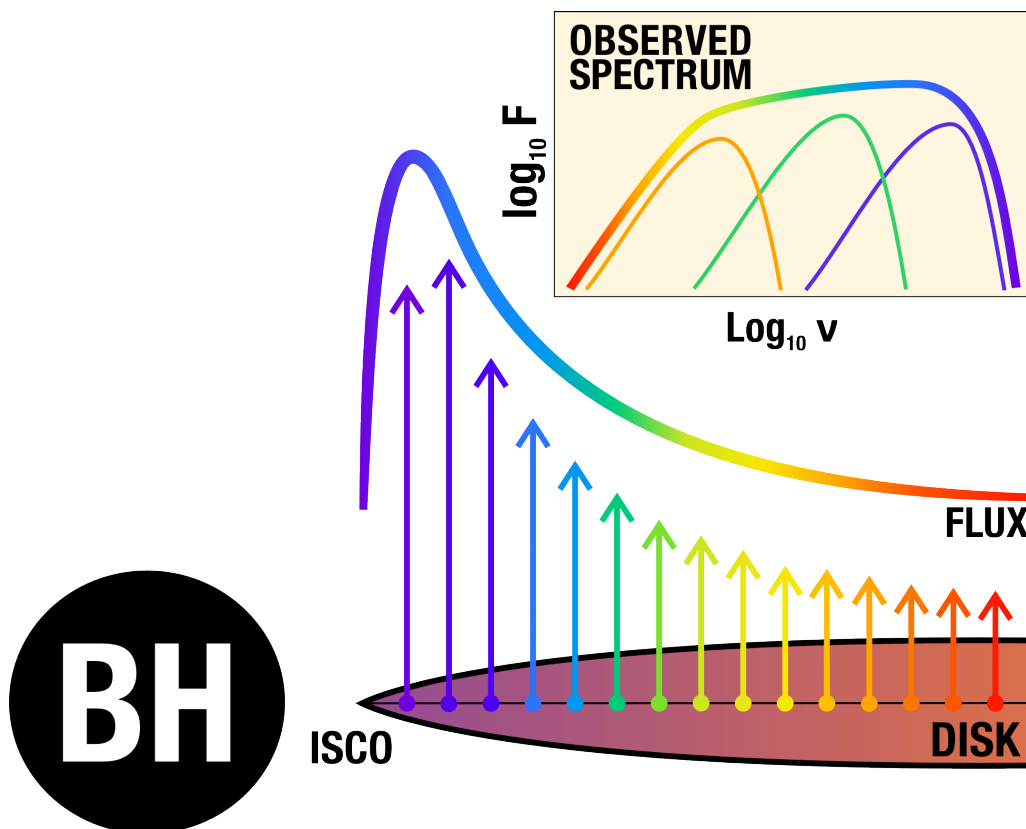


**Figure 2.6.** Illustration of a thin disk and its local flux. The inset shows an observable multi-black body spectrum as a sum of black-body spectra corresponding to the temperature on certain radii.

feature of the thin disk model is used to establish the spin and mass of a BH from observations.

It is evident that the thin disk model lacks an important part that would stabilize it even at higher mass accretion rates. Several stabilizing mechanisms have been proposed so far, (Ciesielski et al. 2012; Oda et al. 2009; Rózańska et al. 1999; Zhu & Narayan 2013); however, the magnetic field and magnetic pressure seem to be most plausible (Begelman & Pringle 2007; Li & Begelman 2014), even though the disk then turns to be geometrically thick, as was also shown in numerical simulations (Huang et al. 2023; Lančová et al. 2019; Mishra et al. 2020; Sądowski 2016).

For  $\dot{m} \sim 1$ , the advection of radiation (photon trapping) becomes an important cooling mechanism, and this state corresponds to the slim disk model, an (essentially one-dimensional) analytic model of an optically thick advective disk, with  $H/r \approx 1$  (Abramowicz et al. 1988). Photon trapping occurs when the

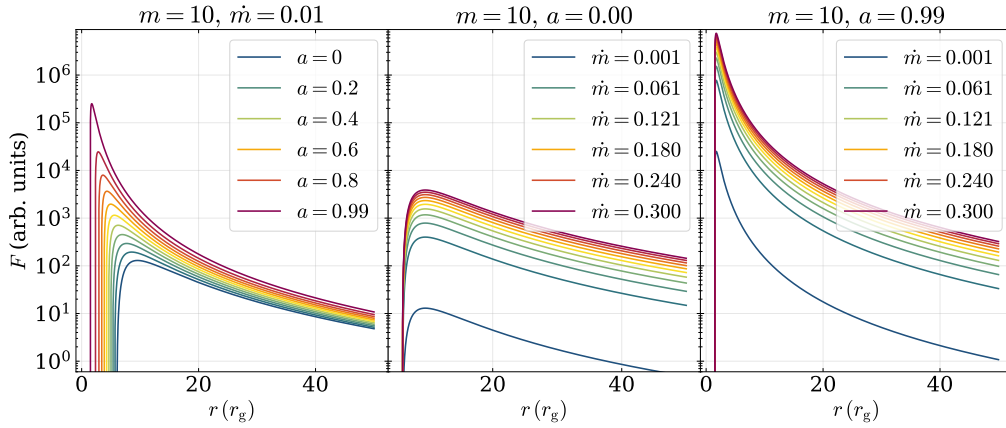


**Figure 2.7.** Radial profile of the local flux  $F$  of a thin disk as a function of spin  $a$  (left), the  $\dot{m}$  for a non-rotating BH (middle), and maximally rotating BH (right) panel, for  $M = 10M_\odot$ .

disk opacity is so high that the photons generated in the plasma are effectively trapped and cannot reach the surface. Instead, they are carried away with the matter of the disk, as shown in Figure 2.8. Photon trapping can be quantitatively described by comparing the photon diffusion time,  $t_{diff} = 3H\tau/c$  (Mihalas & Mihalas 1984), and the accretion time,  $t_{acc} = r/|v^r|$ . The radius at which photon trapping becomes important can be determined using the continuity equation for disk accretion and electron scattering opacity (Kato et al. 2008):

$$r_{\text{trap}} = 3 \left( \frac{H}{r} \right) \dot{m} r_g, \quad (2.25)$$

as a function of  $\dot{m}$  and the disk thickness to radius ratio,  $H/r$ . For high  $\dot{m}$  and  $H/r$ , the trapping radius is larger than  $r_{\text{ISCO}}$ , and the advection of radiation becomes an important cooling mechanism in the slim disk model.

The slim disk is often used to model the luminous state of XRBs and ULXs (Foschini et al. 2006). It is less radiatively efficient than the thin disk since a fraction of the photons are advected into the BH. The inner edge of the slim disk is located inside the ISCO. However, the slim disk spectral model, `slimbb`, (Sądowski 2009), when applied on a data from microquasar in outburst, does not retrieve consistent values of BH spin for different observed luminosity when it increases from  $L \approx 0.01 L_{\text{Edd}}$  up to  $L \approx 0.5 L_{\text{Edd}}$ , corresponding to the radiation pressure-dominated regime of accretion. This was demonstrated in the case of LMC X-3, in Straub et al. (2011). When fitting the observed spectra at different

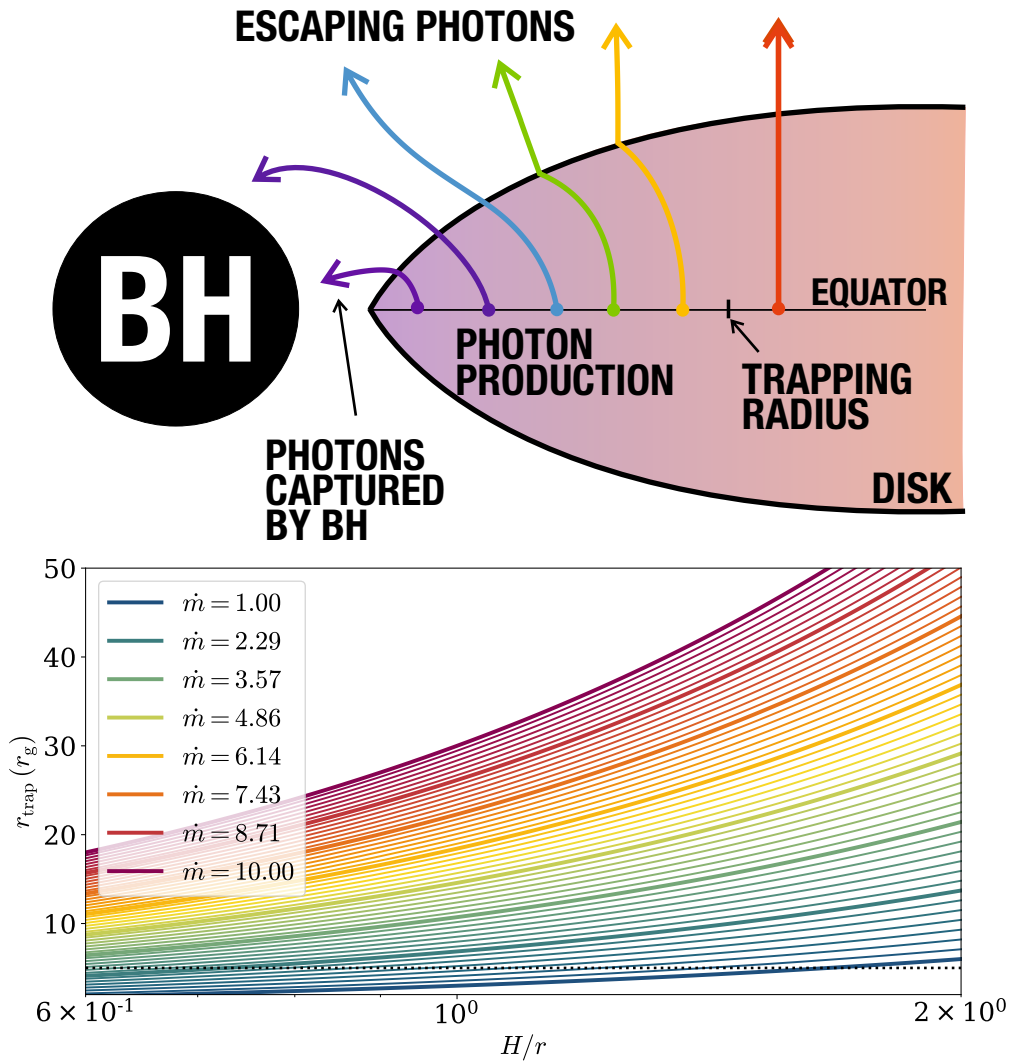


**Figure 2.8.** *Top:* Illustration of photon trapping in a thick accretion disk. *Bottom:* The photon trapping radius as a function of disk thickness for selected values of  $\dot{m}$ . The dotted line represents the  $r_{\text{ISCO}}$  for a non-rotating BH.

luminosity, the derived value of the BH spin was not constant, and the same behaviour was seen for the thin disk model.

The Eddington limit is interpreted as the maximal luminosity a disk can reach, and consequently, the  $\dot{M}_{\text{Edd}}$  the highest possible mass accretion rate before radiation pressure prevents accretion. However, this value is derived under many assumptions, such as spherical accretion. Higher luminosities can be reached by breaking them, such as considering a thick accretion disk (or torus) with  $H/r > 1$ . In such a case, a funnel forms around the rotational axis, allowing radiation to escape and reduce radiation pressure acting on the accreting material. The escaping radiation is also highly collimated towards observers close to the rotational axis and obscured by the thick torus body for equatorial observers. Super-Eddington accretion is actually frequently observed in the Universe, as seen in ULXs, AGN, and microquasars.

The most popular model of the super-Eddington accretion disk is the “Polish doughnut” (Abramowicz et al. 1978; Jaroszyński et al. 1980), describing a radiation pressure-supported accretion torus. In the Polish doughnut model, the matter distribution is assumed to be stationary and axially symmetric and the angular momentum constant within the disk. The distribution of matter in the disk is limited by the equipressure surfaces resulting from the “von Zeipel theorem” (Seguin 1975; von Zeipel 1924), which states that the surfaces of constant angular velocity and angular momentum coincide for a barotropic fluid.

A particular case of the Polish doughnut model is the cusp torus, which is the largest physical configuration of the accretion tori, where the fluid of the disk fills the largest closed equipressure surface, forming a cusp on its inner edge, between the  $r_{\text{ISCO}}$  and  $r_{\text{mb}}$ , see Figure 2.9. The cusp torus is implemented in various QPOs models, which will be further elaborated in Chapter 5 (Abramowicz & Kluźniak 2001; Blaes et al. 2006; Kluźniak & Abramowicz 2001; Török et al. 2016a, 2022).

## 2.6. Modelling the accretion disk in microquasars

Accretion disks in microquasars are commonly modelled using a simple yet powerful thin disk model based on a simple and convenient description of the viscosity in the fluid using the  $\alpha$  parametrization, where a single constant  $\alpha$  relates the fluid stress and pressure.

The alternating periods of luminous outbursts and quiescent fades are often attributed to state transitions of the accretion disk caused by unidentified instabilities (Done et al. 2004; Vincentelli et al. 2023). However, the time scale of

fundamental instabilities in the thin disk model is much shorter than the observed variability. Yet, the emitted spectrum and general behaviour are consistent with the predictions of analytical models in many aspects.

The stability of the sub-Eddington accretion disk plays an important role in modelling the entire life cycle of XRBs. However, accurately modelling the whole outburst and state transitions of a XRB in complex numerical simulations remains a challenge. In our work, (Lančová et al. 2023; Wielgus et al. 2022), we successfully modelled the observable signal from simulations of a mildly sub-Eddington radiation pressure-dominated yet stable puffy disk (Lančová et al. 2019) and compared it to the expected signal from XRB. We found that the simulations can be compared to observed data and that the estimation of source parameters, such as BH spin, is strongly influenced by the specific topology of the puffy disk system compared to that obtained using standard analytical models.

The oversimplified one-dimensional  $\alpha$ -disk cannot capture the dynamics and three-dimensional structure of turbulent accretion flows in the vicinity of a BH. A self-consistent accretion model must address the three-dimensional interplay between gravity, fluid dynamics, magnetic fields, and radiation. It should also capture the turbulent nature of the flow driven by the MRI, which provides the crucial mechanism for angular momentum transport. Such a model can be obtained using advanced numerical methods for modelling plasma, such as in the framework of global general relativistic radiative magnetohydrodynamic (GR-

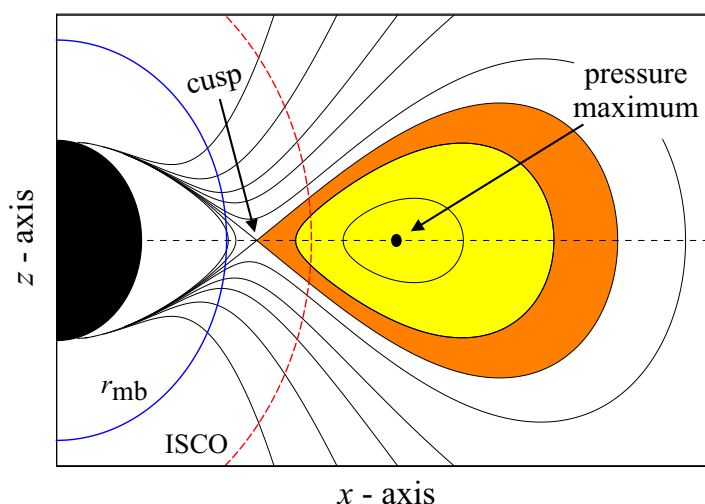


**Figure 2.9.** Illustration of the cusp torus configuration. Adopted from Kotrlová et al. (2020), based on Jaroszyński et al. (1980).

RMHD) simulations. However, simulating optically thick, geometrically thin accretion structures is computationally expensive, requiring high resolution of the three-dimensional numerical grid (Balbus & Hawley 1998), short integration time steps, and the use of implicit solvers to capture the evolution of radiation field (Sądowski et al. 2013). Consequently, many published works sacrifice either radiation (Liska et al. 2019), magnetic field (Mishra et al. 2020), or general relativity (Jiang et al. 2019).

The topic of the sub-Eddington accretion has been a major part of my work during my studies, resulting in the development of the puffy disk model (Lančová et al. 2019), where the results of advanced simulations were presented as one of the first self-consistent simulations of a stable mildly sub-Eddington accretion.



## Chapter 3

# GRRMHD simulation of sub-Eddington accretion

The global general relativistic (GR) radiative (R) magneto (M) hydrodynamics (HD) method is used to simulate the flow of magnetized plasma, including the exchange of energy and momentum with radiation in the framework of GR. Astrophysical fluids in accretion disks, primarily composed of hydrogen, usually have high enough temperatures to be ionized ( $T \gtrsim 10^4$  K). The presence of free electrons in the plasma leads to the generation of a magnetic field through electric currents, which significantly influences the properties of the flow.

In global simulations, the computational domain contains the entire accretion disk and thus captures the complex dynamics and the interactions between the disk, corona, outflows, and jets. On the other hand, a shearing box (or shearing sheet in 2D) simulates the plasma flow within a relatively small box placed at a specific location in the disk, such as the center, surface, or base of a jet. Shearing box simulations help study the structure and small-scale dynamics of the flow.

The development of the GRMHD method began in the late 1980s ([Anile 1989](#)), followed by the development of complementary numerical methods in the 1990s ([Komissarov 1999](#)). In the early 2000s, several codes were developed, taking advantage of the rapid advancements in high-performance and supercomputing, which led to a broader implementation of MHD and GRMHD in accretion disk research.

One of the most widely used GRMHD codes is the HARM ([Gammie et al. 2003](#)), which has since been extended and modified in various variants and derivatives, such as the HARMPI and H-AMR codes ([Liska et al. 2022](#); [Tchekhovskoy 2019](#)) heavily parallelized and/or including advanced treatment of radiation, or the HARM\_COOL code ([Janiuk 2023](#)), which includes cooling by neutrinos. The KORAL code, described below, was developed alongside HARM and shares many methods and algorithms. Other notable codes include the BHAC, implementing advanced nuclear equations of state for the matter, neutrino leakage,

and the possibility to use numerical metrics for non-BH spacetimes (Porth et al. 2017). The IllinoisGRMHD (Etienne et al. 2015) is designed for dynamical metric simulations of BH and NS mergers within the *Einstein Toolkit* framework (Löffler et al. 2012). Many other MHD codes are available for studying different accretion regimes, such as the Athena++ (White et al. 2016), Cosmos++ (Anninos et al. 2005) or non-relativistic but resistive code PLUTO (Mignone et al. 2007), among others. This chapter introduces the equations and numerical methods as implemented in the KORAL code. However, it represents only one road that can be taken. To describe other existing methods would be beyond the scope of this work.

This chapter aims to summarize the methods and features of the KORAL code in the version used in the puffy disk simulations published in Lančová et al. (2019). Since its first publication in Sądowski et al. (2013), new features have been added to the code, and no comprehensive article summarizing these updates exists. The KORAL code was tested against other codes in the *The Event Horizon General Relativistic Magnetohydrodynamic Code Comparison Project* (Porth et al. 2019).

The following list provides a selection of articles related to the KORAL code, although some more might need to be included. KORAL was first introduced as a GRRHD code in Sądowski et al. (2013). The MHD was added in Sądowski et al. (2014), followed by the photon-conserving Comptonization and radiation viscosity in Sądowski & Narayan (2015). The mean-field dynamo, which allows for long 2D simulations without losing the azimuthal component of the magnetic field and suppressing the MRI, was introduced in Sądowski et al. (2015). Two-temperature heating and cooling of electrons and ions, enabling simulations of low-density flows where the ion and electron gases have different temperatures due to inefficient Coulomb interaction, were implemented in Sądowski et al. (2017), together with self-consistent calculation of the adiabatic index and advanced treatment of opacities. The evolution of relativistic non-thermal electrons was incorporated in Chael et al. (2017).

### 3.1. GRRMHD equations

KORAL solves the conservation equations of mass, momentum, and energy on a fixed grid in an arbitrary metric. The code adopts geometrized units where  $G = c = 1$ , the gravitational radius  $r_g = GM/c^2$  as the unit of length, and  $t_g = r_g/c$  as the unit of time. Greek indices range from 0 to 3, while Latin indices range from 1 to 3.

The conservation equations for a fluid with a rest mass density  $\rho$  and lab frame 4-velocity  $u^\mu$  are:

$$(\rho u^\mu)_{;\mu} = 0, \quad (3.1)$$

$$(T^\mu{}_\nu)_{;\mu} = G_\nu, \quad (3.2)$$

$$(R^\mu{}_\nu)_{;\mu} = -G_\nu, \quad (3.3)$$

$$(F^{*\mu\nu})_{;\mu} = 0, \quad (3.4)$$

where  $R^\mu{}_\nu$  is the radiation stress-energy tensor,  $G_\nu$  the radiative 4-force density describing the exchange of energy and momentum between the gas and radiation (see section 3.1.1), and  $F^{*\mu\nu}$  the dual tensor of the electromagnetic field.

The ideal MHD approximation is used in the KORAL code, assuming infinite conductivity of the fluid, which leads to the vanishing of the electric field in the fluid frame. Under this assumption,  $F^{*\mu\nu}$  can be given in a simple form,

$$F^{*\mu\nu} = b^\mu u^\nu - u^\mu b^\nu, \quad (3.5)$$

where  $b^\mu$  is related to the magnetic field  $B^i$  as (Komissarov 1999)

$$B^i = F^{*i0} = F^{*it} = b^i u^t - u^i b^t, \quad (3.6)$$

and vice versa,

$$b^t = B^i u_i, \quad (3.7)$$

$$b^i = \frac{B^i + b^t u^i}{u^t}. \quad (3.8)$$

The gas stress-energy tensor,  $T^{\mu\nu}$ , is given as

$$T^{\mu\nu} = (\rho + u_{\text{int}} + p_{\text{gas}} + b^2) u^\mu u^\nu + \left( p_{\text{gas}} + \frac{b^2}{2} \right) g^{\mu\nu} - b^\mu b^\nu, \quad (3.9)$$

where  $u_{\text{int}}$  is the internal energy density,  $p_{\text{gas}}$  is the gas pressure, and  $g^{\mu\nu}$  represents the metric tensor.

For the adiabatic equation of state, the gas internal energy  $u_{\text{int}}$  in the comoving frame and the gas pressure  $p_{\text{gas}}$  are related by

$$p_{\text{gas}} = (\Gamma - 1)u_{\text{int}} \quad (3.10)$$

where  $\Gamma$  is the adiabatic index. Typically,  $\Gamma$  is assumed to be  $5/3$  for gas pressure and  $4/3$  for optically thick radiation pressure-dominated or relativistic fluid.

From (3.5) is evident that  $F^{*tt} = 0$ , therefore the time component of equation (3.4) is not an evolution equation. However, the  $\nabla \cdot \mathbf{B} = 0$  constraint can be directly delivered from there. It can also be shown that the magnetic 4-vector is perpendicular to the 4-velocity in the fluid frame,  $b^\mu u_\mu = 0$  (Komissarov 1999).

The Maxwell equation in the lab frame then consists of the induction equation

$$\partial_t (\sqrt{-g}B^i) = -\partial_j (\sqrt{-g}b^i u^j - u^j b^i), \quad (3.11)$$

where  $\sqrt{-g}$  is the metric determinant. This equation governs the evolution of the magnetic field and the divergence-free constraint,

$$\frac{1}{\sqrt{-g}}\partial_i (\sqrt{-g}B^i) = 0, \quad (3.12)$$

which ensures  $\nabla \cdot \mathbf{B} = 0$  constrain. However, equation (3.12) is not directly evolved to prevent the production of magnetic monopoles due to numerical errors. Instead, the flux-CT method of Tóth (2000) is implemented, which solves the flux-interpolated constrained transport.

### 3.1.1. Radiation

The hot material in accretion disks produces EM radiation, which interacts with the gas and can significantly influence the fluid's dynamics and temperature by emission and absorption. If the disk is optically thin, the photons escape freely and can be up-scattered by the inverse Compton process. However, this process has little dynamical influence on the fluid, and the consequences to the observed spectrum can be calculated separately during post-processing. On the other hand, if the fluid is optically thick, the photons are effectively trapped and influence the flow dynamics by generating radiation pressure. Photon production in the fluid is also an essential cooling mechanism that must be considered when modelling radiatively efficient accretion regimes.

Hence, the radiation should be an inseparable part of sub-Eddington accretion disk simulations and be evolved simultaneously with the fluid in radiatively efficient flows. However, capturing the complicated dynamics of gas and radiation interaction is challenging, and some sacrifices for the sake of computational simplicity have to be made.

The ideal way of following each photon trajectory is not feasible in an optically thick medium where the photon's mean path is extremely short, and an enormous number of individual photons would be needed to capture the dynamics correctly. Based on the various moments of the radiation field, the method used in the KORAL code can adequately solve the problem in both optically thin and thick media by handling the radiation as an additional “fluid” in the domain. The radiation tensor  $R_{\mu\nu}$  exchanges momentum and energy with the matter through the radiation 4-force density  $G_\nu$ , and the exchange is conservative,  $(T^\mu{}_\nu + R^\mu{}_\nu)_{;\mu} = 0$  (see equations (3.2) and (3.1)).

$R_{\mu\nu}$  consists of components corresponding to various moments of the frequency-integrated specific intensity  $I = \int_\nu I_\nu d\nu$ . In the fluid frame<sup>1</sup> the radiative energy density  $\hat{E} = \int \hat{I}_\nu d\nu d\Omega$ , flux  $\hat{F}^i = \int \hat{I}_\nu d\nu d\Omega N^i$  and the pressure tensor  $\hat{P}^{ij} = \int \hat{I}_\nu d\nu d\Omega N^i N^j$ , where  $\nu$  is frequency,  $\Omega$  the solid angle and  $N^i$  the unit vector in direction  $x^i$ , together form (Mihalas & Mihalas 1984; Sądowski et al. 2013)

$$\hat{\mathbf{R}} = \begin{pmatrix} \hat{E} & \hat{F}^i \\ \hat{F}^j & \hat{P}^{ij} \end{pmatrix}. \quad (3.13)$$

This relatively simple formulation is a function of all components of  $R^{\mu\nu}$  in an arbitrary frame; thus, to close the set of conservation equations (3.3), all components of  $R^{\mu\nu}$  are needed. However, only the radiative energy density  $R^{tt}$  and fluxes  $R^{ti}$  are known in an arbitrary frame. In the KORAL code, the **M1** closure scheme (Levermore 1984; Sądowski et al. 2013) is implemented to find the full form of  $R^{\mu\nu}$ .

The scheme assumes the existence of a “radiation rest frame”, in which the radiation is isotropic<sup>2</sup>, and where radiation tensor acquires a simple form of

$$\tilde{R}^{\mu\nu} = \begin{pmatrix} \tilde{E} & \tilde{E}/3 \\ \tilde{E}/3 & 0 \end{pmatrix} = \frac{4}{3}\tilde{E}\tilde{u}_R^\mu\tilde{u}_R^\nu + \frac{1}{3}\tilde{E}\eta^{\mu\nu}, \quad (3.14)$$

<sup>1</sup> the hats are denoting the fluid frame throughout this work

<sup>2</sup> this frame is denoted by tildes

where  $\tilde{u}_R^\mu = (1, 0, 0, 0)$  is the radiation rest frame 4-velocity, and the metric  $\eta^{\mu\nu}$  is locally Minkowski.

Since this equation is in covariant form, an arbitrary frame expression can be found:

$$R^{\mu\nu} = \frac{4}{3}\tilde{E}u_R^\mu u_R^\nu + \frac{1}{3}\tilde{E}g^{\mu\nu}. \quad (3.15)$$

However,  $\tilde{E}$  should always be interpreted as the radiation energy density in the radiation rest frame.

The *M1* closure works sufficiently well in both optically thin and thick regimes, as long as there is only one source of radiation. Since the radiation is handled as a fluid, in a multiple beams intersection, radiation from one source would be interacting with another as a fluid would do. Fortunately, in astrophysical simulations, such a scenario is usual (see the extensive testing in [Sądowski et al. \(2013\)](#) for reference).

### 3.1.2. Interactions between the fluid and radiation

The radiation 4-force density  $G^\mu$ , describing the conservative interactions between radiation and the fluid, is given by ([Mihalas & Mihalas 1984](#); [Sądowski & Narayan 2015](#); [Sądowski et al. 2015, 2013](#))

$$\hat{G}^\mu = \int (\chi_\nu I_\nu - \eta_\nu) dv d\Omega N^i, \quad (3.16)$$

which takes a relatively simple form for the frequency-integrated quantities:

$$\hat{G}^\mu = \begin{pmatrix} \kappa_a \rho (\hat{E} - 4\pi \hat{B}) \\ (\kappa_a + \kappa_{es}) \rho \hat{F}^i \end{pmatrix}, \quad (3.17)$$

where  $\hat{B}$  is the frequency-integrated Planck function given by  $\hat{B} = aT_g^4/4\pi$ , where  $a$  is the radiation constant and  $T_g$  the gas temperature.  $\chi = \kappa_a + \kappa_{es}$  is the total opacity coefficient consisting of the absorption and electron scattering opacity, respectively<sup>3</sup>.

<sup>3</sup> In the simulations of the puffy disk, we adopted  $\kappa_a = 6.4 \times 10^{22} \rho T^{-7/2} \text{ cm}^2 \cdot \text{g}^{-1}$  and  $\kappa_{es} = 0.34 \text{ cm}^2 \cdot \text{g}^{-1}$ .

In [Sądowski et al. \(2014\)](#) the covariant form of  $G^\mu$  was introduced,

$$G^\mu = -\rho \left[ \chi R^{\mu\nu} u_\nu + \left( \kappa_{es} R^{\alpha\beta} u_\alpha u_\beta + 4\pi \kappa_a B \right) u^\mu \right]. \quad (3.18)$$

However, this approach neglects the exchange of momentum *and* energy during the particle-photos interactions and is appropriate only to model the elastic scattering and thermal absorption. The  $G^0$  term corresponds to the gain of fluid energy density due to absorption ( $\kappa_a \rho \tilde{E}$ ) and loss due to emission ( $\kappa_a \rho a T_g^4$ ). For the black body radiation, the effective radiation temperature is defined as  $T_R^4 = \tilde{E}/a$  in the fluid frame. The  $\hat{G}^0$  in the fluid frame is then

$$\hat{G}^0 = \kappa_a \rho a (T_R^4 - T_g^4), \quad (3.19)$$

which drives the system towards local thermal equilibrium (LTE).

The space components,  $G^i$ , on the other hand, describe a symmetric absorption and re-emission of photons by the fluid, which drives the system to a state of zero radiation flux in the fluid frame.

To enhance this exchange and to include the energy changes during scattering, Comptonization is implemented in KORAL, and it comes in two options. The more advanced one is the photon conserving scheme introduced in [Sądowski & Narayan \(2015\)](#), where the radiation is treated as a Bose-Einstein fluid, and the photon number density  $n_i$  is evolved throughout the simulation. However, this significantly increases the computational cost of the simulations, and for many applications, a more straightforward black body Comptonization is sufficient.

The radiation 4-force density in the fluid frame  $\hat{G}^\mu$  can be written as

$$\hat{G}^\mu = \hat{G}_{\text{BB}}^\mu - \hat{G}_{\text{Compt}}^\mu, \quad (3.20)$$

where  $\hat{G}_{\text{BB}}^\mu$  is given by (3.19) and the term corresponding to the black-body Comptonization is given by

$$\hat{G}_{\text{Compt}}^0 = \rho \hat{E} \kappa_{es} \left[ \frac{4k_B (T_g - T_R)}{m_e} \right] \left( 1 + 3.683 \frac{k_B T_g}{m_e} + \frac{4k_B T_g}{m_e} \right) \left( 1 + \frac{4k_B T_g}{m_e} \right)^{-1}, \quad (3.21)$$

where  $k_B$  is the Boltzmann constant and  $m_e$  the electron mass. The last two expressions in parentheses are fitted formulas corresponding to corrections for relativistic electrons; see [Sądowski & Narayan \(2015\)](#)<sup>4</sup>.

<sup>4</sup> There is a typo in [Sądowski & Narayan \(2015\)](#), missing 4 in the last term.

### 3.1.3. Radiative viscosity

The **M1** closure tends to overestimate the angular momentum of photons close to the rotational axis, which leads to the creation of unphysical shocks, which significantly alters the behaviour of both gas and radiation in the axis regions and can result in misinterpretation of the results. In KORAL, it is addressed by introducing an artificial viscous term in the radiation, following [Coughlin & Begelman \(2014\)](#), to diffuse the shocks, as presented in Appendix B of [Sądowski et al. \(2015\)](#).

The viscous term is given by:

$$R_{\text{visc}}^{\mu\nu} = -2v_{\text{rad}}\tilde{E}\sigma_R^{\mu\nu}, \quad (3.22)$$

where  $v_{\text{rad}} = \alpha_{\text{rad}}\lambda$  is the radiative viscosity coefficient, defined as the product of a constant  $\alpha_{\text{rad}}$  coefficient<sup>5</sup> and photon's mean free path  $\lambda$ .  $\sigma_R^{\mu\nu}$  is the shear tensor,

$$\sigma_R^{\mu\nu} = \frac{1}{2} (u_{R;\alpha}^{\mu} h_R^{\alpha\nu} + u_{R;\alpha}^{\nu} h_R^{\alpha\mu}) - \frac{1}{3} h_R^{\mu\nu}, \quad (3.23)$$

where  $h_R^{\mu\nu} = g^{\mu\nu} + u_R^{\mu} u_R^{\nu}$  is the projection tensor.

The viscosity term is suppressed in the optically thick regions by setting  $\lambda = \min\left(r, \frac{1}{\rho\chi}\right)$ . The maximal value of  $v_{\text{rad}}$  is also limited to ensure that the CFL condition is not violated. In the end, the viscous term is added to the radiative fluxes in the **M1** scheme as

$$R^{i\nu} = R^{i\nu} + R_{\text{visc}}^{i\nu}. \quad (3.24)$$

### 3.1.4. Mean field dynamo

The main engine for angular momentum transport in the accretion disk is the MRI, yet it also leads to the dissipation of magnetic energy and fading of the magnetic field. However, the magnetic field is simultaneously replenished due to the mean-field dynamo effect. This process naturally occurs in 3D simulations, where all three components of  $\mathbf{B}$  are evolved. In 2D simulations, on the other hand, the axisymmetry prevents the generation of the poloidal component of

<sup>5</sup> typical value is  $\alpha_{\text{rad}} = 0.1$  based on calculations and simulations in [Sądowski et al. \(2015\)](#)



the magnetic field, as implied by Cowling's anti dynamo theorem (Brandenburg et al. 1995; Cowling 1933; Sądowski et al. 2015).

Therefore, a 2D simulation cannot last for a prolonged time due to the decaying magnetic field (estimations maximal duration is about  $5000 t_g$ ), but the decay can still influence the results even in earlier stages. In Sądowski & Narayan (2016), a set of very long 3D simulations of super-Eddington accretion was published, and one of them was compared to a 2D simulation of the same parameters. The results confirmed that the artificial mean-field dynamo implemented in the KORAL code enables extremely long 2D simulations with time-averaged properties almost identical to the 3D runs; however, the time variability and radiative luminosity were notably higher in the dynamo simulations. Even though the dynamical properties of the flow are captured well, one should keep in mind that only a full 3D treatment of the problem can lead to reliable results.

The saturated state, when the dynamo term counterbalances the magnetic dissipation, corresponds to a state when the magnetization  $\beta$  and the magnetic tilt angle  $\xi$  are

$$\beta = \frac{P_{\text{mag}}}{P_{\text{gas}}} \approx 0.1 \quad (3.25)$$

$$\xi = \frac{b^r b^\phi}{b^2} \approx \frac{\mathbf{B}_{\hat{p}}}{B_{\hat{\phi}}} \approx 0.25, \quad (3.26)$$

where  $B_{\hat{p}}$  and  $B_{\hat{\phi}}$  are the orthonormal poloidal and azimuthal components of the magnetic field (Sorathia et al. 2012). The mean magnetic field evolution equation (Brandenburg 2001) can be written as

$$\frac{\partial}{\partial t} \mathbf{B} = \alpha_{\text{dyn}} \nabla \times \mathbf{B} + \eta_{\text{md}} \Delta \mathbf{B}, \quad (3.27)$$

where  $\alpha_{\text{dyn}}$  is the dynamo coefficient and  $\eta_{\text{md}}$  the magnetic diffusivity coefficient. To balance the magnetic diffusion by the generation of a poloidal magnetic field, the (3.27) can be rewritten as:

$$\frac{\partial}{\partial t} \mathbf{B}_{\hat{p}} = \alpha_{\text{dyn}} (\nabla \times \mathbf{B})_{\hat{p}} \quad (3.28)$$

Using the assumption of Keplerian motion (the magnetic field is generated on the dynamical timescale  $1/\Omega_K$ ) and the magnitude of poloidal current  $|\mathbf{J}_{\hat{p}}| \approx |B_{\hat{\phi}}|/H$ , where  $H$  is the half-thickness of the disk, the increment of the azimuthal vector potential is

$$\frac{\partial}{\partial t} A_{\hat{\phi}} = \alpha_{dyn} \xi \Omega_K B_{\hat{\phi}}. \quad (3.29)$$

To prevent over-saturation of the magnetic field, errors in the plunging regions, and excessively high  $\xi$  values, the KORAL code introduces factors that control the intensity of the dynamo process, as described in Appendix A of [Sądowski et al. \(2015\)](#).

After generating the magnetic field through the dynamo process, the new magnetic field increment  $d\mathbf{B}_{dyn}$  is added to the existing magnetic field by computing the curl of  $d\mathbf{A}_{dyn}$ :  $d\mathbf{B}_{dyn} = \nabla \times d\mathbf{A}_{dyn}$ . Subsequently, the azimuthal component  $B^\phi$  is damped to maintain saturated values of  $\xi$ . This damping process ensures that the dynamo-generated magnetic field does not become too dominant, leading to unrealistic behaviour or numerical issues.

## 3.2. Numerical methods

The conservation laws (3.1)-(3.2) in the coordinate basis of  $(t, x^i)$  are given by ([Gammie et al. 2003](#))

$$\frac{\partial}{\partial t} (\sqrt{-g} \rho u^t) + \frac{\partial}{\partial x^i} (\sqrt{-g} \rho u^i) = 0, \quad (3.30)$$

$$\frac{\partial}{\partial t} (\sqrt{-g} T^t{}_\nu) + \frac{\partial}{\partial x^i} (\sqrt{-g} T^i{}_\nu) = \sqrt{-g} T^\alpha{}_\beta \Gamma^\beta{}_{\nu\alpha} + \sqrt{-g} G_\nu, \quad (3.31)$$

$$\frac{\partial}{\partial t} (\sqrt{-g} R^t{}_\nu) + \frac{\partial}{\partial x^i} (\sqrt{-g} R^i{}_\nu) = \sqrt{-g} R^\alpha{}_\beta \Gamma^\beta{}_{\nu\alpha} - \sqrt{-g} G_\nu, \quad (3.32)$$

where  $\Gamma^\alpha{}_{\beta\gamma}$  are the Christoffel symbols describing the spacetime curvature.

However, this form is not stable in numerical schemes because it takes the values of the right-hand side as exact from the cell centres when the left-hand sides spatial derivatives are not exact results of the numerical differential. Thus, in the KORAL code, a static metric is expected, and the equations can be written as

$$\frac{\partial}{\partial t} (\rho u^t) + \frac{\partial}{\partial x^i} (\rho u^i) = \frac{-\rho u^i}{\sqrt{-g}} \frac{\partial}{\partial x^i} \sqrt{-g}, \quad (3.33)$$

$$\frac{\partial}{\partial t} (T^t{}_\nu) + \frac{\partial}{\partial x^i} (T^i{}_\nu) = T^\alpha{}_\beta \Gamma^\beta{}_{\nu\alpha} - \frac{T^i{}_\nu}{\sqrt{-g}} \frac{\partial}{\partial x^i} \sqrt{-g} + G_\nu, \quad (3.34)$$

$$\frac{\partial}{\partial t} (R^t{}_\nu) + \frac{\partial}{\partial x^i} (R^i{}_\nu) = T^\alpha{}_\beta \Gamma^\beta{}_{\nu\alpha} - \frac{R^i{}_\nu}{\sqrt{-g}} \frac{\partial}{\partial x^i} \sqrt{-g} - G_\nu. \quad (3.35)$$

These modified equations ensure numerical stability in the simulations.

The KORAL code solves a system of differential equations (3.33)-(3.35) using the finite volume Godunov scheme, which in general solves

$$\frac{\partial}{\partial t} \mathbf{Q} + \nabla \cdot \mathbf{F}(\mathbf{Q}) = \mathbf{S}(\mathbf{Q}), \quad (3.36)$$

in other words, the time change of some vector quantity  $\mathbf{Q}$  plus the divergence of the flux of  $\mathbf{Q}$  is equal to the source of  $\mathbf{Q}$ . The finite-volume method means that (3.36) is calculated in a finite-volume element.

In a first-order Godunov scheme, the state at the time  $(t + \Delta t)$  is computed using the averaged value of  $\mathbf{Q}$  in the whole cell, minus fluxes through all cell faces and then adding the source term. In a second-order Godunov scheme, values at  $(t + \Delta t)/2$  are used to advance the whole system in time. The second-order scheme generally provides more accuracy compared to the first-order scheme, but it also requires more computational resources.

### 3.2.1. The Riemann problem

The complementary problem involves solving the flux through neighbouring cells. In a discrete code, the fluxes at cells' faces are reconstructed from the values at the centres since all cells are considered homogeneous. At each interface between two cells, a discontinuity exists, resulting in two values of flux: the left  $\mathbf{F}^L$  and right  $\mathbf{F}^R$  flux (see Figure 3.1). To find the total flux through the cell face, a Riemann problem, a well-known problem in hydrodynamics, has to be solved.

A one-dimensional Riemann problem can be represented by a tube containing two fluids in different states separated by a thin membrane. Once the membrane is removed, the fluids mix and the time evolution of this state is the Riemann problem. A semi-analytical solution can be found in specific cases, such as the Sod tube problem Sod (1978).

However, in 2D simulation, the Riemann solver needs to be called four times for each cell at each time step, and in 3D simulation, it needs to be called six times for each cell at each time step. Furthermore, in the case of radiative MHD, the problem has to be solved separately for the gas and radiation. Implementing a precise yet complex solver can thus significantly influence the computational load. For this reason, an approximate solver is usually implemented in MHD codes. One such solver is the HLL (Harten–Lax–van Leer) Riemann solver (Harten et al. 1983), which is also implemented in KORAL.

The HLL solver approximates the solution by the superposition of left and right moving waves, corresponding to the minimal and maximal velocity of the signal in the fluid. If the left and right maximal speeds,  $S^L$  and  $S^R$ , are derived, the flux through a cell face is given by

$$\mathbf{F} = \begin{cases} \mathbf{F}^L & 0 < S^L \\ \frac{S^R \mathbf{F}^L - S^L \mathbf{F}^R + S^L S^R (\mathbf{Q}^R - \mathbf{Q}^L)}{S^R - S^L} & S^L \leq 0 \leq S^R, \\ \mathbf{F}^R & S^R < 0 \end{cases}, \quad (3.37)$$

where  $\mathbf{Q}^R$  and  $\mathbf{Q}^L$  are the right and left state respectively (Toro 2009).

This method also imposes a constrain on the size of the time step  $\Delta t$ , since the maximal signal speed  $S^{\max}$  in a cell cannot exceed  $\Delta x / \Delta t$ , where  $\Delta x$  is the cell size. Otherwise, the signal would traverse the entire cell and influence fluxes on both faces within a single time step. This constraint on the maximum  $\Delta t$  size is known as the Courant–Friedrichs–Lewy (CFL) condition and can be expressed as

$$\frac{S^{\max} \Delta t}{\Delta x} \leq C, \quad (3.38)$$

where  $C < 1$ . Choosing a low value of  $C$  leads to more precise results at the price of significantly increasing the computational load.

### 3.2.2. Implicit-explicit time-stepping

In the optically thick regime, the  $G^V$  may become much larger than the conserved quantities, and the evolution equation stiff, requiring an implicit solver to evolve it. In the KORAL code, the second order Runge-Kutta implicit-explicit (IMEX) stepper is implemented, following Pareschi et al. (2005) and (Sądowski et al. 2015).

The implicit scheme in the KORAL code evolves the time and spatial derivatives in (3.35) and (3.34) separately, as the advection term is stable in the explicit step due to the speed of light limit, which restricts the time step size  $\Delta t$ . The time derivative is then found implicitly as

$$T^t_{\mathbf{v}}(t + \Delta t) - T^t_{\mathbf{v}}(t) = \Delta t G_{\mathbf{v}}(t + \Delta t) \quad (3.39)$$

$$R^t_{\mathbf{v}}(t + \Delta t) - R^t_{\mathbf{v}}(t) = -\Delta t G_{\mathbf{v}}(t + \Delta t), \quad (3.40)$$

which leads to a system of four equations due to the conservation laws. This system is solved for the primitive quantities. The IMEX scheme calculates the explicit and implicit terms together, enabling an efficient and accurate evolution of the optically thick fluid (for detailed description, see, e.g., [McKinney et al. 2014](#)).

In addition to the IMEX scheme, the KORAL code offers other time-stepping solvers, such as the standard explicit Runge-Kutta in the first or second order or the Heun solver. However, the IMEX scheme is considered the best choice for problems involving optically thick fluids, as it efficiently handles the stiff behaviour of the equations.

### 3.2.3. Conserved and primitives variables and reconstruction scheme

In equation (3.36), the fluxes and source terms on the left-hand side can be expressed as simple functions of a well-defined set of primitive quantities that naturally describe the flow, such as the density, velocity, and internal energy. However, these quantities are not conserved during evolution. Fortunately, it is possible to find another set of quantities such that they are also functions of the primitives and are conserved during evolution. Equation (3.36) can be then rewritten as:

$$\frac{\partial}{\partial t} \mathbf{U}(\mathbf{P}) + \nabla \cdot \mathbf{F}(\mathbf{P}) = \mathbf{S}(\mathbf{P}), \quad (3.41)$$

where  $\mathbf{U}$  and  $\mathbf{P}$  are the vectors of conserved and primitive quantities, respectively.

The number of equations to solve in MHD codes depends on the included physics; for the case of the puffy disk simulations, using 3D GRMHD and radiation, there are 12 equations and 13 primitives. Specifically, six for the hydrodynamics part, three for the magnetic field and 4 for the radiation. The vectors of primitive and conserved quantities are:

$$\mathbf{P} = [\rho, u_{\text{int}}, u^\mu / u^t, S, B^i, \tilde{E}, \tilde{F}^i], \quad (3.42)$$

$$\mathbf{U} = [\rho u^t, T_t^t + \rho u^t, T_i^t, B^i, R_t^t, R_i^t], \quad (3.43)$$

where the one extra primitive,  $S$ , is the gas entropy per unit volume.

The entropy is used in the case of a cold gas when  $u_{\text{int}} \ll \rho$  and the numerical scheme can lead to negative values of  $u_{\text{int}}$ . At the end of each time step, the entropy is calculated and stored in the vector of primitives (Sądowski et al. 2013). The entropy is given by

$$S = \frac{\rho}{\Gamma - 1} \ln \frac{p}{\rho^\Gamma} \quad (3.44)$$

and evolved as

$$(Su^\mu)_{;\mu} = 0. \quad (3.45)$$

The order of the primitives in (3.42) is kept the same as in the code to distinguish between the HD ( $\rho, u_{\text{int}}, u^\mu / u^t, S$ ), magnetic ( $B^i$ ) and radiation ( $\tilde{E}, \tilde{F}^i$ ) part. In the code, the number of primitives changes depending on the set-up; e.g., if the photon number conserving Comptonization is also included, the number of primitives is 14; for two-temperature plasma or relativistic electrons, it is much more.

The conversion from primitives to conserved quantities (p2u) is relatively straightforward. However, the inversion from conserved to primitives (u2p) is much more complicated, especially in the case of GRMHD (and even in the special relativistic MHD) because the u2p relations consist of an open set of nonlinear equations that must be solved numerically. u2p has to be performed at least once at each time step and, in the case of the second-order precision in KORAL, even twice. Therefore, a fast and precise method for the inversion is crucial for running the simulations effectively.

The u2p inversion scheme in GRMHD involves solving an open set of algebraic equations, for which the Newton-Raphson method is often used. Reducing the number of equations to solve is convenient to optimise the calculations. The algorithm implemented in the KORAL code is well described in Noble et al. (2006).

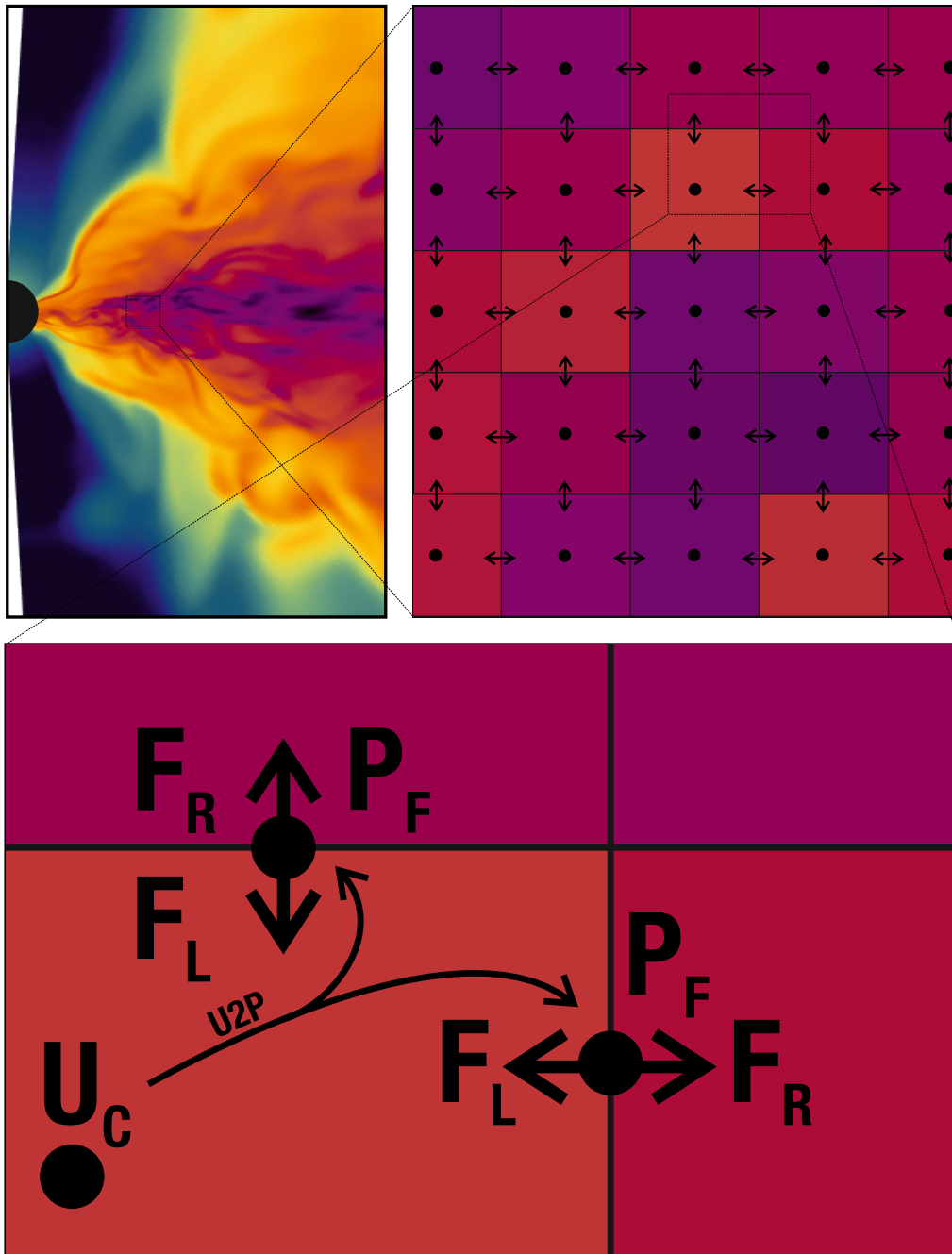


**Figure 3.1.** Illustration of the MHD algorithm in 2D. *Top left:* Snapshot of a density map from accretion disk simulation. *Top right:* Zoom in onto the grid, which consists of homogeneous cells. The cell centres and fluxes are indicated. *Bottom:* Zoom-in on a cell boundary, showing the conserved quantities stored at the cell centres and left and right fluxes through the cells' faces, which are calculated from the primitives reconstructed at the faces. To solve the total flux through each cell face, the Riemann problem is solved.

Several backup mechanisms are also implemented in the code in case the inversion fails, such as applying entropy inversion if the flow is too cold, as described above. If all backup mechanisms fail, the code can also interpolate the faulty cell values from surrounding cells. In this case, the cell is flagged, the number of these fix-ups is summed over the whole domain, and the user is notified in the log. These cells also cannot be used for interpolation in another cell. If more of such cells are next to each other, interpolation cannot be performed, the values of the primitives are set to the floor values, and the code will produce a warning to the user that there is a zone with a potential problem, where the u2p inversion is failing, and the results can be unphysical.

The inversion is done separately for the MHD and radiation primitives, but the inversion scheme is almost identical. After each inversion, the floors are applied if obtained values reach them.

A related problem is calculating values of primitive quantities in different parts of a cell. The values are needed at the cell faces to calculate the fluxes. However, the values stored are at the cell centre, so the values of primitives at each face have to be *reconstructed* to be consistent with the state of the fluid and avoid producing artificial shocks while not smoothing out large physical shocks. Therefore, these numerical schemes are usually referred to as shock-capturing schemes.

Several reconstruction schemes are implemented in the KORAL code, including the *minmod* limiter. This scheme is controlled by only one diffusivity parameter  $\theta_{MM}$  (Sądowski et al. 2013). Here,  $\theta_{MM} = 1$  corresponds to the diffusive van Leer scheme, and  $\theta_{MM} = 2$  to the monotonized central scheme. In simulations,  $\theta_{MM} = 1.5$  is usually the best choice (see van Leer (1979) and references therein).

### 3.3. Running KORAL

KORAL is written in the C programming language, employing numerical methods from the GSL library (Galassi & Gough 2009) and using the VisIt library for visualization (Childs et al. 2012). The structure of the code consists of 5 header files, 19 C files, and a folder OPACITIES, where the tabular opacities introduced in Sądowski et al. (2017) are stored; this forms the core of the code. The user-defined problems are saved in the PROBLEMS folder. Anything that is problem-specific should be implemented in a separate folder stored within the PROBLEMS folder. Each problem folder must include an `init.c` file, where the initial state is defined. Another mandatory file for each problem is the `define.h`



```

Precalculating metrics... done!
*****
BH mass: 10.000000
spin: 0.000000
scalings (G--CGS):
rho: 6.172971e+15
ndot: 4.037160e+38
sigma: 9.117470e+11
len: 1.477000e+06
time: 4.926742e+05
endend: 5.547309e+36
Flux: 1.662345e+47
T(1,1): 7.258797e+12
kbt: 9.184259e+14
kb/me: 1.686367e-10
sigma_rad: 3.409218e-52
kappa: 1.806795e+22
ct: 1.126097e+41
mass: 1.989004e+34

rhorizonBL: 2.000000
rISCOBL: 6.000000
etaM: 0.057191

->ndotEdd: 1.656605e+19
->lumEdd: 2.902734e+20
GM2: 1.477000e+06
GM3: 4.926742e+05
*****
st #166065 t= 7.900e+04 dt=2.98e-03 npi=0.0 zmps=13174658 fail# 0 0 0 ent# 0 0 388820121 0 37964420 imp# 2325840 0 0 0 0 5.6 0.0 0.0 0.0 0.0
st #166066 t= 7.900e+04 dt=2.98e-03 npi=0.0 zmps=13096571 fail# 0 0 0 ent# 0 0 38810719 0 37999524 imp# 2325840 0 0 0 0 5.6 0.0 0.0 0.0 0.0
st #166067 t= 7.900e+04 dt=2.98e-03 npi=0.0 zmps=13116210 fail# 0 0 0 ent# 0 0 3881300 26 0 37975138 imp# 2325840 0 0 0 0 5.6 0.0 0.0 0.0 0.0
st #166068 t= 7.900e+04 dt=2.98e-03 npi=0.0 zmps=12137883 fail# 0 0 0 ent# 0 0 38882735 0 388067150 imp# 2325840 0 0 0 0 5.6 0.0 0.0 0.0 0.0
st #166069 t= 7.900e+04 dt=2.98e-03 npi=0.0 zmps=13283959 fail# 0 0 0 ent# 0 0 3881300 26 0 37975138 imp# 2325840 0 0 0 0 5.6 0.0 0.0 0.0 0.0
st #166070 t= 7.900e+04 dt=2.98e-03 npi=0.0 zmps=12395567 fail# 0 0 0 ent# 0 0 38812028 0 38805134 imp# 2325840 0 0 0 0 5.6 0.0 0.0 0.0 0.0
st #166071 t= 7.900e+04 dt=2.98e-03 npi=0.0 zmps=12206261 fail# 0 0 0 ent# 0 0 38886913 0 37980941 imp# 2325840 0 0 0 0 5.6 0.0 0.0 0.0 0.0
st #166072 t= 7.900e+04 dt=2.98e-03 npi=0.0 zmps=12333309 fail# 0 0 0 ent# 0 0 3889232 0 389146134 imp# 2325840 0 0 0 0 5.6 0.0 0.0 0.0 0.0
st #166073 t= 7.900e+04 dt=2.98e-03 npi=0.0 zmps=12992488 fail# 0 0 0 ent# 0 0 38884234 0 37977636 imp# 2325840 0 0 0 0 5.6 0.0 0.0 0.0 0.0
st #166074 t= 7.900e+04 dt=2.98e-03 npi=0.0 zmps=12766319 fail# 0 0 0 ent# 0 0 388868136 0 388000423 imp# 2325840 0 0 0 0 5.6 0.0 0.0 0.0 0.0
st #166075 t= 7.900e+04 dt=2.98e-03 npi=0.0 zmps=13191845 fail# 0 0 0 ent# 0 0 388882135 0 379762145 imp# 2325840 0 0 0 0 5.6 0.0 0.0 0.0 0.0
st #166076 t= 7.900e+04 dt=2.98e-03 npi=0.0 zmps=12774763 fail# 0 0 0 ent# 0 0 38886242 0 379889152 imp# 2325840 0 0 0 0 5.6 0.0 0.0 0.0 0.0
st #166077 t= 7.900e+04 dt=2.98e-03 npi=0.0 zmps=12831302 fail# 0 0 0 ent# 0 0 388896148 0 379891147 imp# 2325840 0 0 0 0 5.6 0.0 0.0 0.0 0.0
st #166078 t= 7.900e+04 dt=2.98e-03 npi=0.0 zmps=11724732 fail# 0 0 0 ent# 0 0 388878145 0 388004150 imp# 2325839 1 0 0 0 5.6 0.0 0.0 0.0 0.0
st #166079 t= 7.900e+04 dt=2.98e-03 npi=0.0 zmps=13068440 fail# 0 0 0 ent# 0 0 388878152 0 379953168 imp# 2325840 0 0 0 0 5.6 0.0 0.0 0.0 0.0
st #166080 t= 7.900e+04 dt=2.98e-03 npi=0.0 zmps=11558927 fail# 0 0 0 ent# 0 0 387981143 0 379657149 imp# 2325840 0 0 0 0 5.6 0.0 0.0 0.0 0.0
st #166081 t= 7.900e+04 dt=2.98e-03 npi=0.0 zmps=12804565 fail# 0 0 0 ent# 0 0 387982133 0 379740140 imp# 2325840 0 0 0 0 5.6 0.0 0.0 0.0 0.0
st #166082 t= 7.900e+04 dt=2.98e-03 npi=0.0 zmps=12926394 fail# 0 0 0 ent# 0 0 387861112 0 379820115 imp# 2325840 0 0 0 0 5.6 0.0 0.0 0.0 0.0
st #166083 t= 7.900e+04 dt=2.98e-03 npi=0.0 zmps=13178978 fail# 0 0 0 ent# 0 0 387838115 0 379667122 imp# 2325840 0 0 0 0 5.6 0.0 0.0 0.0 0.0
st #166084 t= 7.900e+04 dt=2.98e-03 npi=0.0 zmps=12759429 fail# 0 0 0 ent# 0 0 387905119 0 379853124 imp# 2325840 0 0 0 0 5.6 0.0 0.0 0.0 0.0
st #166085 t= 7.900e+04 dt=2.98e-03 npi=0.0 zmps=13053769 fail# 0 0 0 ent# 0 0 38782020 0 379968124 imp# 2325840 0 0 0 0 5.6 0.0 0.0 0.0 0.0
st #166086 t= 7.900e+04 dt=2.98e-03 npi=0.0 zmps=12639783 fail# 0 0 0 ent# 0 0 387953126 0 379822130 imp# 2325840 0 0 0 0 5.6 0.0 0.0 0.0 0.0
st #166087 t= 7.900e+04 dt=2.98e-03 npi=0.0 zmps=13040099 fail# 0 0 0 ent# 0 0 387992130 0 379630139 imp# 2325840 0 0 0 0 5.6 0.0 0.0 0.0 0.0
st #166088 t= 7.900e+04 dt=2.98e-03 npi=0.0 zmps=12608974 fail# 0 0 0 ent# 0 0 387930133 0 379839140 imp# 2325840 0 0 0 0 5.6 0.0 0.0 0.0 0.0
st #166089 t= 7.900e+04 dt=2.98e-03 npi=0.0 zmps=1129061 fail# 0 0 0 ent# 0 0 387961138 0 379783149 imp# 2325840 0 0 0 0 5.6 0.0 0.0 0.0 0.0
st #166090 t= 7.900e+04 dt=2.98e-03 npi=0.0 zmps=12622766 fail# 0 0 0 ent# 0 0 387990138 0 379846149 imp# 2325840 0 0 0 0 5.6 0.0 0.0 0.0 0.0
st #166091 t= 7.900e+04 dt=2.98e-03 npi=0.0 zmps=13883555 fail# 0 0 0 ent# 0 0 387846134 0 379849143 imp# 2325840 0 0 0 0 5.7 0.0 0.0 0.0 0.0
st #166092 t= 7.900e+04 dt=2.98e-03 npi=0.0 zmps=1294693 fail# 0 0 0 ent# 0 0 387920132 0 379962137 imp# 2325840 0 0 0 0 5.7 0.0 0.0 0.0 0.0
st #166093 t= 7.900e+04 dt=2.98e-03 npi=0.0 zmps=13079247 fail# 0 0 0 ent# 0 0 387882138 0 379577144 imp# 2325840 0 0 0 0 5.7 0.0 0.0 0.0 0.0
st #166094 t= 7.900e+04 dt=2.98e-03 npi=0.0 zmps=13013093 fail# 0 0 0 ent# 0 0 387763135 0 379863139 imp# 2325840 0 0 0 0 5.7 0.0 0.0 0.0 0.0
st #166095 t= 7.900e+04 dt=2.98e-03 npi=0.0 zmps=13098868 fail# 0 0 0 ent# 0 0 387789138 0 379696142 imp# 2325840 0 0 0 0 5.7 0.0 0.0 0.0 0.0
st #166096 t= 7.900e+04 dt=2.98e-03 npi=0.0 zmps=12825990 fail# 0 0 0 ent# 0 0 387771142 0 379726154 imp# 2325840 0 0 0 0 5.7 0.0 0.0 0.0 0.0
st #166097 t= 7.900e+04 dt=2.98e-03 npi=0.0 zmps=13066137 fail# 0 0 0 ent# 0 0 387861147 0 379932151 imp# 2325839 1 0 0 0 5.7 0.0 0.0 0.0 0.0
st #166098 t= 7.900e+04 dt=2.98e-03 npi=0.0 zmps=12915265 fail# 0 0 0 ent# 0 0 387828139 0 379836144 imp# 2325840 0 0 0 0 5.7 0.0 0.0 0.0 0.0
st #166099 t= 7.900e+04 dt=2.98e-03 npi=0.0 zmps=12786958 fail# 0 0 0 ent# 0 0 387888144 0 380039152 imp# 2325840 0 0 0 0 5.7 0.0 0.0 0.0 0.0
st #166100 t= 7.900e+04 dt=2.98e-03 npi=0.0 zmps=13092785 fail# 0 0 0 ent# 0 0 387827134 0 379938140 imp# 2325839 1 0 0 0 5.7 0.0 0.0 0.0 0.0
st #166101 t= 7.900e+04 dt=2.98e-03 npi=0.0 zmps=12780466 fail# 0 0 0 ent# 0 0 387810141 0 379868149 imp# 2325840 0 0 0 0 5.7 0.0 0.0 0.0 0.0
st #166102 t= 7.900e+04 dt=2.98e-03 npi=0.0 zmps=13053058 fail# 0 0 0 ent# 0 0 387889120 0 380004123 imp# 2325840 0 0 0 0 5.7 0.0 0.0 0.0 0.0

```

**Figure 3.2.** Example of KORAL log output. *Left:* The log printed right after the start shows general information about the set-up, including the BH mass and spin in the case of BH simulation, as well as scalings from the code units to the cgs units. *Right:* Example of the log output during the run, including the step number and time in the simulation, the current time step size, MPI load, number of zones calculated per second, number of fails (i.e., failed u2p conversions in MHD or radiation part), and information about the implicit solver.

header, which includes a setup for the code, parameters of the spacetime and grid, or modifiers to the standard options or constants.

Other optional files can be included, such as `preinit.c` or `postinit.c`, which are called before and after initialization, respectively, and can include specific tools or modifiers for the initial state. The `kappa.c` and `kappaes.c` files allows the user to define their prescriptions for the absorption and electron scattering opacity. A `finger.c` file can be called at the beginning of each time step, e.g., to extract specific data or modify something. Additionally, `bc.c` can be included, in which problem-specific boundary conditions are defined. The particular problem to be solved using the KORAL core is specified in file `problem.h` in the root directory.

The code also includes separate tools to process or modify the output data, such as tools for slicing and averaging over some plane, exporting outputs in more convenient hdf5 format, averaging the results over specific time windows, or changing the resolution. Additionally, there is a tool that enables turning on the radiation or other options of the code. Since the primitives are saved in the binary output files as a 1D array, if the number of primitives changes (e.g., by including radiation or photon number conserving), the entire structure of the binary file needs to be changed.

The code is heavily parallelized using the message-passing interface (MPI), enabling simulations to run on supercomputers with a large number of nodes and

individual CPUs. Each node then process-specific part of the grid, and the values at the boundary are passed between them through the MPI. Simulations of the puffy disk were performed thanks to obtaining several grants at supercomputer Prometheus within the PLGRID infrastructure.

### 3.3.1. KORAL algorithm

Having described important procedures required for GRRMHD in the previous sections, the algorithm of KORAL can be summarized as follows:

1. First, the code searches for an existing binary file to restart the simulation. If none is found, the `init.c` initializes a new simulation. The initial state is always saved to a separate array for the boundary condition calculations or other operations if needed.
2. Ghost cells are filled using values corresponding to the boundary conditions. The number of ghost cells depends on the order of the reconstruction scheme, and typically, it is between 3 and 5 in each direction. They are required for the flux calculations through the outer edges of the domain. Ghost cells are not evolved in time.
3. Re-scaling or perturbation of the initial state is performed if defined by the user. For instance, when initializing an accretion disk with a stable torus, the azimuthal fluid velocity may be perturbed to trigger the MRI.
4. The main time loop begins with the initial time step size  $\Delta t$  estimated from characteristic wave speeds in the smallest cell. In the following steps,  $\Delta t$  is calculated during the explicit step from the CFL condition.
5. User-defined `finger.c` is applied, and data distribution through MPI is performed when running on a cluster.
6. The first implicit and explicit steps are performed to obtain the intermediate values, followed by the first u2p inversion. Data are exchanged over MPI, ghost cells' values are determined from the boundary conditions, and the dynamo term is applied in a 2D simulation.
7. The first IMEX step is performed to obtain the intermediate values.
8. Second implicit and explicit steps are done in the same manner as before, but using the intermediate values.
9. The second IMEX step advances the whole solution in time.
10. Second u2p inversion is performed, and the entropy is calculated and stored in primitives.
11. At the end of each time step, the total number of failed u2p inversions is counted, and the number of iterations of the implicit solver and performance

marks are calculated. All relevant information is printed into the log for the user to control the simulation status.

The explicit and implicit steps include all manipulations with the primitives, reconstruction scheme, and Riemann problem-solving. The explicit step includes

1. Primitives are reconstructed on the cell borders, and left and right fluxes are calculated.
2. Riemann problem is solved using the HLL solver to calculate fluxes through all cell faces. The magnetic fluxes are determined using the CT to enforce  $\nabla \cdot \mathbf{B} = 0$  constraint.
3. The time step  $\Delta t$  is calculated using the wave speed in each cell. The minimal value across the whole domain is then used everywhere.
4. Conserved quantities in  $(t + \Delta t)$  are calculated using (3.41).

In the implicit step, the energy of the radiation and the fluid is compared in each cell. Then, the one which stores less energy is evolved implicitly, using the original values of primitives as the first guess. If a solution is not found in some cell after a predefined number of iterations, the values are interpolated from neighbouring cells, flagged, and printed in the log for the user.

KORAL saves its outputs into binary files as often as the user defines. The code can read these binary files, restart the simulations from a certain point, or process them via several complementary scripts for different purposes. If it runs on a serial machine, the code can directly create a `VisIt .silo` files, where most of the essential quantities are saved, which is helpful for a fast check of the run or tuning of the initial setup.

### 3.3.2. Computational grid and resolution

A correct choice of computational grid parameters is fundamental in MHD simulations, as it must have a sufficient resolution to resolve the low-scale turbulences while considering computational demands. The smaller cell size leads to a smaller  $\Delta t$ , as evident from the CFL condition (equation 3.38). The issue becomes even more complex in the case of the GR due to singularities in the commonly used coordinate systems. However, the coordinate singularities can be removed by adopting the Kerr-Schild (KS) coordinates (Kerr & Schild 2009).

To achieve an ideal resolution, the cells must be smaller in the inner region and the midplane of the accretion disk, usually at the equatorial plane. This can be easily achieved using the modified Kerr-Schild (MKS) coordinates (McKinney & Gammie 2004). Nevertheless, the simulation outputs are most conveniently stored in Boyer–Lindquist (BL) coordinates (Boyer & Lindquist 1967).

Transformation relations between all three in the Kerr metric for a rotating BH are described below.

The BL coordinates are  $(t, r, \theta, \phi)$ , and the Kerr metric in BL coordinates is given by (2.12). The determinant of the metric is  $g = -\Sigma^2 \sin^2 \theta$ .

In the KS coordinates,  $(t, r, \theta, \phi)$ , the Kerr metric is expressed as:

$$\begin{aligned} ds^2 = & - \left(1 - \frac{2r}{\Sigma}\right) dt^2 + \left(\frac{4r}{\Sigma}\right) dr dt + \left(1 + \frac{2r}{\Sigma}\right) dr^2 + \Sigma d\theta^2 \\ & + \sin^2 \theta \left[ \Sigma + a^2 \left(1 + \frac{2r}{\Sigma}\right) \sin^2 \theta \right] d\phi^2 \\ & - \left(\frac{4ar \sin^2 \theta}{\Sigma}\right) d\phi dt - 2a \left(1 + \frac{2r}{\Sigma}\right) \sin^2 \theta d\phi dr, \end{aligned} \quad (3.46)$$

and the determinant is  $g = \Sigma^2 \sin^2 \theta$ . The  $r$  and  $\theta$  coordinates are the same as in the BL coordinates,  $r^{\text{KS}} = r^{\text{BL}}$  and  $\theta^{\text{KS}} = \theta^{\text{BL}}$ .

Implementing the MKS coordinates provides the advantage of using a logarithmic grid, which concentrates the resolution in  $r$  and  $\theta$  direction. The transformations for  $t^{\text{MKS}}$  and  $\phi^{\text{MKS}}$  remain the same as in the KS coordinates, and the other coordinates transform as

$$r^{\text{KS}} = R_0 + \exp(r^{\text{MKS}}), \quad (3.47)$$

$$\theta^{\text{KS}} = \left\{ \frac{\tan [H_0 \pi (\theta^{\text{MKS}} - \frac{1}{2})]}{\tan (\frac{\pi}{2} H_0)} + 1 \right\} \frac{\pi}{2}, \quad (3.48)$$

where  $R_0$  and  $H_0$  are parameters controlling how much are the cells concentrated in  $r$  and  $\theta$  directions. The expression for  $\theta$  transformation is a slightly modified version of the MKS coordinates presented in [McKinney & Gammie \(2004\)](#).

Other coordinate systems are implemented in the KORAL code, e.g., cylindrical coordinates covering precisely the polar regions to resolve the jets, similar to those introduced in [Ressler et al. \(2017\)](#).

However, internally the code considered all cells as cubes, and the coordinate transformation is applied only when necessary.

### 3.3.3. Resolving the MRI

One challenge of the GRMHD is the scalability of turbulences, which makes it difficult to achieve fully converged solutions that resolve turbulences on all

scales. When changing the resolution, convergence in an accretion disk GRMHD simulation is typically determined by the stability of important parameters (e.g., mass accretion rate, density scale height, radiative luminosity). However, increasing resolution to reach convergence is impractical and computationally expensive.

In studies by [Hawley et al. \(2011, 2013\)](#), quality parameters were derived to assess simulation convergence based on the assumption that the characteristic wavelength of the MRI must be well resolved so the MRI-induced turbulences are maintained. Although satisfying these conditions is important for obtaining reliable and physical results, limitations and approximations of the GRMHD must still be considered.

The quality parameters,  $Q_\theta$  and  $Q_\phi$ , correspond to the ratio of the cell size to the characteristic MRI wavelength

$$\lambda_{\text{MRI}} = \frac{2\pi v^A}{\Omega}, \quad (3.49)$$

where  $v^A$  is the Alfvén speed and  $\Omega$  is orbital frequency. The quality parameters are then defined as

$$Q_\theta = \frac{\lambda_{\text{MRI}}}{\Delta\theta} = \frac{2\pi |v_\theta^A|}{\Omega\Delta\theta}, \quad (3.50)$$

$$Q_\phi = \frac{\lambda_{\text{MRI}}}{r\Delta\phi} = \frac{2\pi |v_\phi^A|}{\Omega\Delta\phi}. \quad (3.51)$$

To maintain the turbulences, the non-linear growth of MRI has to be resolved, which couples both parameters. If  $\langle Q_\phi \rangle \geq 20$ , then  $\langle Q_\theta \rangle \geq 10$  is needed. However, if  $\langle Q_\phi \rangle$  is lower,  $\langle Q_\theta \rangle$  can compensate if it is high enough ([Hawley et al. 2011](#)).



## Chapter 4

# Puffy accretion disk

The puffy disk is a numerical model of an accretion disk based on the results of the GRRMHD simulation, targeted to study properties and behaviour of sub-Eddington accretion onto a stellar-mass BH. Unlike the traditional thin disk model, which assumes a geometrically thin and optically thick structure, the puffy disk consists of a vertically extended and optically thick layer surrounding a geometrically thin core. The puffy disk is stabilized by the magnetic pressure against the thermal and viscous instabilities, even in the radiation pressure-dominated regime. The puffy disk simulations provide a detailed model of the dynamics, radiation properties, and stability of sub-Eddington accretion in XRBs by employing advanced numerical techniques and radiative transfer methods.

Simulation of the sub-Eddington accretion helps to interpret the data obtained from observations of accretion systems, such as microquasars containing a BH. By comparing the simulated observational signatures of the puffy disk with the actual astrophysical data, we can refine our models and gain insights into the physical processes occurring within these systems. Additionally, commonly used tools and methods for analyzing data from observations can be tested against the puffy disk simulations (Lančová et al. 2023; Wielgus et al. 2020).

### 4.1. Simulating a sub-Eddington accretion disk

Two apparent approaches exist to initiate a simulation of sub-Eddington accretion onto a compact object, such as a BH. The first method involves setting up a thin disk by adopting existing solutions like those proposed by Novikov & Thorne (1973) with a Gaussian distribution of quantities in the vertical direction. Alternatively, one can employ the steady thin disk solution by Kluźniak & Kita (2000). Then, thread the initial state with a weak magnetic field to induce turbulence that drives the matter towards the central BH.

However, in this particular setup, in the regime when the radiation pressure dominates over the gas pressure (e.g., for  $\dot{m} \gtrsim 0.1$  for a stellar-mass BH), the

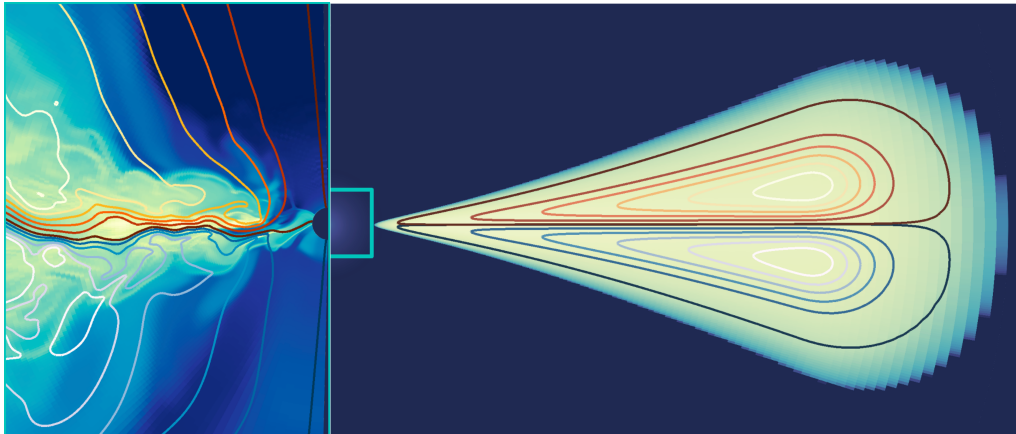


**Figure 4.1.** Logarithmic density plots of the initial torus with magnetic field loops (*right*) and the initial state for the puffy disk simulation (*left*) in the inner regions denoted by the green rectangle. The magnetic field lines are shown in both parts.

thermal and viscous instabilities lead to the collapse of the disk (Fragile et al. 2018; Jiang et al. 2013; Lightman & Eardley 1974; Shakura & Sunyaev 1976).

An effective strategy to maintain a stable sub-Eddington disk involves introducing an ad hoc cooling function as an additional source term in the MHD equations (3.36). This function removes excess or injects sparse energy generated within the flow during each time step, thereby regulating the disk's thickness to radius ratio  $H/r$  (e.g. Penna et al. 2013c; Shafee et al. 2008). However, while this approach can enforce stability, it is obviously artificial and does not fully address the underlying issue of disk stability.

On the other hand, accurately resolving the MRI in the central region of an extremely thin disk with a very low  $\dot{m}$  presents its own challenges. Achieving this requires an exceptionally high resolution throughout the entire simulation domain or implementing methods that dynamically increase resolution where needed. One such approach is the adaptive mesh refinement, as employed in simulations of tilted accretion disks by Liska et al. (2019). This method allows for targeted refinement of regions of interest, enabling a more precise representation of the MRI and its effects in razor-thin disk cores.

Another approach to simulate sub-Eddington accretion involves modelling the behaviour of matter falling onto a BH from a distant reservoir on a Keplerian orbit. However, such simulations can have excessively long duration due to their dependency on the position of the external source of matter. As a result, simulating the entire system of a BH and a star as a matter source, resembling a real XRB, becomes unfeasible within the GRMHD framework.



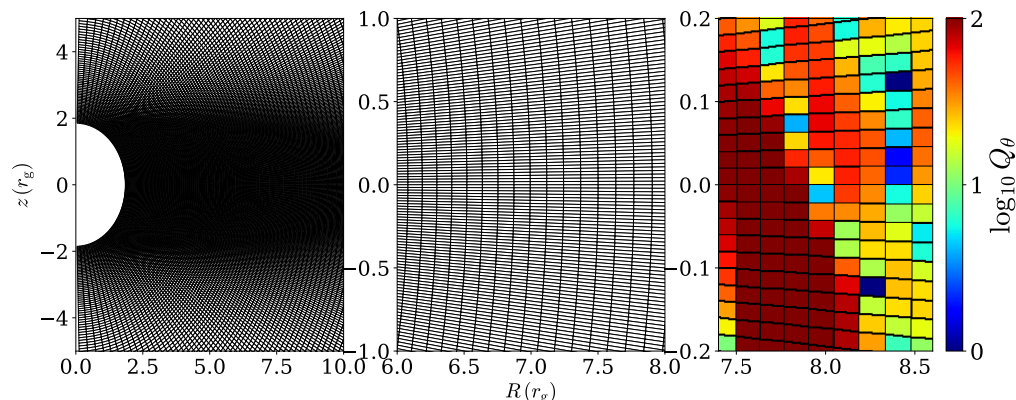


**Figure 4.2.** Computational grid for the puffy disk simulations in the  $r, \theta$  plane. *Left and middle:* Detailed view of the computational grid. *Right:* The quality parameter in the  $\theta$  direction,  $Q_\theta$ .

An alternative approach is considering a stable matter reservoir closer to the central object with on a Keplerian orbit. Then, a more manageable and realistic scenario can be obtained by focusing the analysis solely on the innermost regions where the disk is self-consistently formed.

This approach was adopted in [Sądowski \(2016\)](#), focused on the disk stability and comparison of different magnetic field topologies. In the puffy disks project, we used the same set of simulations, expanding them to lower  $\dot{m}$ , and conducted a comprehensive analysis of the disk's general properties in relation to standard analytical models.

Consequently, while the results described the disk as a "thin disk" in [Sądowski \(2016\)](#), our findings in [Lančová et al. \(2019\)](#) revealed significant differences when compared to the analytical models, leading to the introduction of a novel accretion disk model, the puffy disk.

## 4.2. Initial configuration for the Puffy disk simulations

The puffy disk simulations were initiated using a thick accretion torus of [Penna et al. \(2013a\)](#), as illustrated in the right panel of Figure 4.1. The inner edge of the torus is positioned at  $r_{in} = 42 r_g$ . The torus is threaded by a quadrupole magnetic field, with the counterclockwise loops above and clockwise loops below the equator. Initially, the magnetic field strength is set not to exceed  $\beta = p_{gas}/p_{mag} = 20$ .

The simulation is carried out in 2D for approximately  $\sim 60000 t_g$  using the mean-field dynamo (see section 3.1.4) to sustain the MRI in axisymmetric sim-

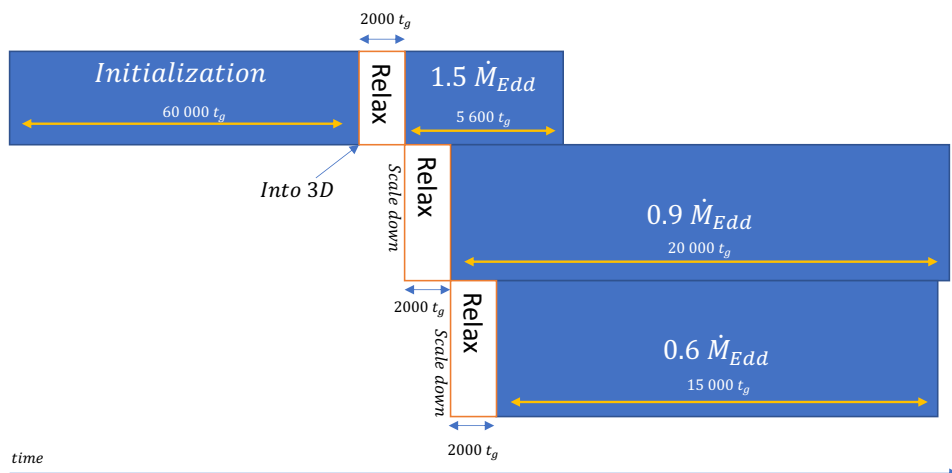


**Figure 4.3.** The timeline of the puffy disk simulations showing the initial state in 2D and the time needed for the solution to relax.

ulation. This duration allows sufficient time for the matter to form a disk in the inner region (left panel of Figure 4.1). Once the  $\dot{m}$  stabilizes, the data is extended into a 3D grid, and the simulation continues for  $\sim 2000 t_g$  to achieve a relaxed solution. This final state is considered the actual initial state of the simulations.

The first run, labelled as S15, is conducted with a super-Eddington  $\dot{m}$  but is relatively short. To obtain a lower  $\dot{m}$ , the density and magnetic field strength are scaled down by a small constant factor in the whole domain, conserving the gas temperature and maintaining a constant magnetic-to-gas pressure ratio. This rescaled simulation is run for an extended period and results in  $\dot{m}$  dropping to  $\sim 0.9$ . Following another rescaling, the  $\dot{m}$  decreases further to  $\sim 0.6$ , leading to the puffy disk as described in Lančová et al. (2019) (simulation S06).

Attempting another rescaling with the original resolution becomes problematic, as the inner region close to the equatorial plane becomes unresolved, leading to the rapid collapse of the disk. Table 4.1 provides an overview of all three simulations and selected parameters, and Figure 4.3 the timeline of the simulations.

#### 4.2.1. Computational grid and resolution

The computation grid resolution is  $(320, 320, 32)$  in  $N_r, N_\theta$ , and  $N_\phi$  respectively. In the  $\phi$  direction, the domain covers a  $\pi/2$  wedge rather than the full  $2\pi$  to optimize computational resources. For verification, a full 3D simulation was presented in Sądowski (2016), demonstrating that the results quantitatively match those obtained from the  $\pi/2$ -wedge simulation.

**Table 4.1.** Puffy disk simulations and selected parameters, including the density scale-height  $h_\rho$ , photosphere height  $h_\tau$  to radius ratio, total duration  $T_{run}$  of each simulation in  $t_g$ , number of orbits at  $r = 10r_g$ , and seconds.

Simulation	$\dot{m}$	$h_\rho/r$	$h_\tau/r$	$T_{run}(t_g)$	$T_{run}(\text{orbits})$	$T_{run}(\text{s})$
S15	1.51	0.20	1.0	5600	28	0.27
S09	0.89	0.15	1.0	20000	100	0.98
S06	0.58	0.10	1.0	17400	87	0.86

The calculations are performed on the MKS coordinates, employing logarithmic spacing in  $r$  and  $\theta$ , concentrating cells in the innermost regions, achieving a significant effective resolution. The computational grid can resolve the MRI even in the dense disk core while satisfying the minimal requirements for the quality parameters throughout the disk, see Figure 4.2.

#### 4.2.2. Stability

In the analytical thin disk model, the balance between the viscous heating  $Q_{\text{visc}}^+$  and radiative cooling  $Q_{\text{rad}}^-$  is maintained when the disk is primarily governed by gas pressure. However, when the radiation pressure exceeds the gas pressure, this balance is swiftly disrupted, resulting in disk collapse. This phenomenon was also demonstrated in GRMHD simulations, such as those conducted by Mishra et al. (2016).

In order to study the stability of an accretion disk, an ideal simulation would need to span a duration corresponding to the viscous timescale at the outer edge of the disk, which is approximately  $t_{\text{acc}} \sim 10^{17} t_g$  ( $10^{13}$  s for  $10M_\odot$  BH), for the outer edge located at  $100r_g$ . However, within the framework of GRMHD, the longest simulations have only recently reached a duration of up to  $10^5 t_g$  (Liska et al. 2019). Conducting a radiative simulation of such an extended duration would require immense computational power. Nonetheless, the stability can still be investigated in shorter simulations, e.g., by examining if the simulation remains stationary on the  $T - \Sigma$  diagram, where  $\Sigma$  is the surface density. The balance in the azimuthal ( $\phi$ ) direction can be demonstrated through the radial profile of  $\dot{m}$ , which should remain constant if the mass inflow is stable.

In the puffy disk simulation, the heating and cooling processes are balanced throughout the entire duration, thanks to the vertical net flux of the magnetic field, as is illustrated in Figure 4 of Sądowski (2016). Figure 4.5 shows that the puffy disk maintains thermal equilibrium throughout the simulation. Addition-

ally, Figure 4.6 indicates that the total  $\dot{m}$  remains stable up to relatively large radii, providing further evidence of a relaxed and stable simulation.

### 4.3. Properties of the puffy disk

The puffy disk represents a sub-Eddington accretion disk stabilized by magnetic pressure. The disk is geometrically and optically thick. It can be divided into three distinct regions, each with unique properties:

- Core (C on Figure 4.4): This region resembles a standard thin disk, geometrically thin and dense.
- Puffy region (P on Figure 4.4): A vertically extended optically thick area of hot magnetized gas. It resembles a warm corona, as discussed in Gronkiewicz & Różańska (2020) and Różańska et al. (2015).
- Funnel (F on Figure 4.4): Located above the disk, this optically thin region exhibits strong outflows.

The disk core is defined by the density scale height given by

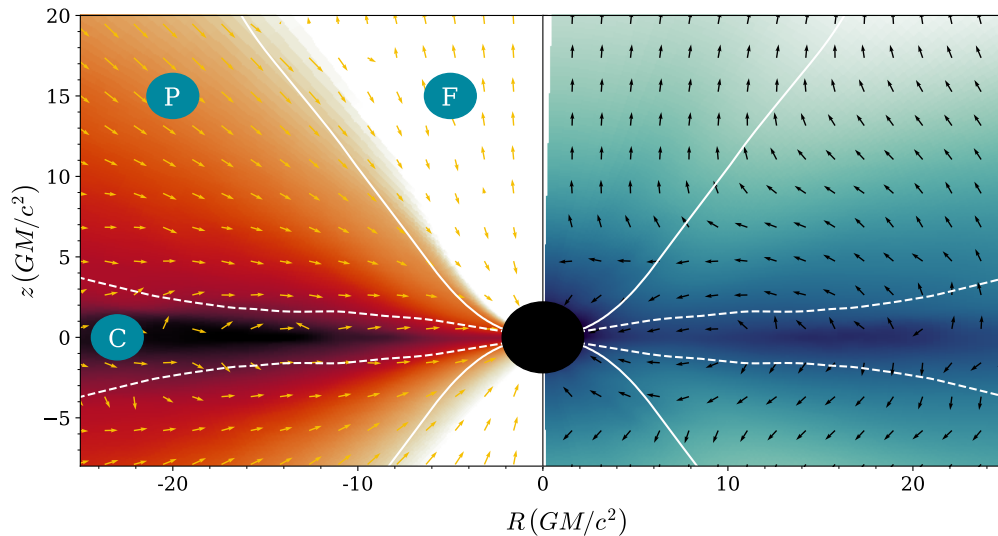


**Figure 4.4.** The structure of the puffy disk: Gas and radiation in the  $r - \theta$  plane using the time-averaged data from S06. The full white line represents the photosphere, while the dashed line indicates the density scale height. *Left:* Logarithm of density with denoted regions (C - core, P - puffy, F - funnel). Quivers show the gas momentum flux. *Right:* Logarithmic colour map displaying radiation energy density, accompanied by arrows indicating the radiation flux.

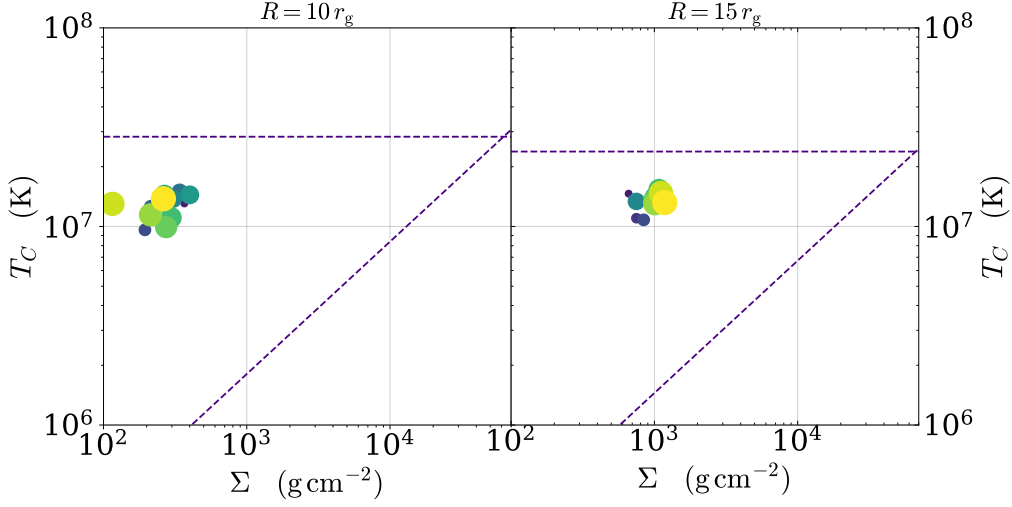


**Figure 4.5.** Thermal equilibrium ( $T - \Sigma$ ) diagram for a standard thin disk at  $r = 10 r_g$  (left) and  $r = 15 r_g$  (right), using  $\alpha = 0.1$ ,  $m = 10$  and non-rotating BH. The dots represent the time evolution of the puffy disk during the S06; the colour of the dots changes from blue to yellow, and their size grows over time.

$$h_\rho = \sqrt{\frac{\int \rho z^2 dz}{\int \rho dz}}. \quad (4.1)$$

The photosphere of the disk is located where the gas becomes optically thin, corresponding to a surface denoted by  $h_\tau$ . The criterion for optically thin gas is when the vertically integrated optical depth,  $\tau$ , satisfies  $\tau \leq 2/3$ . The optical depth is calculated as

$$\tau(z) = \int_{z_{\text{out}}}^z \kappa_{es} \rho dz. \quad (4.2)$$

where the integration is performed from the outer boundary at  $z_{\text{out}}$  towards the equator.

The core resembles a geometrically thin Keplerian disk of high density, gas temperatures around  $10^7$  K, and subsonic accretion velocities. The mass accretion rate in this region is very low, and it even approaches zero in some areas (as shown in Figure 4.6). Most of the accretion occurs in the puffy region, particularly at larger radii.

The fluid within the disk shows a high level of magnetization, particularly in the funnel region, but is also higher in the puffy region than in the core. The

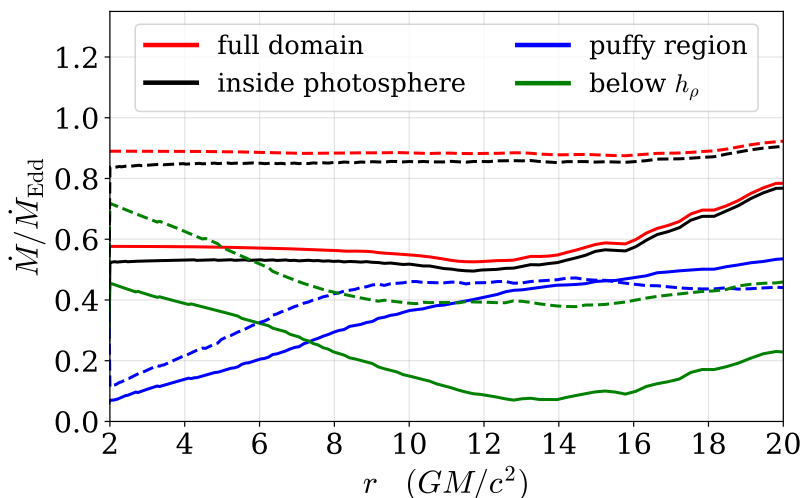


**Figure 4.6.** Mass accretion rate  $\dot{m}$  in different regions for all three runs. Dashed lines correspond to S09, while the solid lines to the S06.

magnetic field is turbulent in the disk; however, these turbulent fluctuations are averaged out over the entire simulation run to establish a magnetic field topology specific to this solution. In this topology, the azimuthal component dominates within the disk, while the radial component dominates in the funnel region, as shown in Figure 4.7.

On the photosphere, the magnetic field rapidly changes as the field lines are carried away by the gas. This process leads to a decrease in the magnetic pressure and potential formation of a current sheet and magnetic reconnection, which cannot be resolved in our simulations under the ideal MHD approximation.

In the optically thick regions of the puffy disk, the radiation approximately follows the density gradient, escaping through the funnel region and becoming collimated along the axis. In the innermost regions of the disk, a significant portion of the radiation is advected into the BH, contrary to what analytical models predict. A fraction of the radiation is also released, but closer to the centre than anticipated in a standard thin disk. As a result, the spectrum is shifted towards lower radii compared to the predictions of a standard thin disk model.

Regarding the gas dynamics, a strong inflow is present in the puffy region of the disk. On the other hand, the gas motion in the core region of the disk is slower and more turbulent. This behaviour arises from the complex interplay between magnetic forces, radiation pressure, and gravitational effects within the disk. The slower and more turbulent motion in the core allows for energy dissipation and redistribution of angular momentum, leading to the formation and maintenance

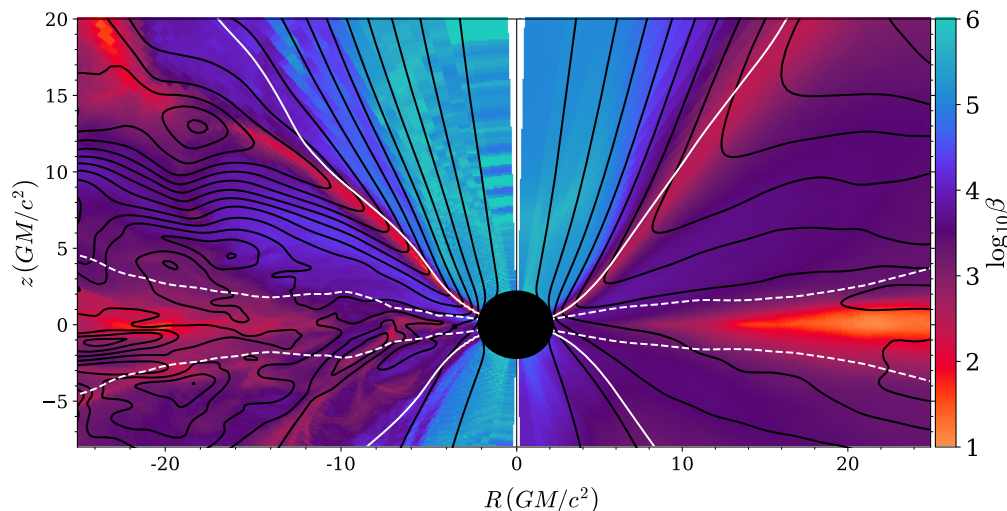


**Figure 4.7.** Magnetic field lines (black contours) and magnetization  $\beta$  shown in colours for simulation S06. The white solid line represents the photosphere, while the dashed lines indicate the density scale height. The *right* panel displays data averaged over both azimuthal angle and time, providing an overall view. In contrast, the *left* panel shows a snapshot from the simulation, averaged only over the azimuthal angle (close to the axis, the snapshot data shows numerical error due to lower resolution, these errors are being corrected during the simulation run and do not impact the overall results.).

of the geometrically thin disk structure observed there.

The core temperature is slightly higher than the puffy region, as illustrated in Figure 4.9. The core temperature rapidly increases in the plunging region, but the temperature on the photosphere follows almost a power-law distribution with no significant change under the  $r_{\text{ISCO}}$ .

In both the core and puffy regions of the disk, the radiation and magnetic pressures surpass the gas pressure by several orders of magnitude, as shown in Figure 4.8. The presence of magnetic pressure and its interplay with other physical processes contribute to the stability of the disk, despite the significant deviation from the traditional expectations of a sub-Eddington thin disk structure.

#### 4.4. Observational picture

The analysis of these observational properties of the puffy disk and comparisons with analytical models were presented in [Wielgus et al. \(2022\)](#), and in [Lančová](#)

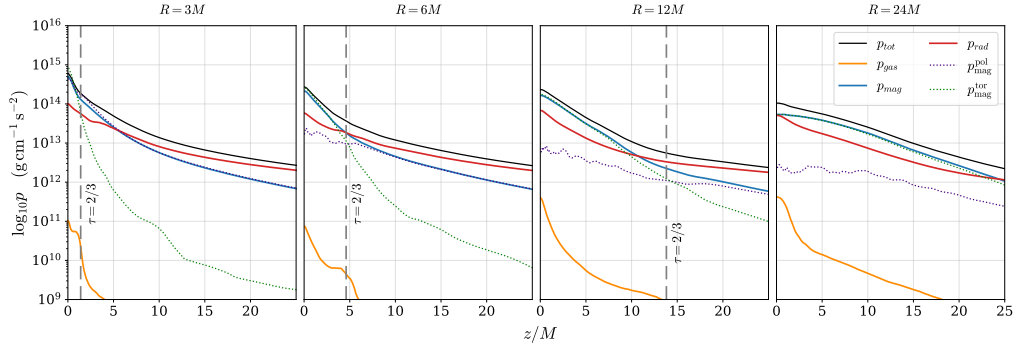


**Figure 4.8.** Vertical distribution on pressure components on selected radii for the S06 simulation.

et al. (2023) it was extended to include also the kynbb spectral model in XSPEC and compare it with the kerrbb.

The puffy disk spectra and images were computed using the relativistic radiative post-processing code HEROIC (Narayan et al. 2016; Zhu et al. 2015). This code solves the complete radiative transfer problem on the time-averaged output from the converged simulations for three different mass-accretion rates. By accounting for various physical processes such as scattering effects, Comptonization, bremsstrahlung, and synchrotron radiation, HEROIC enables to study of observational properties and a direct comparison with standard analytical models. Additionally, it provides an opportunity to validate commonly used tools by simulating observations.

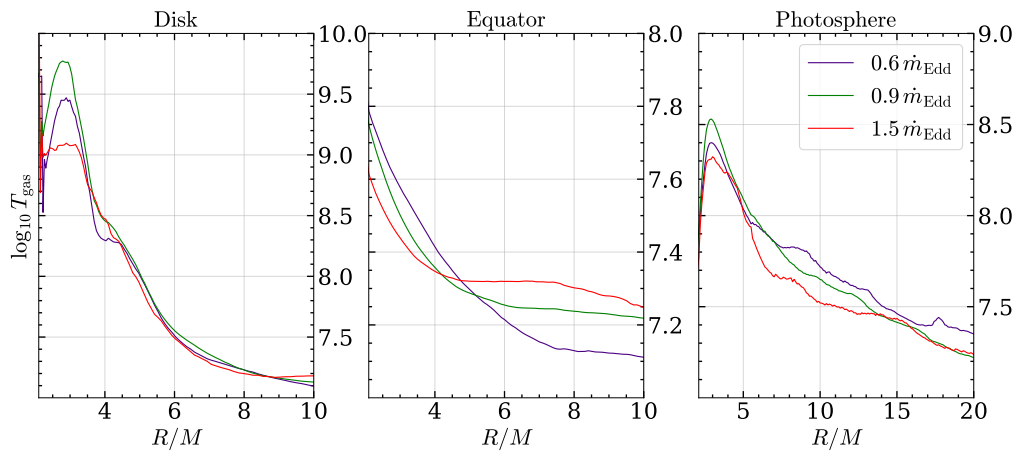


**Figure 4.9.** Radial profiles of the gas temperatures for all three simulations on different surfaces, at the core surface (left), at the equator (middle), and on the photosphere (right).



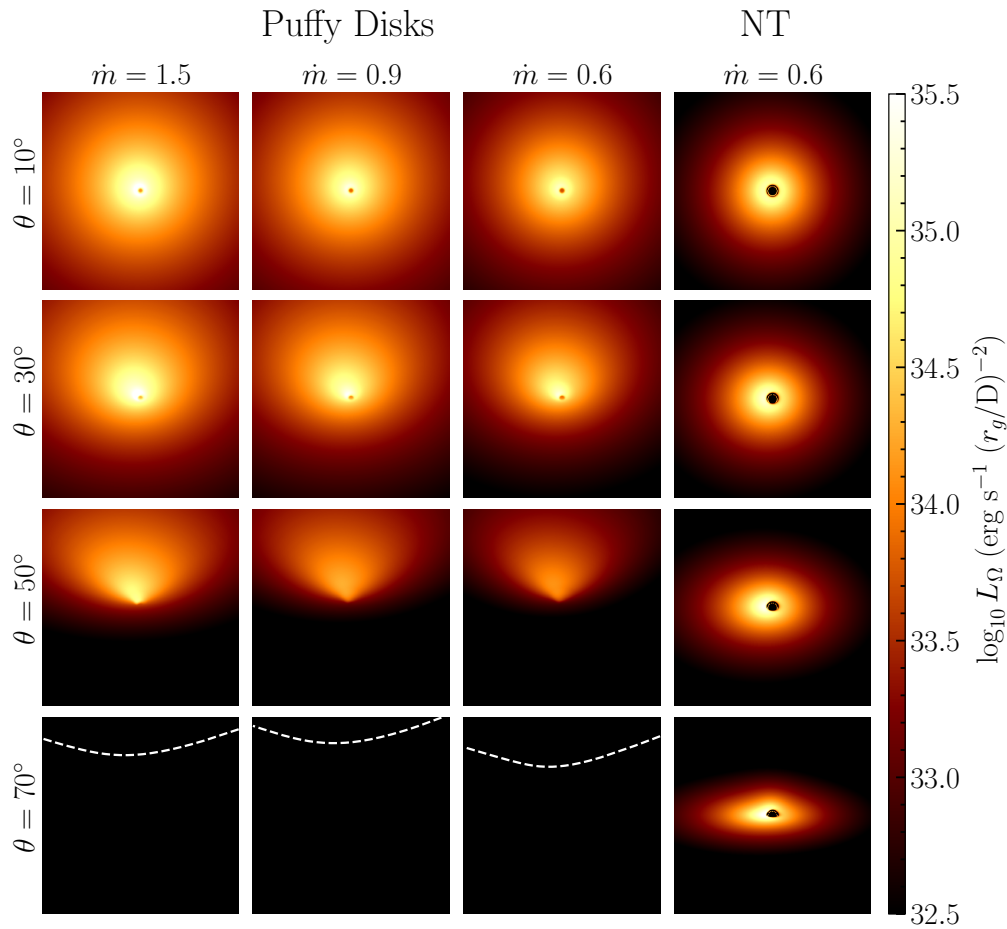


**Figure 4.10.** Three columns on the left show the images of the puffy disk for three different mass-accretion rates, while the right column is the image of a standard thin disk with  $\dot{m} = 0.6$ . The images are arranged in increasing inclination angles from top to bottom. The colour map scale is consistent across all images. However, in the last row, the puffy disk’s luminosity is significantly lower, making its visibility less prominent than the other images. From [Wielgus et al. \(2022\)](#)

One feature of the puffy disk is the beaming of radiation towards the rotational axis, accompanied by significant obscuration for viewing angles close to the equatorial plane. This behaviour stands in contrast to the standard thin disk model. The inner parts of the disk and the central BH are completely obscured for observers with high inclinations, see [Figure 4.10](#). Conversely, for observers with low inclinations, the disk radiation extends all the way to the event horizon.

The shape of the spectra emitted from the puffy disk is similar to analytical thin or slim disk models, with a notable additional power-law component corresponding to thermal Comptonization. However, when comparing the spectra

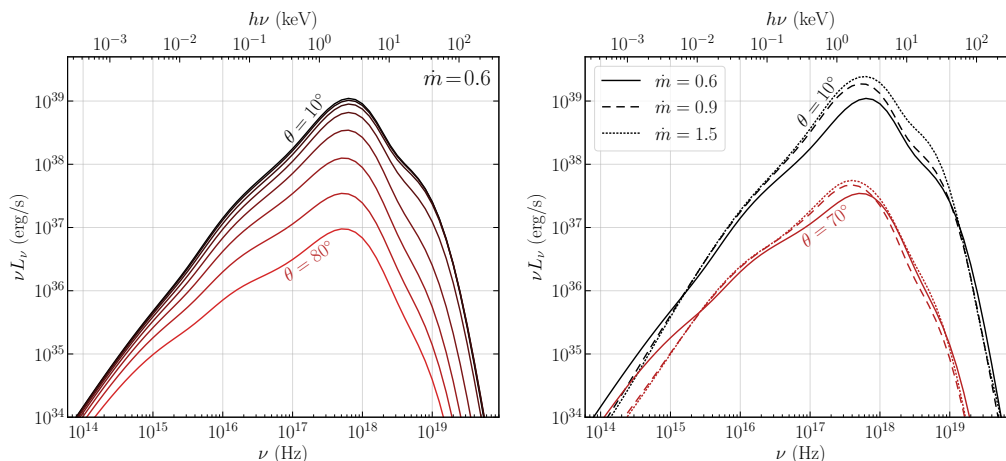


**Figure 4.11.** *Left:* isotropic radiative power per logarithmic frequency interval, as a function of the observer’s inclination, from  $10^\circ$  (nearly face-on) to  $80^\circ$  (nearly edge-on). *Right:* isotropic radiative power per logarithmic frequency interval for three puffy disks simulations, corresponding to different mass accretion rates.

from the three simulation runs at different inclination angles, deviations from the analytical models become larger. While the observer’s inclination angle can influence the position of the maximum of luminosity by up to two orders of magnitude, fixing the inclination angle shows no significant change in the SED for different  $\dot{m}$  values, as shown in Figure 4.11. Regardless of the inclination angle, the frequency of photons associated with the peak luminosity remains constant.

Synthetic spectra of the puffy disk were generated for two inclinations of the S06 simulation to test the performance of commonly used spectral fitting models. These spectra were then fitted using the XSPEC package (Arnaud 1996), simulating the observation of a real astrophysical source. Two models, a fully relativistic thin disk model (kerrbb, Li et al. 2005a) and a fully relativistic advective slim disk model (slimbb, Sądowski 2009; Straub et al. 2011), were used, each accompanied by a thermal Comptonization component (nthcomp, Zdziarski et al. 1996; Życki et al. 1999), which models seed photons from the disk that are upscattered to higher energies by a homogeneous corona. The same analysis was later repeated for the kynbb (Dovčiak et al. 2004) model.

The BH mass, distance, viscous  $\alpha$ , and inclination angle were fixed for the fitting, and total luminosity, spin, temperature of the seed and up-scattered photons, and photon index are free parameters. The results showed that the puffy disk could be fitted with standard tools and provide a reasonable set of parameters.

However, the results of the fitting process did not align with the simula-

---

tion parameters. Notably, the BH spin is overestimated, with obtained values of  $a \sim 0.8$  for low inclination and  $a \sim 0.5$  for high inclination angles. This discrepancy highlights the problems of fitting spectral states with strong Comptonization, leading to unreliable spin measurements using continuum fitting methods (Gierliński & Done 2004).

The puffy disk simulation (S06) can be compared to the ultra-luminous or intermediate state of a microquasar during an outburst, characterized by high luminosity and a soft spectrum with a prominent Compton component. In this state, QPOs are often observed. However, due to the limitations of the simulation duration and the capabilities of the radiative transfer code, a detailed analysis of the oscillatory behaviour and fast variability is not feasible within the scope of this model.



## Chapter 5

# Modelling the rapid time variability of XRBs

Observations of bright objects in the X-ray sky reveal distinct properties of these sources, such as the quasi-periodic temporal variability across a wide range of frequencies, as described in Section 1.3.2. Since the discovery of the QPOs in the late 1980s (Middleditch & Priedhorsky 1986), they have been brought to the attention of many research groups and have been the target of observations by X-ray telescopes (Remillard & McClintock 2006; Van der Klis 2006). With the launch of the Rossi X-Ray Timing Explorer (RXTE) in 1995, high-frequency variability was discovered (Bradt et al. 1993; Wijnands 1999).

Initially observed in NS sources, where the HF QPOs are very strong, they were also identified in BH sources. This chapter is dedicated to modelling the HF QPOs and their application in extracting information about the geometry and properties of the central object in these sources.

The frequencies of HF QPOs are apparently linked to the fundamental frequencies of motion in the innermost regions of accretion disks (Karas 1999a,b; Stella & Vietri 1999; Török et al. 2005). However, accurately modelling the origin of these oscillations is a complex task that requires long-time GR simulations of the behaviour of matter and radiation in the close vicinity of a compact object.

This chapter describes HF QPO modelling, as presented in the following published papers. Despite the strong correlation between LF QPOs frequencies and those of the HF QPOs, the latter is more complicated to model and explain. In fact, up until now, no widely accepted model comprehensively explains these phenomena. For convenience, the HF QPOs are henceforth referred to as QPOs.

I have contributed to several published results in this field throughout my studies, complementing those described in the previous chapters. Additionally, I have actively participated in several ongoing studies, that have already been published or are currently submitted for peer review.

## 5.1. Fast time variability of black holes and neutron stars in XRBs

Over the years following their discovery, several models have been proposed to explain the QPOs. These models are founded on the premise that the QPOs originate in the innermost regions of an accretion disk near the central compact object. While each model can explain specific observed properties, they often have limitations when addressing other aspects. Furthermore, it remains to be seen whether the mechanism behind the twin-peak QPOs in NS systems is the same as that governing the QPOs in BH systems (Van der Klis 2006).

In the case of NS sources, the observed variability is often tied to processes occurring on its surface and interactions between the disk, the star, and a luminous boundary (spreading) layer on the NS surface. As discussed in Section 1.3.2, NS systems display LF QPOs corresponding to the horizontal, normal,

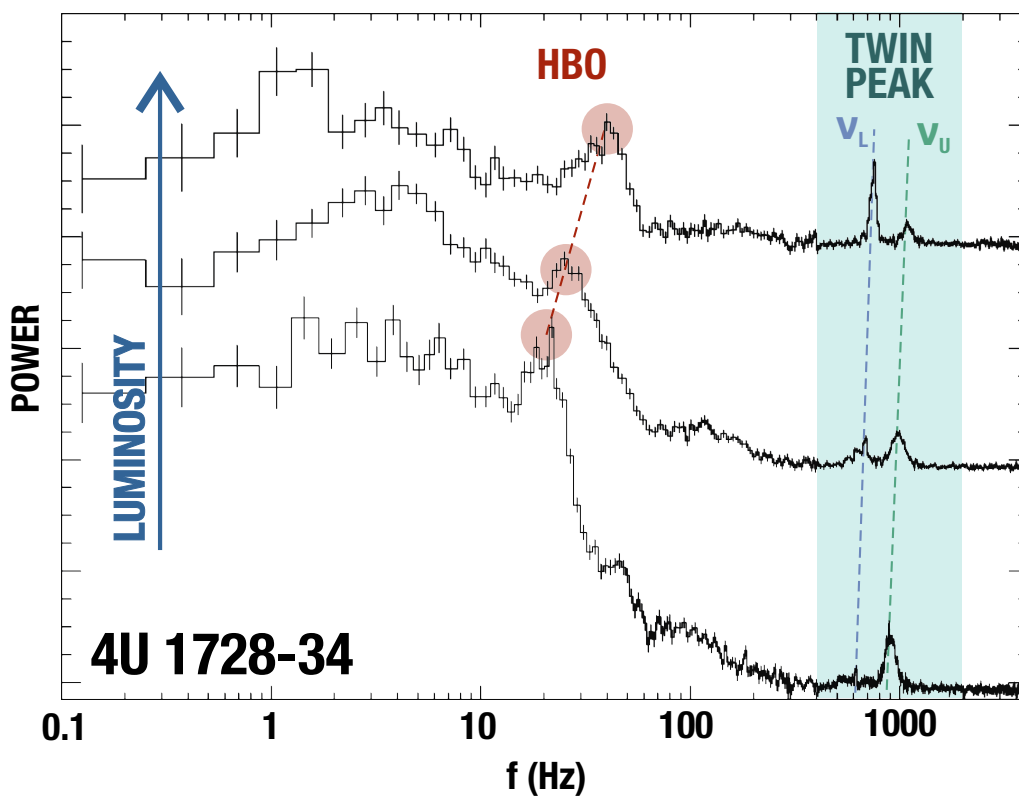


**Figure 5.1.** PSD diagram from three observations of NS LMXB 4U 1728-34, each corresponding to an increase in luminosity. Both the LF QPOs and thin-peak QPOs are clearly visible, along with changes in the significance of the lower  $\nu_L$  and upper  $\nu_U$  peak. Data from Strohmayer et al. (1996).

and flaring branches on the HID, as well as the twin-peak QPOs (sometimes referred to as kHz QPOs) with very high frequencies comparable to the orbital frequencies in the innermost regions.

An interesting observation is the strong correlation between the HBO frequency and the lower peak of the twin peak QPOs (Van der Klis 2006), shown in Figure 5.1. This correlation was explained as a superposition of the Keplerian frequency at the inner edge of an accretion disk (associated with the magnetospheric radius in NS systems) and the rotational frequency of the NS itself. This model is known as the magnetospheric-beat frequency model (Alpar & Shaham 1985; Miller et al. 1998).

However, this scenario is limited to specific QPO observations and a narrow range of NS's surface magnetic field strengths. Eventually, with more twin-peak QPO data being observed, a decrease in frequency difference with increasing frequency was discovered, contradicting this model.

Another phenomenon often categorized as QPOs is the NS burst oscillations observed during type I X-ray bursts. These bursts occur due to the sudden ignition of thermonuclear burning of accreted material on the NS surface. The frequency of burst oscillations falls within the range of 300 to 600 Hz, which is close to a typical NS spin frequency. However, frequency shifts during the burst have been observed (see, for example, Strohmayer et al. 1997), consistent with a small expansion of the NS envelope. Models involving unstable inhomogeneous hydrogen burning on the NS surface and non-radial oscillation modes of the envelope have been proposed, providing a reasonably accurate representation of the observed data (Bildsten & Cumming 1998).

## 5.2. Foundations of the orbital models of QPOs

QPOs are observed in both NS and BH systems. However, in NS systems, the amplitude of the oscillations is much higher compared to the BH systems, see Figure 1.9. The observed frequencies of these oscillations closely align with the fundamental frequencies of orbital motion in the vicinity of a compact object. This alignment is particularly evident for geodesic circular motion with Keplerian orbital frequency

$$f_K = \frac{c^3}{2\pi GM} \frac{1}{a + r^{3/2}}, \quad (5.1)$$

and the radial  $f_r$  and vertical  $f_\theta$  epicyclic frequencies

$$f_r^2 = f_K^2 \left[ \left( 1 - \frac{6r_g}{r} \right) + 8a \left( \frac{r_g}{r} \right)^{3/2} - 3a^2 \left( \frac{r_g}{r} \right)^2 \right], \quad (5.2)$$

$$f_\theta^2 = f_K^2 \left[ 1 - 4a \left( \frac{r_g}{r} \right)^{3/2} + 3a^2 \left( \frac{r_g}{r} \right)^2 \right] \quad (5.3)$$

in the Kerr metric, where  $a$  is the non-dimensional spin parameter of the central object and  $r$  is the radius. The radial dependence of these frequencies and their typical values for a stellar-mass BH and a NS are illustrated in Figure 5.2.

Quasi-periodic modulation in the X-ray band, with frequencies similar to those of the orbital motion, has been observed not only in XRBs but also in galactic centres containing a super-massive BH (Carpano & Jin 2018). Observations across a wide range of masses demonstrated that the observed QPOs are inversely proportional to the mass of the central object and fall within the range defined by the Keplerian frequency in the innermost regions (Abramowicz et al. 2004; Goluchová et al. 2019; Karas et al. 2023; Remillard & McClintock 2006).

### 5.2.1. Models of orbiting blobs

Various mechanisms implemented within distinct QPO models can translate the orbital motion into the observable signal. One such mechanism involves the motion of clumps or blobs of matter in the innermost region of accretion disks.

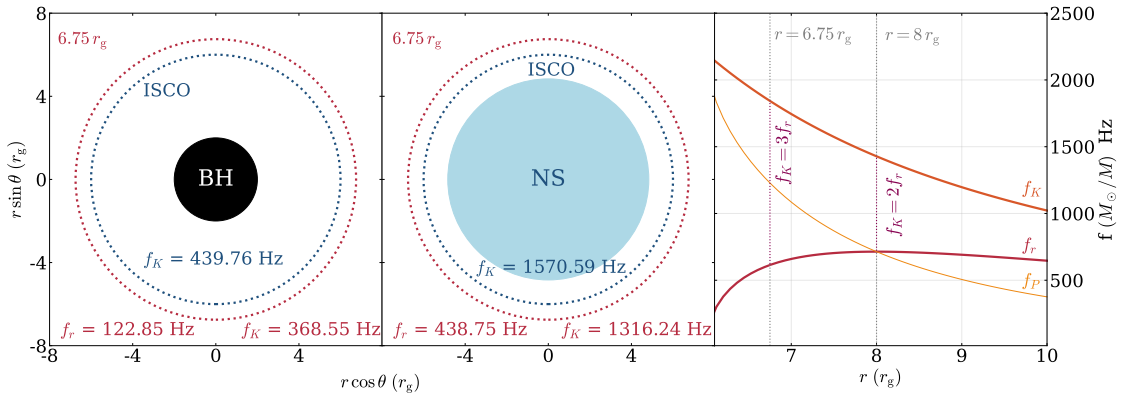


**Figure 5.2.** *Left and Middle:* Illustration of a non-rotating BH and NS, accompanied by the corresponding values of Keplerian ( $f_K$ ) and radial epicyclic ( $f_r$ ) frequencies at  $r_{\text{ISCO}}$  and  $r = 6.75 r_g$ , where  $f_K = 3f_r$ . Values for the BH are calculated for  $M = 5 M_\odot$ , while those for the NS for  $M = 1.4 M_\odot$  and radius  $R_* = 10$  km. *Right:* Values of the  $f_K$ ,  $f_r$  and  $f_P$  in the Schwarzschild case. Note that in the non-rotating spacetime  $f_\theta = f_K$ .



These clumps, having higher temperature than the surrounding disk, can modulate the observed light curves as they orbit. This concept was recognized prior to the first QPO observations and was considered a potential method to measure the NS mass (Kluźniak et al. 1990).

A specific model based on the kinematics of orbital motion in proximity to a compact object is the relativistic precession (RP) model. This model explains the oscillations by considering the geodesic motion of a test particle within the framework of GR (Stella & Vietri 1999). The RP model connects the frequency of the upper peak of QPOs to the Keplerian frequency ( $\nu_U = f_K$ ), while the lower peak corresponds to the periastron precession frequency ( $\nu_L = f_P = f_K - f_r$ ), as illustrated in the right panel of Figure 5.2. Additionally, the model interprets the LF QPOs as the nodal precession frequency. However, the coherence times observed in the QPO signals contradict the predictions of the RP model (Barret et al. 2005).

### 5.2.2. Diskoseismology

The distinct profile of the radial epicyclic frequency motivated the development of a family of diskoseismic models. The presence of a maximum in  $f_r$  relatively close to the  $r_{\text{ISCO}}$  can lead to the trapping of oscillatory modes, particularly the g-mode, within an accretion disk. This trapping can yield observational signatures (Nowak & Wagoner 1991, 1992).

One of these models is the disk warp model, where the oscillations are generated by perturbing an initially axisymmetric state of the disk, leading to the trapping of specific modes (Kato 2004). These modes have also been observed in (GR)MHD simulations (Bollimpalli et al. 2020; Dewberry et al. 2020; Kato & Machida 2020; Mishra et al. 2019, 2020).

### 5.2.3. Oscillations of accretion tori

An extensive collection of papers has been published, proposing a connection between the QPOs and oscillations of accretion tori, (e.g., Abramowicz et al. 2006; Abramowicz & Kluźniak 2001; Blaes et al. 2006; Bursa 2005; Bursa et al. 2004; de Avellar et al. 2017; Fragile et al. 2016; Ingram & Done 2010; Mishra et al. 2017; Rezzolla et al. 2003).

The accretion tori are often approximated using the Polish doughnut model, which assumes a stationary perfect fluid in purely azimuthal motion. It forms within the surfaces of constant potential, in which the gravitational forces acting on the torus and the internal pressures of the torus are combined (Abramowicz

et al. 1978; Jaroszyński et al. 1980). Although the Polish doughnut model is known to be unstable to the Papaloizou–Pringle instability (Papaloizou & Pringle 1984), it, in general, provides a good approximation for a time-averaged realistic turbulent accretion flow.

The specific frequency ratios of QPOs observed in both BH and NS sources have inspired the development of the family of resonance models (Abramowicz & Kluźniak 2001; Kluźniak & Abramowicz 2001). These models connect the QPO to oscillations at distinct radii, where the ratios of Keplerian and epicyclic frequencies are small natural numbers. In the simplest case of the Schwarzschild metric, these radii are  $r = 6.75 r_g$ , where  $f_K = 3f_r$ , or  $r = 8 r_g$ , where  $f_K = 2f_r$  (which also corresponds to the maximum of the radial epicyclic frequency, Kato & Fukue 1980).

Oscillations of fluid accretion tori situated very close to the central compact object have been explored within the resonance models, (Abramowicz & Kluźniak 2004; Kluźniak et al. 2004; Lee et al. 2004). In this case, the two QPO peaks are associated with the fastest-growing resonant modes in the accretion disk, which correspond to the 3:2 epicyclic frequency ratio (Kluźniak & Abramowicz 2002; Rezzolla et al. 2003).

Possible resonances between frequencies of relativistic orbital motion were extensively studied in a large collection of papers (Abramowicz & Kluźniak 2001; Bakala et al. 2015a; Horák et al. 2004, 2009; Horák & Karas 2006; Horák & Lai 2013; Kluźniak 2008; Kluźniak & Abramowicz 2001; Méndez & Belloni 2021; Pétri 2005; Stuchlík et al. 2013). Currently, the role of resonances in the generation of QPOs is subject to debate (Abramowicz et al. 2003; Boutelier et al. 2010; Ingram & Motta 2019; Török et al. 2008). However, the concept of oscillating accretion tori persists as a robust and plausible explanation for this phenomenon.

### 5.3. Marginally overflowing tori and the CT model

A thick accretion torus can be described using the Polish doughnut model recalled in Sections 2.5 and 5.2. A torus can fit within any of the equipotential surfaces defined by the model, spanning from an infinitesimally slender torus with an elliptic cross-section (circular in Newtonian gravity or the Schwarzschild case) to a maximally thick torus that fills the critical largest closed equipotential, forming a cusp-like shape. A typical shape of the equipotential surfaces is illustrated in the left panel of Figure 5.3.

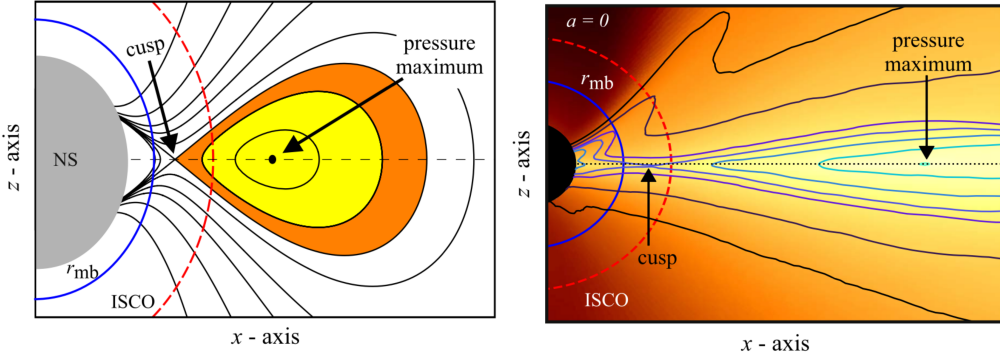


**Figure 5.3.** Comparison of the cusp torus geometry based on analytical solution of the Polish doughnut and the equipressure surface in complex GRRMHD simulation of the puffy disk. From Török et al. (2022).

The torus thickness is quantified by parameter  $\beta$ , where  $\beta = 0$  corresponds to a slender torus and  $\beta = 1$  to a theoretical torus of infinite size. The specific value of  $\beta$  for the cusp torus configuration ( $\beta = \beta_{cusp}$ ) depends on the spacetime geometry (Straub & Šrámková 2009), yet it is also constrained by the accreting system geometry, see Figure 5.4.

Analytical formulas for the radial and vertical eigenfrequencies of torus oscillations in the Paczyński-Wiita potential were derived by Blaes et al. (2007) and Šrámková et al. (2007), and a full-GR version of these formulas was introduced by Straub & Šrámková (2009) and Fragile et al. (2016) for slightly non-slender tori with a constant angular momentum.

The cusp torus configuration is promising for modelling oscillation modes in real accretion disks, as it corresponds to a marginally overflowing torus. Oscillations of such torus, situated in the innermost region of the accretion flow, can modulate the amount of matter transferred onto the NS surface, which can be reflected in the luminosity of the boundary layer (Horák 2005; Paczynski 1987). Furthermore, a cusp-shaped structure is also expected to exist in real accretion disks (Kotrlová et al. 2020; Török et al. 2022), see Figure 5.3.

The cusp-torus (CT) model, initially introduced and preliminary tested on observed data from NS sources in Török et al. (2016b), is based on the solution of Straub & Šrámková (2009). This model assumes oscillations and Keplerian motion related to cusp tori. In Kotrlová et al. (2020), the model was applied to observed QPOs in galactic microquasars and compared to other models.

More recently, the CT model has been extended into the Hartle-Thorne metric (Matuszková et al. 2022; Šrámková et al. 2023), incorporating the influence of the quadrupole moment of a NS,  $q = Q/M^3$ . This parameter significantly

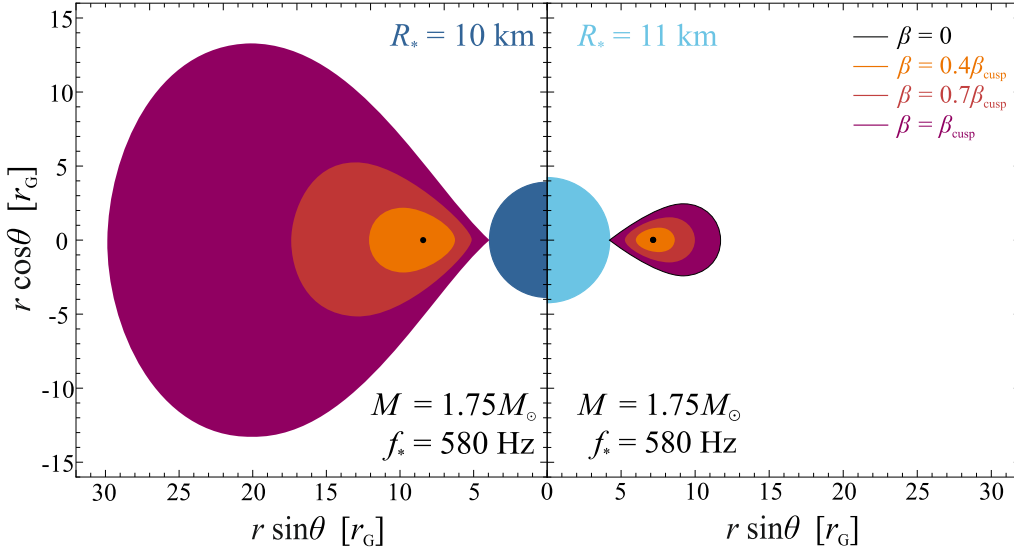


**Figure 5.4.** Theoretical maximal size of a cusp torus in the Hartle-Thorne metric limited by the radius of the NS  $R_*$  for fixed mass and rotational frequency  $f_*$ . This limitation arises from the universal relations linking the metric parameter  $q$  to the mass, spin, and radius of the NS (Urbanec et al. 2013). Based on Matuszková et al. (in preparation).

affects the frequencies of orbital motion (Urbancová et al. 2019; Urbanec et al. 2013). The Hartle-Thorne metric is accurate to the second order in  $q$  and therefore provides a sound approximation for the spacetime surrounding an oblate NS, with deviations mainly occurring close to the ISCO. It was shown that this model matches frequencies of twin-peak QPOs (Török et al. 2016a, 2022).

## 5.4. Oscillations of accretion tori and estimations of parameters of compact objects

The frequencies of observed QPOs can be used to derive parameters of the compact object, such as its mass or spin, due to their linkage to the accretion flow properties. Values deduced from such fitting can be directly compared with outcomes obtained from alternative parameter estimation methods, including those based on the spectral properties of the signal. This comparison helps to validate both the results and methodologies.

### 5.4.1. Estimation of black holes spin

Figure 5.5 presents a comparison of multiple spin estimation methods for five BH sources. The first two, LMC X1 and 4U 1543–475, are included for reference

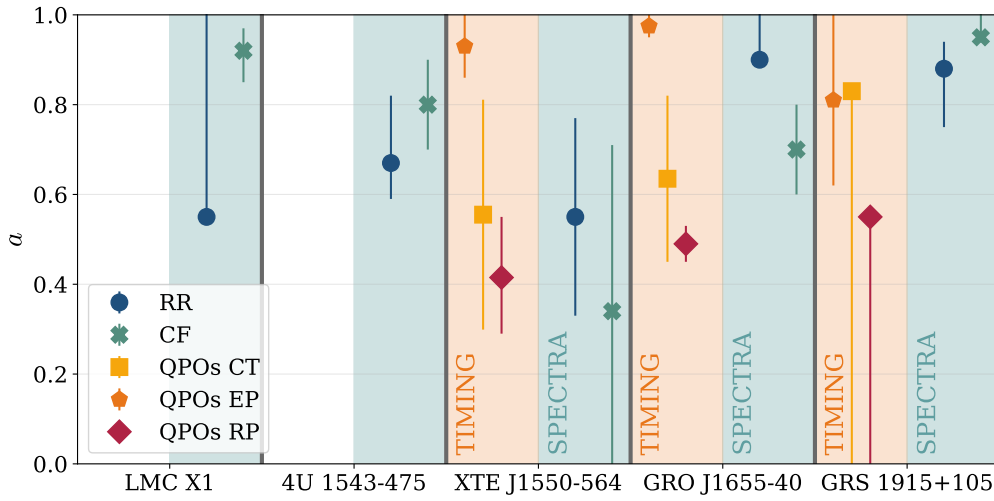


**Figure 5.5.** Comparison of spin value estimations for selected BH XRBs. The values obtained via the CF and RR methods, based on the spectral properties, are in the blue segments of the plots. Values derived through the timing-based methods are in the orange segments of the plots. The timing methods employ the CT and RP models and axisymmetric radially and vertically oscillating torus model (EP). Data for [Kotrlová et al. \(2020\)](#) and [Reynolds \(2021\)](#).

as the QPOs were not observed in them. Several methods were applied to the remaining three sources, some reproducing results within comparable limits.

The relativistic reflection (RR) method, based on the reflection of X-ray radiation from a corona on the accretion disk ([Dauser et al. 2016](#)), is one of the chosen methods. The relativistic effects broaden the typically narrow iron  $K\alpha$  line after reflection, which can reveal the size of the disk and, subsequently, the parameters of the central object. The continuous fitting (CF) method (also discussed in Chapter 2) involves fitting observed spectra with a thermal multi-black body spectrum expected from a thin accretion disk. Since the spectral shape and total flux strongly depend on the inner edge position, it can reveal important information about the system ([Zhang et al. 1997](#)).

In contrast, the timing-based methods often involves fitting the frequencies of QPOs with the fundamental frequencies of motion near a BH. A detailed description of these models and the spin estimation process can be found in [Kotrlová et al. \(2020\)](#).

Figure 5.5 shows that specific spectral and timing-based methods often yield consistent results, pointing to relatively high spin values in the BH XRBs. However, it is evident that no universally preferred method exists, and the applied methodology remains premature. Despite variation in spin estimates from X-ray

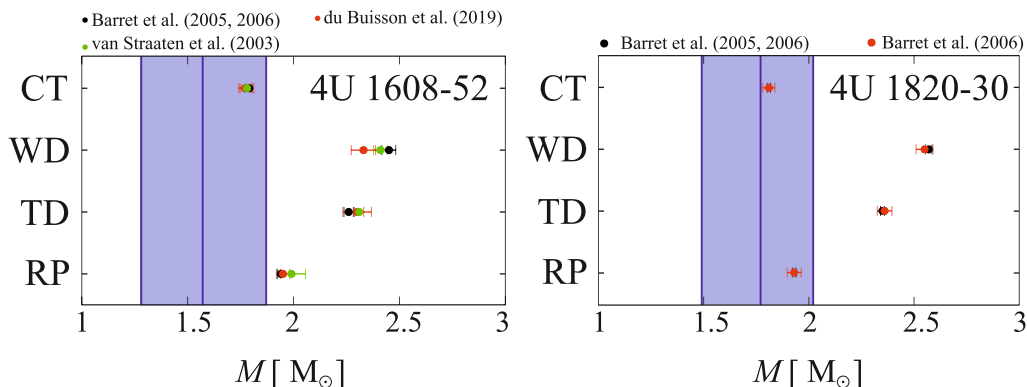


**Figure 5.6.** Estimation of the mass for two NS XRBs, comparing the mass derived from type I X-ray bursts (blue rectangles) against results from several QPO models. The WD and TD models are described in Török et al. (2019). Kateřina Klimovičová (private communication), and Török et al. (2019, 2022).

observations, a preliminary conclusion is that the CT model tends to recover spin values similar to those obtained via spectral fitting methods.

#### 5.4.2. Estimation of neutron stars mass

The Hartle-Thorne metric within the CT model provides a sufficient approximation for its application on sources with rotating NS. Furthermore, an approximate analytical formula was derived in Török et al. (2022), reproducing the model’s predictions for QPO frequencies. Applying this formula to data from several NS sources provides better fits compared to the RP model. This outcome confirms the compatibility of the CT model with the observed data.

The mass of several atoll sources obtained using the CT model in Török et al. (2022) aligns with estimates obtained from X-ray burst measurements, which is illustrated in Figure 5.6 for two chosen sources. The same method was applied to several other atoll sources, yielding mass estimates between 1.5 and 1.9  $M_{\odot}$  (Török et al. 2022).

### 5.5. Oscillations of accretion tori and QPO modulation

The oscillations of an accretion torus in the vicinity of a compact object should manifest as observable variations in the total flux. As a result, the frequencies of these oscillations can be identified in the Fourier image of the observed light curve.

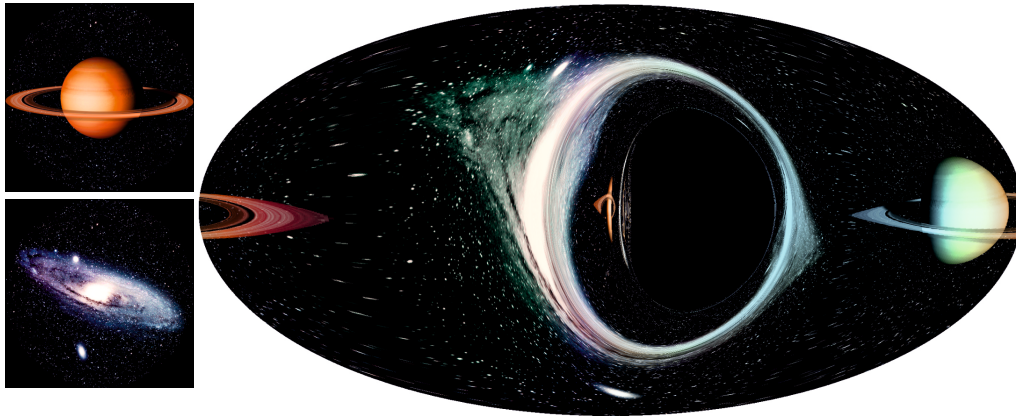


**Figure 5.7.** A ray-traced full-sky image for an observer in front of an extreme Kerr BH, a planet behind, and a galaxy in front of them. This visualization includes gravitational lensing, higher-order images, and Doppler and gravitational shifts in the photons' energy. Created by Pavel Bakala, ([Bakala et al. 2015b](#)).

However, the propagation of light close to a compact object is governed by the effects of GR. To achieve a realistic representation, it is necessary to numerically solve the null geodesic equations determining the trajectories of photons. This can be accomplished using a relativistic ray-tracing code, which accurately simulates the paths of photons in curved spacetimes ([Bakala et al. 2015b](#); [Beckwith & Done 2005](#); [Bronzwaer et al. 2018](#); [Chan et al. 2013](#); [Cunningham & Bardeen 1973](#); [Dexter & Agol 2009](#); [Karas et al. 1992](#); [Prather et al. 2023](#); [Schnittman & Rezzolla 2006](#); [Vincent et al. 2011](#)).

### 5.5.1. Relativistic ray tracing with the LSD code

Several ray-tracing codes implementing various numerical methods are available, including the HEROIC code mentioned in Chapter 4. For a comprehensive overview of relativistic radiative transfer codes, see [Prather et al. \(2023\)](#). Within the context of QPOs, ray tracing simulations were pioneered by [Bursa \(2005\)](#); [Bursa et al. \(2004\)](#); [Schnittman \(2005\)](#); [Schnittman & Bertschinger \(2004\)](#); [Schnittman et al. \(2006a,b\)](#). A novel ray-tracing code has also been developed in our research group – the Lensing Simulation Device (LSD) ([Bakala et al. 2015b, 2007](#)).

The LSD code directly integrates the null geodesics in the direction from the observer, allowing for the computation of individual photon trajectories. This approach uniquely considers time delays between different photons, including those from second or higher-order images, which orbit the BH several times

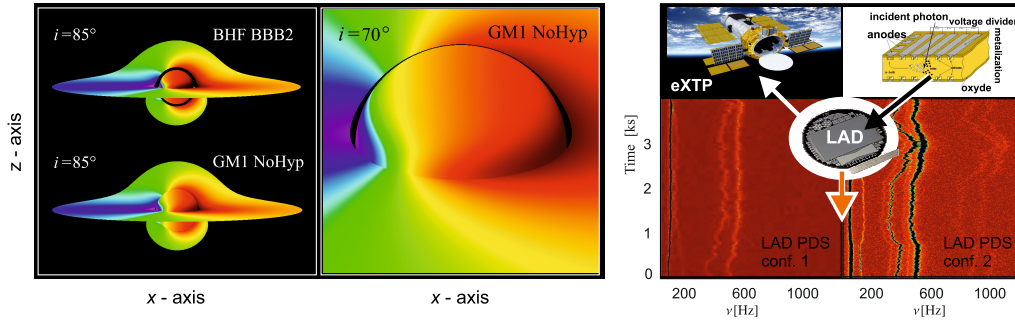


**Figure 5.8.** *Left:* G-factor maps illustrating the Doppler effect for a thin disk around a rotating NS for two different equations of state while maintaining the same mass and rotational frequency. *Middle:* Detail of the spreading boundary layer on the NS surface. Both illustrations are adopted from Šprña et al. (in preparation). *Right:* The LAD detector on board the eXTP satellite and examples of simulated spectrograms of an accreting system with a NS. Illustration from (Karas et al. 2023).

before escaping toward the observer. While this time difference may not be significant in most scenarios, its incorporation leads to higher accuracy of results when simulating rapid time variability.

The LSD code consists of two separate components. The first one performs ray tracing, following the photon paths in a given (curved, axially symmetric) space-time from the observer at a given location to the point of origin of such photon. This “backward” ray tracing strategy significantly enhances computational efficiency.

The second part calculates the intersection of these photon paths with objects of general geometry, accounting for obscuration by multiple bodies. These sources are defined by their radiating surface (photosphere) and 4-velocity. The initial step involves generating geodesics for a specified space-time and the observer’s position and resolution. Subsequently, the radiating object is inserted into the photon paths to calculate its lensed picture, light curve, and spectra. The calculated photon geodesics can be reused for different objects, further enhancing computational efficiency.

The LSD code has a wide range of applications, from simulating observable spectra and light curves to studying the subtle, hidden spectral features and immediate surroundings of compact objects, to illustrating the impacts of strong gravity for science popularization and immersive media (see Figure 5.9 for the former, and 5.7 for the latter). The LSD code can be applied to precisely model the signal from an X-ray source for a distant observer in the context of X-ray instrument development, enabling testing and verifying the capabilities of oper-



ating and planned X-ray telescopes. An example of such utilization is shown in Figure 5.8, in the case of the Large Area Detector (LAD) aboard the proposed enhanced X-ray Timing and Polarimetry (eXTP) mission.

Moreover, the LSD code is valuable in modelling the interactions between multiple objects in the strong gravitational fields, accounting for the mutual obscuration effects. Furthermore, it can simulate the observable spectra, e.g., from a system consisting of a thin disk around a NS and a boundary layer on its surface (Šprňa et al. in preparation), as illustrated in the left part of Figure 5.8 (Bakala et al. 2014; De Rosa et al. 2019; Feroci et al. 2022; Zhang et al. 2016).

In the context of the QPO modelling, the LSD code can simulate an object in the vicinity of a compact object and its time evolution, producing individual spectra and spatially resolved pictures. However, the code does not solve the radiative transfer through the material, and thus the effects on the spectral shape and distribution arise solely from the GR effects. The capabilities of the LSD code are illustrated in Figure 5.9 for various scenarios of a BH or a NS accretion and its application for demonstrating light behaviour in strong gravity.

### 5.5.2. Ray-traced models

To demonstrate the capabilities of the LSD code and to compare three distinct approaches to QPO modelling, we analyze both the temporal and frequency domain outputs obtained from simulations of three families of QPO models for both BH and NS sources. These simulations are carried out using the LSD code, incorporating relativistic effects on photon propagation and mutual obscuration of all components through ray tracing. This work is based on Török et al. (2022) and Karas et al. (2023) alongside an ongoing project. Therefore, exhaustive details regarding simulation settings, parameter space exploration, and a thorough analysis of results are beyond the scope of this thesis. The current discussion should be considered illustrative, demonstrating the differences and similarities between the models.

The three families of models (**M1-M3**) for both the NS and BH cases are considered as follows:

- **M1:** Models assuming a torus oscillating closely to the central object in both vertical and radial directions, based on the work of Abramowicz & Kluźniak (2001, 2004); Kluźniak & Abramowicz (2001).
- **M2:** Models considering orbital motion and oscillations of torus or products of torus instabilities. These models are based on the scenario suggested in Török et al. (2022), which involve epochs of stable torus oscillations alter-

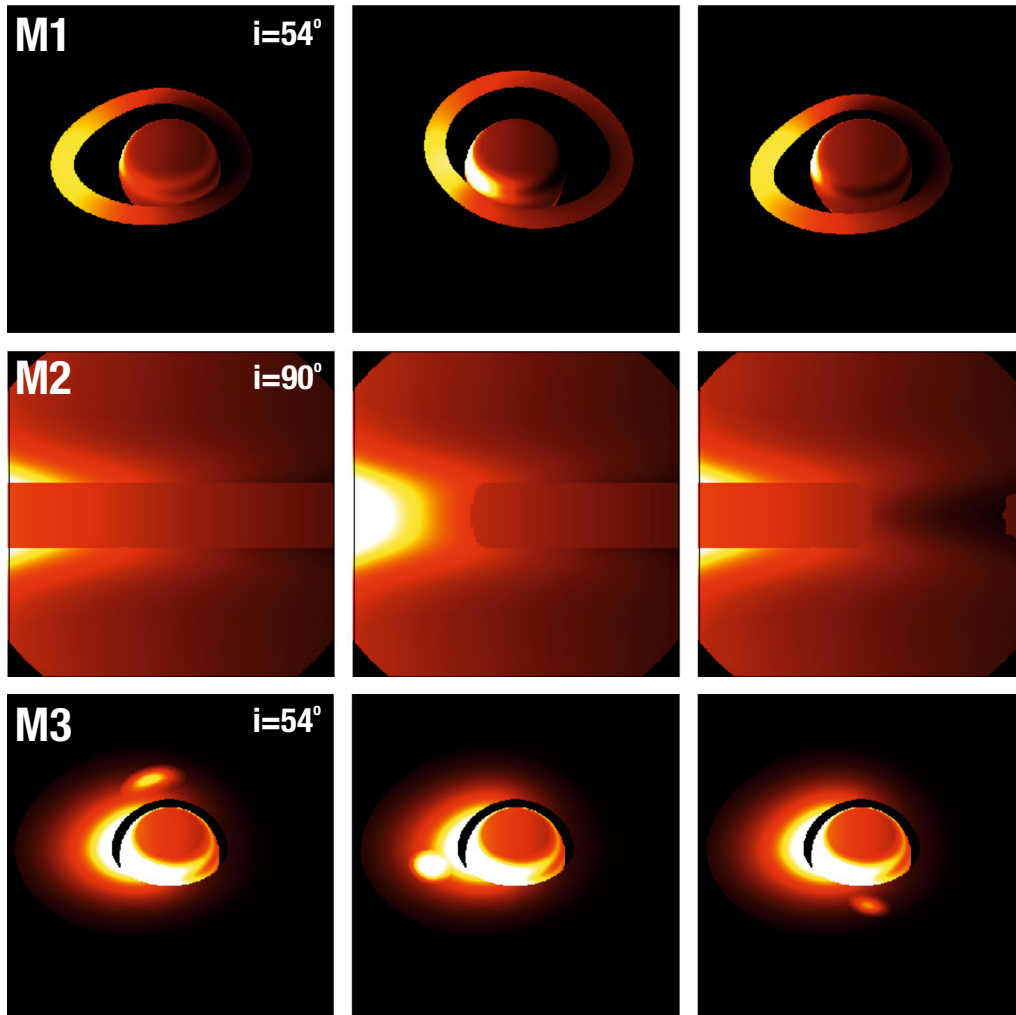


**Figure 5.9.** Colourmaps illustrating the relative bolometric intensity of the observable radiation for configurations corresponding to the **M1-M3** families of models, simulated using the LSD code. Three arbitrarily selected snapshots from the temporal evolution of each configuration are shown. Adopted from [Karas et al. \(2023\)](#). *Top*: A radially oscillating torus around a NS, where torus oscillations modulate the boundary layer luminosity. *Middle*: A detailed equatorial view of the NS boundary layer on its surface and a torus fragment orbiting it. *Bottom*: A hot spot orbiting within a thin accretion disk around a NS with a luminous boundary layer.

nating with periods where instability emerges, leading to the formation of one or more torus fragments (Goodman et al. 1987).

- **M3**: Models assuming the presence of one or more hot spots orbiting in proximity to the compact object within an accretion disk. These models are based on work of Kluźniak et al. (1990) and Stella & Vietri (1999).

To explore these families of models, we adopt the methodology introduced by Bursa (2005); Bursa et al. (2004). Our approach assumes optically thick tori and employs a simplified torus thermodynamics (Karas et al. 2023). Additionally, for the NS case, a luminous NS boundary (spreading) layer is included in the simulations (Inogamov & Sunyaev 1999). Based on works of Abramowicz et al. (2006); Horák (2005); Paczynski (1987) and findings of Parthasarathy et al. (2017), our simulations include the modulation of the NS boundary layer luminosity due to radial oscillations of the torus.

The **M1** and **M2** families are intrinsically connected, both revolving around the concept of accretion tori, although in very different configurations. On the contrary, the **M3** family is built on different assumptions and is listed for comparison. Illustrations of the observational pictures and evolution of particular configurations of the **M1-M3** families of models are shown in Figure 5.9.

### 5.5.3. Simulations setup

The families of models can each accommodate a variety of models with diverse parameters, including the radial coordinate of the torus centre, oscillations modes and symmetry, number of spots or torus fragments, and more. The simulations presented in this section are selected as representative examples from these families. For the sake of simplicity, a non-rotating NS and BH is assumed, and in each case, the torus (or spot) is located at radius  $r_0 = 6.75 r_g$ , where, as illustrated in Figure 5.2,  $f_K = 3f_r$ . The mass of the BH is  $M = 5 M_\odot$ , and in the NS case, the mass is  $M = 1.4 M_\odot$  and radius  $R_* = 10 \text{ km}$  (which is the same as in Figure 5.2).

The specific parameters for each simulation are:

- **M1**: Torus exhibiting axisymmetric radial and vertical oscillations.
- **M2**: Torus fragment as the products of instabilities exhibiting axisymmetric radial oscillations.
- **M3**: A single orbiting spot with radial precession.

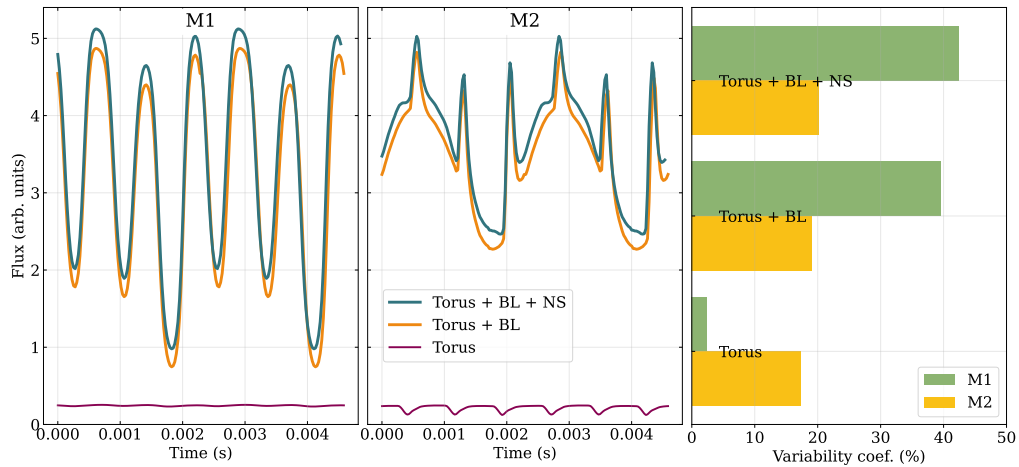


**Figure 5.10.** Light curves obtained for models **M1** (*left*) and **M2** (*middle*) in the NS case. The extension corresponds to two Keplerian orbits at  $r_0$ . The individual components of the models are disassembled, and separate light curves are shown while maintaining the effects of mutual obscuration (the objects are included in the simulations, but they do not radiate). The green line corresponds to the full model, the yellow for the torus and boundary layer, and the red one solely for the torus. In the *right* panel, the variability coefficients for both models and all the components are shown.

#### 5.5.4. Simulations results

Figure 5.10 presents the light curves and variability for models representing families **M1** and **M2**. Due to the substantial luminosity of the NS boundary layer, which corresponds to releasing a significant fraction of accreted energy, the torus contributes relatively less to the overall variability than the pulsating, periodically obscured boundary layer. In this context, the torus acts as “clock” that determines the observed NS variability, while the NS acts as an “amplifier” enhancing the signal. This sets produced signals apart from that of the BH systems.

Possible observable PSDs of these simulations are presented in Figure 5.11. Following the approach of Bakala et al. (2014), the pure signal obtained from simulations **M1-M3** is combined with a typical X-ray background associated with the hard spectral state of an XRB, along with white noise.

The accretion rate modulation due to the radial oscillations of cusp tori was confirmed in MHD simulations (Parthasarathy et al. 2017). However, they identified an apparent absence of modulation caused by vertical oscillations. The obscuration of the boundary layer by the torus and the accretion rate modulation, recovers the observed frequency peak corresponding to the vertical oscillations.

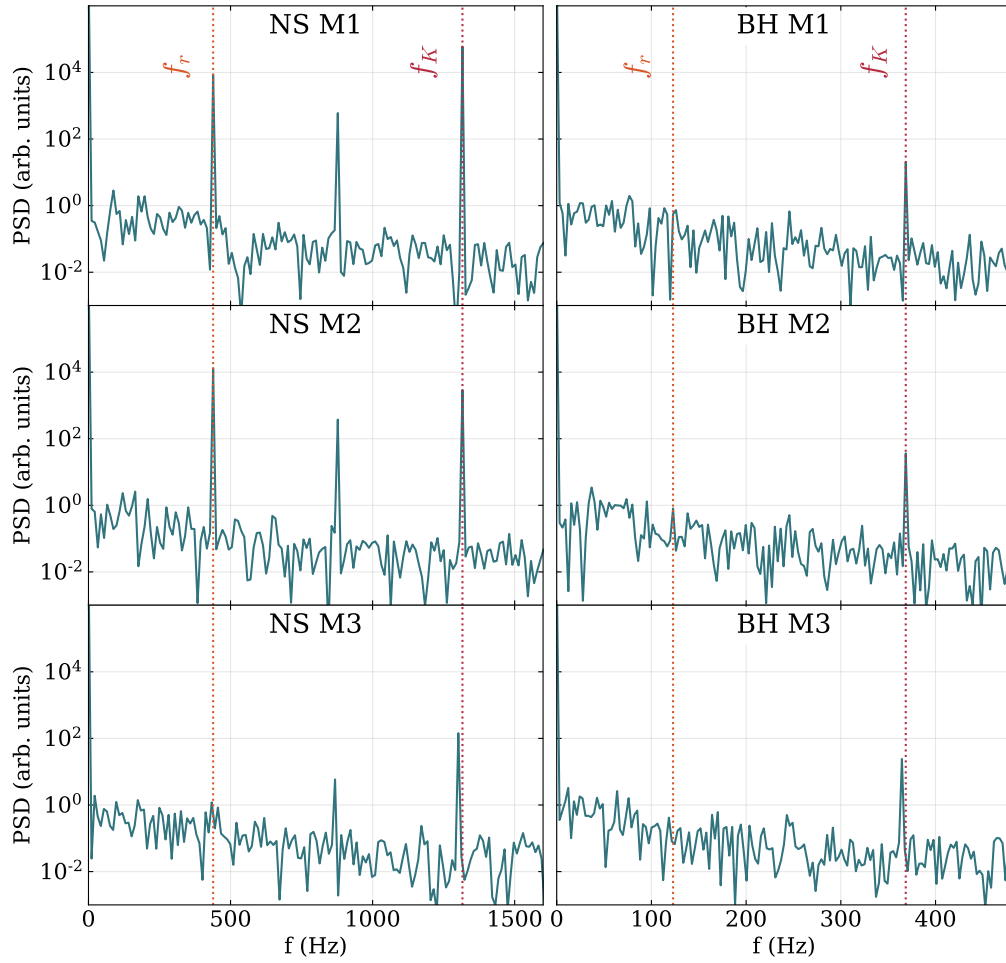


**Figure 5.11.** Simulated PSD for selected QPO models in the case of the NS (*left*) and BH (*right*) systems for the inclination angle of the observer  $i = 70^\circ$ .

The results presented in this section regarding the combined modulation of QPOs are part of ongoing work and are relevant to a wide range of models. A preliminary discussion of these results was presented at a conference and is included in a recently submitted paper (Karas et al. 2023). These findings have implications for models based on the resonance of the fundamental frequencies of orbital oscillations (Abramowicz & Kluźniak 2001; Kluźniak & Abramowicz 2001), the CT model (Török et al. 2016a, 2022), models by Rezzolla and collaborators (Rezzolla et al. 2003), or the model by Ingram and collaborators (Ingram & Done 2010). One can also expect that for the last model, strong constraints on the physical properties of the “toroidal structure” assumed within the model will be implied.

## Summary

My work aimed to model the accretion disks in XRBs featuring either a BH or a NS. The main objective was to employ advanced numerical techniques to uncover the underlying processes governing the observed spectral and timing properties.

One notable outcome of this modelling was the recognition of the puffy accretion disk, a novel type of accretion disk based purely on the results of numerical simulations. This innovative model covers the previously not fully explored gap between the thin and slim disk analytical models. Moreover, these results have been used to test the simplified analytical models to verify their validity, stability, and whether they can correctly interpret the observed data.

Modelling accreting systems presents a challenge due to the broad spectrum of timescales. These timescales span from resolving the turbulent processes that govern viscosity and angular momentum transport within microseconds to accurately modelling the complex oscillations responsible for observed temporal variability on timescales of tens of seconds. Two approaches can be taken to address these challenges. The first is to model the accretion flow within the disk self-consistently during different states. The second approach involves using simplified analytical models of the disk and focusing on its oscillatory behaviour in the context of GR. I have pursued both paths during my studies.

## Overview of the collection of papers

### **Paper 1: Puffy Accretion Disks: Sub-Eddington, Optically Thick, and Stable**

In this Letter, [Lančová et al. \(2019\)](#), we report on a new class of solutions for BH accretion disks derived from the results of global 3D GRRMHD simulations. This solution combines features of the canonical thin, slim, and thick disk models but differs from each in crucial ways; thus, we named it the *puffy disk*. The puffy disk provides a more realistic description of BH accretion. The solution

is presented for a non-spinning BH with a sub-Eddington mass accretion rate. The disk appears thin based on the density scale height, but most inflow occurs through a highly turbulent, optically thick, Keplerian region. The magnetic field supports the accreting fluid, making the disk thermally stable. The implications for understanding optically thick accretion disks and modelling BH sources are also discussed.

### **Paper 2: Observational properties of puffy discs: radiative GRMHD spectra of mildly sub-Eddington accretion**

The puffy disk observational picture is described in this paper, [Wielgus et al. \(2022\)](#). It explores the observational properties of puffy disks, including their geometrical obscuration at higher inclinations of the observer, and the collimation of radiation along the spin axis, including the discussion on similarities of the output of the simulations with various states of microquasars or ULXs. The paper also examines the fitting of puffy disk spectra using standard spectral models in XSPEC and discusses the limitations of these models in correctly recovering the BH spin and mass accretion rate. Although the synthetic spectra of puffy disks are qualitatively similar to those of a Comptonized thin disk, other important properties, such as the dependency on the inclination angle of the observer, or the hardness ratio, are distinct from the analytical picture.

### **Paper 3: Spectra of puffy accretion discs: the kynbb fit**

This paper, [Lančová et al. \(2023\)](#), published in the proceedings of 2022 XMM-Newton meeting in Madrid, we investigated the accuracy of spectral models in interpreting synthetic spectra of the puffy accretion disk in XRBs. The `kerrbb` and `kynbb` models in XSPEC were applied to the puffy disk simulated spectra to verify and extend the results of fitting in [Wielgus et al. \(2022\)](#) (Paper 2). The results show that neither of the models accurately recovers the parameters of the accretion disk, the BH spin, or the mass accretion rate. This suggests that new, more accurate spectral models for BH XRBs' luminous regimes are needed. The paper proposes that these new models should be based on the results of numerical simulations. The findings suggest that the traditional thin accretion disk models may not be suitable for accurately interpreting the spectra of XRBs with a sub-Eddington luminosity.



#### **Paper 4: Models of high-frequency quasi-periodic oscillations and black hole spin estimates in Galactic microquasars**

This paper, [Kotrllová et al. \(2020\)](#), examined the influence of pressure forces on the frequencies of oscillations of accretion disks around BHs. The effect of the pressure forces was examined in the framework of various QPOs models and its consequences for BH spin estimations. The study focuses on HF QPOs observed in the X-ray flux of Galactic microquasars. Several QPOs models based on oscillations of accretion tori were considered, and we examined the consequences for estimates of the BH spin. The paper concludes that, for some of the models, the pressure significantly impacts the spin estimates.

#### **Paper 5: Simple Analytic Formula Relating the Mass and Spin of Accreting Compact Objects to Their Rapid X-Ray Variability**

In this paper, [Török et al. \(2022\)](#), the CT model was extended and applied to explain observed HF QPOs in NS XRBs. The CT model is based on oscillations of marginally overflowing accretion tori with cusps. The paper derives an analytic formula for rotating compact objects in Kerr and Hartle-Thorne spacetimes. The formula accurately reproduces the predictions of the numerical model for QPOs frequencies. The formula is well applicable to rotating oblate NSs. Its application on data from several NS sources provides better fits of observed data compared to the RP model, confirming the compatibility of the CT model with the data.

#### **Paper 6: Oscillations of non-slender tori in the external Hartle-Thorne geometry**

This paper, [Matuszková et al. \(2022\)](#), published in the Proceedings of RAGtime 20-22<sup>1</sup> studies the influence of the quadrupole moment of a slowly rotating NS on the oscillations of non-slender accretion tori. The analytical calculations are applied to determine the frequencies of the radial epicyclic mode of a torus in the Hartle-Thorne geometry. These frequencies are then compared to those obtained, assuming standard and linearized Kerr metrics. The paper states that while the shape of tori is not significantly affected by the quadrupole moment, the frequencies of oscillations are affected significantly. The paper suggests that considering the quadrupole moment of a NS is important for HF QPOs modelling.

---

<sup>1</sup> <https://proceedings.physics.cz/proceedings-of-ragtime-20-22/>



## List of Symbols

Symbol	Meaning
$\mathbf{A}_{dyn}$	dynamo-generated vector potential
$A_{\hat{\phi}}$	azimuthal vector potential
$B^i, \mathbf{B}$	magnetic field 3-vector
$\mathbf{B}_{dyn}$	dynamo-generated magnetic field
$B_{\hat{p}}$	orthonormal poloidal component of the magnetic field
$B_{\hat{\phi}}$	orthonormal azimuthal component of the magnetic field
$B_*$	magnetic field strength on the surface of star
$\widehat{B}$	frequency-integrated Planck function
$E$	radiative energy density
$\mathbf{E}$	electric field 3-vector
$F$	local radiative flux
$F^i$	radiative flux
$F_g$	gravitational force
$\mathbf{F}^L$	left flux through cell face
$\mathbf{F}^R$	right flux through cell face
$F_r$	radiation force
$F^{*\mu\nu}$	dual tensor of the electromagnetic field
$G$	gravitational constant
$G_\mu$	radiative 4-force density
$H$	half-thickness of a disk
$I$	frequency-integrated specific intensity
$I_\nu$	specific intensity
$J$	BH angular momentum
$\mathbf{J}_{\hat{p}}$	poloidal current
$L$	luminosity
$L_{Edd}$	Eddington luminosity
$M$	mass
$M_A$	mass of accretor
$M_D$	mass of donor star

---

$M_{\odot}$	solar mass
$\dot{M}$	mass accretion rate
$\dot{M}_{\text{Edd}}$	critical mass accretion rate
$N^i$	unit vector in direction $x^i$
$P$	rotation period
$P(\nu)$	Function of a steep power-law state of XRB
$\mathbf{P}$	vectors of primitive quantities
$p^{ij}$	radiation pressure tensor
$Q$	BH charge
$\mathbf{Q}^L$	left state
$\mathbf{Q}^R$	right state
$Q_{\phi}$	quality parameter in $\phi$ direction
$Q_{\theta}$	quality parameter in $\theta$ direction
$Q_{\text{visc}}^+$	viscous heating
$Q_{\text{rad}}^-$	radiative cooling
$R_{\text{circ}}$	circularization radius
$R_{\nu}^{\mu}$	radiation stress-energy tensor
$R_{\text{visc}}^{\mu\nu}$	radiation viscous term
$R_*$	radius of a star
$S$	gas entropy per unit volume
$\mathbf{S}^L$	left maximal speed in cell face
$S^{\text{max}}$	maximal signal speed in cell
$\mathbf{S}^R$	right maximal speed in cell face
$T$	temperature
$T_g$	gas temperature
$T_R$	radiation temperature
$T^{\mu\nu}$	gas stress-energy tensor
$\mathbf{U}$	vectors of conserved quantities

---

$a$	BH spin
$a$	radiation constant
$b^{\mu}$	4-vector of magnetic field
$c$	speed of light
$ds$	spacetime interval
$f_K$	Keplerian orbital frequency
$f_P$	periastron precession frequency
$f_r$	radial epicyclic frequency
$f_{\theta}$	vertical epicyclic frequency
$f_*$	rotational frequency of star
$g$	metric determinant

---

$g_{\mu\nu}$	metric tensor
$h_\rho$	density scale-height
$h_\tau$	photosphere height
$h_R^{\mu\nu}$	projection tensor
$k_B$	Boltzmann constant
$m$	mass in units of $M_\odot$
$m_e$	electron mass
$m_{p^+}$	proton mass
$\dot{m}$	mass accretion rate
$p$	pressure
$p_{\text{gas}}$	gas pressure
$p_{\text{mag}}$	magnetic pressure
$q$	mass ratio
$q$	non-dimensional quadrupole moment of a NS
$r_0$	position of center of torus
$r_{\text{co}}$	corotation radius
$r_e^\pm$	ergosphere in Kerr metric
$r_g$	gravitational radius
$r_h^\pm$	horizons in Kerr metric
$r_{\text{ISCO}}$	radius of ISCO
$r_{\text{lc}}$	light cylinder radius
$r_{\text{mag}}$	magnetospheric radius
$r_{\text{mb}}$	marginally bound orbit
$r_{\text{ph}}$	photon orbit
$r_{\text{Schw}}$	Schwarzschild radius
$r_{\text{trap}}$	photon trapping radius
$r_*$	radius in cm
$s$	binary separation
$t_{\text{acc}}$	accretion time
$t_{\text{diff}}$	photon diffusion time
$t_{\text{dyn}}$	dynamical time-scale
$t_g$	gravitational radius crossing time
$t_{r\phi}$	viscous stress
$t_{\text{th}}$	thermal time-scale
$t^{\mu\nu}$	stress-energy tensor
$u_{\text{int}}$	internal energy density
$u^\mu$	lab frame 4-velocity
$\tilde{u}_R^\mu$	radiation rest frame 4-velocity

$v^j = (v^r, v^\theta, v^\phi)$	vector of 3-velocity
$\Delta t$	time step
$\Delta x$	cell size
$\Gamma$	adiabatic index
$\Gamma^\alpha_{\beta\gamma}$	Christoffel symbols
$\Omega$	angular velocity
$\Omega$	solid angle
$\Sigma$	surface density
$\Omega_K$	Keplerian angular velocity
$\alpha$	viscous coefficient
$\alpha_{dyn}$	dynamo coefficient
$\alpha_{rad}$	radiative viscous coefficient
$\beta$	magnetic-to-total pressure ratio
$\beta$	Thickness parameter of torus
$\beta_{cusp}$	Thickness parameter of a cusp torus
$\eta$	energy conversion efficiency
$\eta_{md}$	magnetic diffusivity coefficient
$\eta^{\mu\nu}$	Minkowski metric
$\theta_{MM}$	minmoddiffusivity parameter
$\kappa_a$	absorption opacity
$\kappa_{es}$	electron scattering opacity
$\lambda$	mean free path of photons
$\lambda_{MRI}$	characteristic MRI wavelength
$\mu$	magnetic moment
$\mu_{30}$	magnetic moment in the units of $10^{30} \text{ G} \cdot \text{cm}^3$
$\nu$	frequency
$\nu^A$	Alfvén speed
$\nu_L$	Observed lower peak of HF QPOs
$\nu_U$	Observed upper peak of HF QPOs
$\nu_{rad}$	radiative viscosity coefficient
$\xi$	magnetic tilt angle
$\rho$	Gas density
$\sigma_R^{\mu\nu}$	radiation shear tensor
$\sigma_T$	Thomson cross-section
$\tau$	optical depth
$\chi$	total opacity coefficient
$(-, +, +, +)$	metric signature
$(r, \theta, \phi)$	spacial coordinates
$(t, r, \theta, \phi)$	spacetime coordinates

---

Latin indices	$(i, j, k, \dots)$ (1,2,3)
Greek indices	$(\alpha, \beta, \gamma, \dots)$ (0,1,2,3)

---





## List of Abbreviations

Abbreviations	Meaning
ADAF	Advection Dominated Accretion Flow
AGN	Active Galactic Nuclei
BH	Black Hole
BL	Boyer–Lindquist (coordinates)
CCD	Colour-Colour Diagram
CFL	Courant–Friedrichs–Lewy (condition)
CT	Constrained Transport
CT	Cusp Torus
EHT	Event Horizon Telescope
EM	Electromagnetic
eXTP	enhanced X-ray Timing and Polarimetry (mission)
FBO	Flaring Branch Oscillations
GR	General Relativity
GRRMHD	General Relativistic Radiative Magnetohydrodynamic
GW	Gravitational Waves
HBO	Horizontal Branch Oscillations
HD	Hydrodynamics
HF QPOs	High Frequency QPOs
HID	Hardness Intensity Diagram
HLL	Harten–Lax–van Leer (Riemann solver)
HMXB	High-Mass X-ray Binary
IMEX	Implicit-Explicit
ISCO	Innermost Stable Circular Orbit
KS	Kerr-Schild
LAD	Large Area Detector
LF QPOs	Low Frequency QPOs
LMXB	Low-Mass X-ray Binary
LSD	Lensing Simulation Device
LTE	Local Thermal Equilibrium

MHD	Magnetohydrodynamics
MKS	Modified Kerr-Schild (coordinates)
MPI	Message Parsing Interface
MRI	Magnetorotational Instability
NBO	Normal Branch Oscillations
NS	Neutron Star
PSD	Power Spectral Density
RP	Relativistic Precession
QPO	Quasi-periodic Oscillations
RR	Relativistic Reflection
RXTE	Rossi X-Ray Timing Explorer
SED	Spectral Energy Distribution
TDE	Tidal Disruption Event
ULX	Ultraluminous X-ray source
UV	Ultraviolet
XRB	X-ray Binary
ZAMO	Zero Angular Momentum Observer

---

## References

- Abbott, B. P., Abbott, R., Abbott, T. D., et al., Observation of Gravitational Waves from a Binary Black Hole Merger. 2016, *Phys. Rev. Lett.*, **116**, 061102, DOI: 10.1103/PhysRevLett.116.061102
- Abramowicz, M., Jaroszyński, M., & Sikora, M., Relativistic, accreting disks. 1978, *A&A*, **63**, 221
- Abramowicz, M. A., Blaes, O. M., Horák, J., Kluźniak, W., & Rebusco, P., Epicyclic oscillations of fluid bodies: II. Strong gravity. 2006, *Classical and Quantum Gravity*, **23**, 1689, DOI: 10.1088/0264-9381/23/5/014
- Abramowicz, M. A., Bulik, T., Bursa, M., & Kluźniak, W., Evidence for a 2:3 resonance in Sco X-1 kHz QPOs. 2003, *Astron. Astrophys.*, **404**, L21, DOI: 10.1051/0004-6361:20030737
- Abramowicz, M. A., Czerny, B., Lasota, J. P., & Szuszkiewicz, E., Slim Accretion Disks. 1988, *ApJ*, **332**, 646, DOI: 10.1086/166683
- Abramowicz, M. A. & Kluźniak, W., A precise determination of black hole spin in GRO J1655-40. 2001, *Astron. Astrophys.*, **374**, L19, DOI: 10.1051/0004-6361:20010791
- Abramowicz, M. A. & Kluźniak, W., Interpreting black hole QPOs. 2004, in American Institute of Physics Conference Series, Vol. **714**, *X-ray Timing 2003: Rossi and Beyond*, ed. P. Kaaret, F. K. Lamb, & J. H. Swank, 21–28
- Abramowicz, M. A., Kluźniak, W., McClintock, J. E., & Remillard, R. A., The Importance of Discovering a 3:2 Twin-Peak Quasi-periodic Oscillation in an Ultraluminous X-Ray Source, or How to Solve the Puzzle of Intermediate-Mass Black Holes. 2004, *Astrophys. J. Lett.*, **609**, L63, DOI: 10.1086/422810
- Alabarta, K., Altamirano, D., Méndez, M., et al., Failed-transition outbursts in black hole low-mass X-ray binaries. 2021, *Mon. Not. R. Astron. Soc.*, **507**, 5507, DOI: 10.1093/mnras/stab2241
- Alpar, M. A. & Shaham, J., Is GX5 - 1 a millisecond pulsar? 1985, *Nature*, **316**, 239, DOI: 10.1038/316239a0
- Ambartsumian, V. A., On the evolution of galaxies. 1958, in *11ème Conseil de Physique de l'Institut International de Physique Solvay: La structure et l'évolution de l'univers : rapports et discussions*, 241–280

- Anile, A. M. 1989, *Relativistic fluids and magneto-fluids: With applications in astrophysics and plasma physics* (Cambridge University Press)
- Anninos, P., Fragile, P. C., & Salmonson, J. D., Cosmos++: Relativistic Magneto-hydrodynamics on Unstructured Grids with Local Adaptive Refinement. 2005, *Astro-phys. J.*, **635**, 723, DOI: 10.1086/497294
- Arnaud, K. A., XSPEC: The First Ten Years. 1996, in Astronomical Society of the Pacific Conference Series, Vol. **101**, *Astronomical Data Analysis Software and Systems V*, ed. G. H. Jacoby & J. Barnes, 17
- Avakyan, A., Neumann, M., Zainab, A., et al., XRBCats: Galactic Low Mass X-ray Binary Catalogue. 2023, *arXiv e-prints*, arXiv:2303.16168, DOI: 10.48550/arXiv.2303.16168
- Bakala, P., De Falco, V., Battista, E., et al., Three-dimensional general relativistic Poynting-Robertson effect. II. Radiation field from a rigidly rotating spherical source. 2019, *Phys. Rev. D*, **100**, 104053, DOI: 10.1103/PhysRevD.100.104053
- Bakala, P., Goluchová, K., Török, G., et al., Twin peak high-frequency quasi-periodic oscillations as a spectral imprint of dual oscillation modes of accretion tori. 2015a, *Astron. Astrophys.*, **581**, A35, DOI: 10.1051/0004-6361/201525867
- Bakala, P., Goluchová, K., Török, G., et al., Twin peak high-frequency quasi-periodic oscillations as a spectral imprint of dual oscillation modes of accretion tori. 2015b, *A&A*, **581**, A35, DOI: 10.1051/0004-6361/201525867
- Bakala, P., Török, G., Karas, V., et al., Power density spectra of modes of orbital motion in strongly curved space-time: obtaining the observable signal. 2014, *Mon. Not. R. Astron. Soc.*, **439**, 1933, DOI: 10.1093/mnras/stu076
- Bakala, P., Čermák, P., Hledík, S., Stuchlík, Z., & Truparová, K., Extreme gravitational lensing in vicinity of Schwarzschild-de Sitter black holes. 2007, *Central European Journal of Physics*, **5**, 599, DOI: 10.2478/s11534-007-0033-6
- Balbus, S. A. & Hawley, J. F., A Powerful Local Shear Instability in Weakly Magnetized Disks. I. Linear Analysis. 1991, *The Astrophysical Journal*, **376**, 214, DOI: 10.1086/170270
- Balbus, S. A. & Hawley, J. F., Turbulent transport in accretion disks. 1998, in American Institute of Physics Conference Series, Vol. **431**, *Accretion processes in Astrophysical Systems: Some like it hot! - eighth AstroPhysics Conference*, ed. S. S. Holt & T. R. Kallman, 79–88
- Bambi, C. 2017, *Black Holes: A Laboratory for Testing Strong Gravity* (Springer)
- Bardeen, J. M., Press, W. H., & Teukolsky, S. A., Rotating Black Holes: Locally Nonrotating Frames, Energy Extraction, and Scalar Synchrotron Radiation. 1972, *The Astrophysical Journal*, **178**, 347, DOI: 10.1086/151796
- Barret, D., Kluźniak, W., Olive, J. F., Paltani, S., & Skinner, G. K., On the high coherence of kHz quasi-periodic oscillations. 2005, *Mon. Not. R. Astron. Soc.*, **357**,

1288, DOI: 10.1111/j.1365-2966.2005.08734.x

Beckwith, K. & Done, C., Extreme gravitational lensing near rotating black holes. 2005, *Mon. Not. R. Astron. Soc.*, **359**, 1217, DOI: 10.1111/j.1365-2966.2005.08980.x

Begelman, M. C. & Pringle, J. E., Accretion discs with strong toroidal magnetic fields. 2007, *Mon. Not. R. Astron. Soc.*, **375**, 1070, DOI: 10.1111/j.1365-2966.2006.11372.x

Belczynski, K., Bulik, T., Fryer, C. L., et al., On the Maximum Mass of Stellar Black Holes. 2010, *Astrophys. J.*, **714**, 1217, DOI: 10.1088/0004-637X/714/2/1217

Bildsten, L. & Cumming, A., Hydrogen Electron Capture in Accreting Neutron Stars and the Resulting g-Mode Oscillation Spectrum. 1998, *Astrophys. J.*, **506**, 842, DOI: 10.1086/306279

Blaes, O. M., Arras, P., & Fragile, P. C., Oscillation modes of relativistic slender tori. 2006, *Mon. Not. R. Astron. Soc.*, **369**, 1235, DOI: 10.1111/j.1365-2966.2006.10370.x

Blaes, O. M., Šrámková, E., Abramowicz, M. A., Kluźniak, W., & Torkelsson, U., Epicyclic Oscillations of Fluid Bodies: Newtonian Nonslender Torus. 2007, *Astrophys. J.*, **665**, 642, DOI: 10.1086/519782

Blandford, R. D. & Znajek, R. L., Electromagnetic extraction of energy from Kerr black holes. 1977, *Mon. Not. R. Astron. Soc.*, **179**, 433, DOI: 10.1093/mnras/179.3.433

Bollimpalli, D. A., Mahmoud, R., Done, C., et al., Looking for the underlying cause of black hole X-ray variability in GRMHD simulations. 2020, *Mon. Not. R. Astron. Soc.*, **496**, 3808, DOI: 10.1093/mnras/staa1808

Bombaci, I., The maximum mass of a neutron star. 1996, *Astron. Astrophys.*, **305**, 871

Bondi, H., On spherically symmetrical accretion. 1952, *Mon. Not. R. Astron. Soc.*, **112**, 195, DOI: 10.1093/mnras/112.2.195

Boutelier, M., Barret, D., Lin, Y., & Török, G., On the distribution of frequency ratios of kHz quasi-periodic oscillations. 2010, *Mon. Not. R. Astron. Soc.*, **401**, 1290, DOI: 10.1111/j.1365-2966.2009.15724.x

Boyer, R. H. & Lindquist, R. W., Maximal Analytic Extension of the Kerr Metric. 1967, *Journal of Mathematical Physics*, **8**, 265, DOI: 10.1063/1.1705193

Bradt, H. V., Rothschild, R. E., & Swank, J. H., X-ray timing explorer mission. 1993, *Astron. Astrophys. Suppl.*, **97**, 355

Bradt, H. V. D. & McClintock, J. E., The optical Counterparts of Compact discrete galactic X-Ray sources. 1983, *Annu. Rev. Astron. Astrophys.*, **21**, 13, DOI: 10.1146/annurev.aa.21.090183.000305

Brandenburg, A., The Inverse Cascade and Nonlinear Alpha-Effect in Simulations of Isotropic Helical Hydromagnetic Turbulence. 2001, *Astrophys. J.*, **550**, 824, DOI: 10.1086/319783

Brandenburg, A., Nordlund, A., Stein, R. F., & Torkelsson, U., Dynamo-generated Turbulence and Large-Scale Magnetic Fields in a Keplerian Shear Flow. 1995, *Astro-*

- phys. J.*, **446**, 741, DOI: 10.1086/175831
- Bronzwaer, T., Davelaar, J., Younsi, Z., et al., RAPTOR. I. Time-dependent radiative transfer in arbitrary spacetimes. 2018, *Astron. Astrophys.*, **613**, A2, DOI: 10.1051/0004-6361/201732149
- Bursa, M., Global oscillations of a fluid torus as a modulation mechanism for black-hole high-frequency QPOs. 2005, *Astronomische Nachrichten*, **326**, 849, DOI: 10.1002/asna.200510426
- Bursa, M., Abramowicz, M. A., Karas, V., & Kluźniak, W., The Upper Kilohertz Quasi-periodic Oscillation: A Gravitationally Lensed Vertical Oscillation. 2004, *Astrophys. J. Lett.*, **617**, L45, DOI: 10.1086/427167
- Carpano, S. & Jin, C., Discovery of a 23.8 h QPO in the Swift light curve of XMMU J134736.6+173403. 2018, *Mon. Not. R. Astron. Soc.*, **477**, 3178, DOI: 10.1093/mnras/sty841
- Casella, P., Belloni, T., & Stella, L., The ABC of Low-Frequency Quasi-periodic Oscillations in Black Hole Candidates: Analogies with Z Sources. 2005, *Astrophys. J.*, **629**, 403, DOI: 10.1086/431174
- Chael, A. A., Narayan, R., & Sądowski, A., Evolving non-thermal electrons in simulations of black hole accretion. 2017, *Mon. Not. R. Astron. Soc.*, **470**, 2367, DOI: 10.1093/mnras/stx1345
- Chan, C.-k., Psaltis, D., & Özel, F., GRay: A Massively Parallel GPU-based Code for Ray Tracing in Relativistic Spacetimes. 2013, *Astrophys. J.*, **777**, 13, DOI: 10.1088/0004-637X/777/1/13
- Chandrasekhar, S. 1998, *The Mathematical Theory of Black Holes* (Clarendon Press)
- Childs, H., Brugger, E., Whitlock, B., et al., VisIt: An End-User Tool For Visualizing and Analyzing Very Large Data. 2012, in *High Performance Visualization—Enabling Extreme-Scale Scientific Insight* (Taylor & Francis Inc), 357–372
- Ciesielski, A., Wielgus, M., Kluźniak, W., et al., Stability of radiation-pressure dominated disks. I. The dispersion relation for a delayed heating  $\alpha$ -viscosity prescription. 2012, *Astron. Astrophys.*, **538**, A148, DOI: 10.1051/0004-6361/201117478
- Coughlin, E. R. & Begelman, M. C., The General Relativistic Equations of Radiation Hydrodynamics in the Viscous Limit. 2014, *Astrophys. J.*, **797**, 103, DOI: 10.1088/0004-637X/797/2/103
- Cowling, T. G., The magnetic field of sunspots. 1933, *Mon. Not. R. Astron. Soc.*, **94**, 39, DOI: 10.1093/mnras/94.1.39
- Cunningham, C. T. & Bardeen, J. M., The Optical Appearance of a Star Orbiting an Extreme Kerr Black Hole. 1973, *Astrophys. J.*, **183**, 237, DOI: 10.1086/152223
- Dauser, T., García, J., & Wilms, J., Relativistic reflection: Review and recent developments in modeling. 2016, *Astronomische Nachrichten*, **337**, 362, DOI: 10.1002/asna.201612314

- de Avellar, M. G. B., Porth, O., Younsi, Z., & Rezzolla, L., The kilo Hertz quasi-periodic oscillations in neutron star low-mass X-ray binaries as tori oscillation modes. I. 2017, *arXiv e-prints*, arXiv:1709.07706, DOI: 10.48550/arXiv.1709.07706
- De Falco, V., Bakala, P., Battista, E., et al., Three-dimensional general relativistic Poynting-Robertson effect: Radial radiation field. 2019, *Phys. Rev. D*, **99**, 023014, DOI: 10.1103/PhysRevD.99.023014
- De Rosa, A., Uttley, P., Gou, L., et al., Accretion in strong field gravity with eXTP. 2019, *Science China Physics, Mechanics, and Astronomy*, **62**, 29504, DOI: 10.1007/s11433-018-9297-0
- Dewberry, J. W., Latter, H. N., Ogilvie, G. I., & Fromang, S., HFQPOs and discoseismic mode excitation in eccentric, relativistic discs. II. Magnetohydrodynamic simulations. 2020, *Mon. Not. R. Astron. Soc.*, **497**, 451, DOI: 10.1093/mnras/staa1898
- Dexter, J. & Agol, E., A Fast New Public Code for Computing Photon Orbits in a Kerr Spacetime. 2009, *Astrophys. J.*, **696**, 1616, DOI: 10.1088/0004-637X/696/2/1616
- Done, C., Gierliński, M., & Kubota, A., Modelling the behaviour of accretion flows in X-ray binaries. Everything you always wanted to know about accretion but were afraid to ask. 2007, *Astronomy and Astrophysics Review*, **15**, 1, DOI: 10.1007/s00159-007-0006-1
- Done, C., Wardziński, G., & Gierliński, M., GRS 1915+105: the brightest Galactic black hole. 2004, *Monthly Notices of the Royal Astronomical Society*, **349**, 393, DOI: 10.1111/j.1365-2966.2004.07545.x
- Dovčiak, M., Karas, V., & Yaqoob, T., An Extended Scheme for Fitting X-Ray Data with Accretion Disk Spectra in the Strong Gravity Regime. 2004, *Astrophys. J. Suppl. Ser.*, **153**, 205, DOI: 10.1086/421115
- Dullo, B. T., Gil de Paz, A., & Knapen, J. H., Ultramassive Black Holes in the Most Massive Galaxies:  $M_{BH}-\sigma$  versus  $M_{BH}-R_b$ . 2021, *Astrophys. J.*, **908**, 134, DOI: 10.3847/1538-4357/abceae
- Etienne, Z. B., Paschalidis, V., Haas, R., Mösta, P., & Shapiro, S. L., IllinoisGRMHD: an open-source, user-friendly GRMHD code for dynamical spacetimes. 2015, *Classical and Quantum Gravity*, **32**, 175009, DOI: 10.1088/0264-9381/32/17/175009
- Fath, E. A., The spectra of some spiral nebulae and globular star clusters. 1909, *Lick Observatory Bulletin*, **149**, 71, DOI: 10.5479/ADS/bib/1909LicOB.5.71F
- Feroci, M., Ambrosi, G., Ambrosino, F., et al., The large area detector onboard the eXTP mission. 2022, in Society of Photo-Optical Instrumentation Engineers (SPIE) Conference Series, Vol. **12181**, *Space Telescopes and Instrumentation 2022: Ultraviolet to Gamma Ray*, ed. J.-W. A. den Herder, S. Nikzad, & K. Nakazawa, 121811X
- Foschini, L., Ebisawa, K., Kawaguchi, T., et al., The application of slim disk models to ULX: The case of M33 X-8. 2006, *Advances in Space Research*, **38**, 1378, DOI: 10.1016/j.asr.2005.06.024

- Fragile, P. C., Etheridge, S. M., Anninos, P., Mishra, B., & Kluźniak, W., Relativistic, Viscous, Radiation Hydrodynamic Simulations of Geometrically Thin Disks. I. Thermal and Other Instabilities. 2018, *ApJ*, **857**, 1, DOI: 10.3847/1538-4357/aab788
- Fragile, P. C., Straub, O., & Blaes, O., High-frequency and type-C QPOs from oscillating, precessing hot, thick flow. 2016, *Mon. Not. R. Astron. Soc.*, **461**, 1356, DOI: 10.1093/mnras/stw1428
- Frank, J., King, A., & Raine, D. J. 2002, *Accretion Power in Astrophysics: Third Edition* (Cambridge University Press)
- Galassi, M. & Gough, B. 2009, *GNU Scientific Library: Reference Manual*, GNU manual (Network Theory)
- Gammie, C. F., McKinney, J. C., & Tóth, G., HARM: A Numerical Scheme for General Relativistic Magnetohydrodynamics. 2003, *Astrophys. J.*, **589**, 444, DOI: 10.1086/374594
- Gierliński, M. & Done, C., Black hole accretion discs: reality confronts theory. 2004, *Mon. Not. R. Astron. Soc.*, **347**, 885, DOI: 10.1111/j.1365-2966.2004.07266.x
- Gierliński, M., Zdziarski, A. A., Poutanen, J., et al., Radiation mechanisms and geometry of Cygnus X-1 in the soft state. 1999, *Mon. Not. R. Astron. Soc.*, **309**, 496, DOI: 10.1046/j.1365-8711.1999.02875.x
- Goluchová, K., Török, G., Šrámková, E., et al., Mass of the active galactic nucleus black hole XMMUJ134736.6+173403. 2019, *A&A*, **622**, L8, DOI: 10.1051/0004-6361/201834774
- Goodman, J., Narayan, R., & Goldreich, P., The stability of accretion tori. II - Non-linear evolution to discrete planets. 1987, *Mon. Not. R. Astron. Soc.*, **225**, 695, DOI: 10.1093/mnras/225.3.695
- Gou, L., McClintock, J. E., Reid, M. J., et al., The Extreme Spin of the Black Hole in Cygnus X-1. 2011, *Astrophys. J.*, **742**, 85, DOI: 10.1088/0004-637X/742/2/85
- Gronkiewicz, D. & Różańska, A., Warm and thick corona for a magnetically supported disk in galactic black hole binaries. 2020, *Astron. Astrophys.*, **633**, A35, DOI: 10.1051/0004-6361/201935033
- Harten, A., Lax, P., & van Leer, B., On Upstream Differencing and Godunov-Type Schemes for Hyperbolic Conservation Laws. 1983, *SIAM Rev.*, **25**, 35
- Hartle, J. B. & Thorne, K. S., Slowly Rotating Relativistic Stars. II. Models for Neutron Stars and Supermassive Stars. 1968, *APJ*, **153**, 807, DOI: 10.1086/149707
- Hasinger, G. & van der Klis, M., Two patterns of correlated X-ray timing and spectral behaviour in low-mass X-ray binaries. 1989, *Astron. Astrophys.*, **225**, 79
- Hawley, J. F., Guan, X., & Krolik, J. H., Assessing Quantitative Results in Accretion Simulations: From Local to Global. 2011, *Astrophys. J.*, **738**, 84, DOI: 10.1088/0004-637X/738/1/84
- Hawley, J. F., Richers, S. A., Guan, X., & Krolik, J. H., Testing Con-



- vergence for Global Accretion Disks. 2013, *Astrophys. J.*, **772**, 102, DOI: 10.1088/0004-637X/772/2/102
- Hills, J. G., Possible power source of Seyfert galaxies and QSOs. 1975, *Nature*, **254**, 295, DOI: 10.1038/254295a0
- Horák, J., A possible mechanism for QPOs modulation in neutron star sources. 2005, *Astronomische Nachrichten*, **326**, 845, DOI: 10.1002/asna.200510425
- Horák, J., Abramowicz, M. A., Karas, V., & Kluzniak, W., Of NBOs and kHz QPOs: a Low-Frequency Modulation in Resonant Oscillations of Relativistic Accretion Disks. 2004, *Publ. Astron. Soc. Jpn*, **56**, 819, DOI: 10.1093/pasj/56.5.819
- Horák, J., Abramowicz, M. A., Kluzniak, W., Rebusco, P., & Török, G., Internal resonance in nonlinear disk oscillations and the amplitude evolution of neutron-star kilohertz QPOs. 2009, *A&A*, **499**, 535, DOI: 10.1051/0004-6361/200810740
- Horák, J. & Karas, V., Twin-peak quasiperiodic oscillations as an internal resonance. 2006, *Astron. Astrophys.*, **451**, 377, DOI: 10.1051/0004-6361:20054039
- Horák, J. & Lai, D., Corotation resonance and overstable oscillations in black hole accretion discs: general relativistic calculations. 2013, *Mon. Not. R. Astron. Soc.*, **434**, 2761, DOI: 10.1093/mnras/stt1120
- Huang, J., Jiang, Y.-F., Feng, H., et al., Global 3D Radiation Magnetohydrodynamic Simulations of Accretion onto a Stellar-mass Black Hole at Sub- and Near-critical Accretion Rates. 2023, *The Astrophysical Journal*, **945**, 57, DOI: 10.3847/1538-4357/acb6fc
- Ingram, A. & Done, C., A physical interpretation of the variability power spectral components in accreting neutron stars. 2010, *Mon. Not. R. Astron. Soc.*, **405**, 2447, DOI: 10.1111/j.1365-2966.2010.16614.x
- Ingram, A. R. & Motta, S. E., A review of quasi-periodic oscillations from black hole X-ray binaries: Observation and theory. 2019, *New Astron. Rev.*, **85**, 101524, DOI: 10.1016/j.newar.2020.101524
- Inogamov, N. A. & Sunyaev, R. A., Spread of matter over a neutron-star surface during disk accretion. 1999, *Astronomy Letters*, **25**, 269, DOI: 10.48550/arXiv.astro-ph/9904333
- Janiuk, A., Neutrino cooled disk in post-merger system studied via numerical GR MHD simulation with a composition-dependent equation of state. 2023, *arXiv e-prints*, arXiv:2303.18129, DOI: 10.48550/arXiv.2303.18129
- Jaroszyński, M., Abramowicz, M. A., & Paczyński, B., Supercritical accretion disks around black holes. 1980, *Acta Astron.*, **30**, 1
- Jiang, Y.-F., Stone, J. M., & Davis, S. W., On the Thermal Stability of Radiation-dominated Accretion Disks. 2013, *Astrophys. J.*, **778**, 65, DOI: 10.1088/0004-637X/778/1/65
- Jiang, Y.-F., Stone, J. M., & Davis, S. W., Super-Eddington Accretion Disks around

- Supermassive Black Holes. 2019, *ApJ*, **880**, 67, DOI: 10.3847/1538-4357/ab29ff
- Kaaret, P., Feng, H., & Roberts, T. P., Ultraluminous X-Ray Sources. 2017, *Annu. Rev. Astron. Astrophys.*, **55**, 303, DOI: 10.1146/annurev-astro-091916-055259
- Karas, V., Quasi-Periodic Features Due to Clumps Orbiting around a Black Hole. 1999a, *Publ. Astron. Soc. Jpn*, **51**, 317, DOI: 10.1093/pasj/51.3.317
- Karas, V., Twin Peak Separation in Sources with Kilohertz Quasi-periodic Oscillations Caused by Orbital Motion. 1999b, *Astrophys. J.*, **526**, 953, DOI: 10.1086/308015
- Karas, V., Klimovičová, K., Lančová, D., et al. 2023, manuscript submitted for publication to *Contrib. Astron. Obs. Skalnaté Pleso*
- Karas, V., Vokrouhlický, D., & Polnarev, A. G., In the vicinity of a rotating black hole: a fast numerical code for computing observational effects. 1992, *Mon. Not. R. Astron. Soc.*, **259**, 569, DOI: 10.1093/mnras/259.3.569
- Kato, S., Resonant Excitation of Disk Oscillations by Warps: A Model of kHz QPOs. 2004, *Publ. Astron. Soc. Jpn*, **56**, 905, DOI: 10.1093/pasj/56.5.905
- Kato, S. & Fukue, J., Trapped Radial Oscillations of Gaseous Disks around a Black Hole. 1980, *Publ. Astron. Soc. Jpn*, **32**, 377
- Kato, S., Fukue, J., & Mineshige, S. 2008, *Black-Hole Accretion Disks: Towards a New Paradigm* (Kyoto University Press)
- Kato, S. & Machida, M., A possible origin of kilohertz quasi-periodic oscillations in low-mass X-ray binaries. 2020, *Publ. Astron. Soc. Jpn*, **72**, 38, DOI: 10.1093/pasj/psaa019
- Kerr, R. P., Gravitational Field of a Spinning Mass as an Example of Algebraically Special Metrics. 1963, *Phys. Rev. Lett*, **11**, 237, DOI: 10.1103/PhysRevLett.11.237
- Kerr, R. P. & Schild, A., Republication of: A new class of vacuum solutions of the Einstein field equations. 2009, *General Relativity and Gravitation*, **41**, 2485, DOI: 10.1007/s10714-009-0857-z
- Kluźniak, W., Resonance model for high-frequency QPOs in white dwarfs, neutron stars and black holes. 2008, *New Astron. Rev.*, **51**, 841, DOI: 10.1016/j.newar.2008.03.014
- Kluźniak, W. & Abramowicz, M. A., Strong-Field Gravity and Orbital Resonance in Black Holes and Neutron Stars — kHz Quasi-Periodic Oscillations (QPO). 2001, *Acta Physica Polonica B*, **32**, 3605
- Kluźniak, W. & Abramowicz, M. A., Parametric epicyclic resonance in black hole disks: QPOs in micro-quasars. 2002, *arXiv e-prints*, astro, DOI: 10.48550/arXiv.astro-ph/0203314
- Kluźniak, W., Abramowicz, M. A., Kato, S., Lee, W. H., & Stergioulas, N., Nonlinear Resonance in the Accretion Disk of a Millisecond Pulsar. 2004, *Astrophys. J. Lett.*, **603**, L89, DOI: 10.1086/383143

- Kluźniak, W. & Kita, D., Three-dimensional structure of an alpha accretion disk. 2000, *arXiv e-prints*, astro, DOI: 10.48550/arXiv.astro-ph/0006266
- Kluźniak, W., Michelson, P., & Wagoner, R. V., Determining the Properties of Accretion-Gap Neutron Stars. 1990, *Astrophys. J.*, **358**, 538, DOI: 10.1086/169006
- Komissarov, S. S., A Godunov-type scheme for relativistic magnetohydrodynamics. 1999, *Mon. Not. R. Astron. Soc.*, **303**, 343, DOI: 10.1046/j.1365-8711.1999.02244.x
- Kotrlová, A., Šrámková, E., Török, G., et al., Models of high-frequency quasi-periodic oscillations and black hole spin estimates in Galactic microquasars. 2020, *Astron. Astrophys.*, **643**, A31, DOI: 10.1051/0004-6361/201937097
- Lančová, D., Abarca, D., Kluźniak, W., et al., Puffy Accretion Disks: Sub-Eddington, Optically Thick, and Stable. 2019, *ApJ Letters*, **884**, L37, DOI: 10.3847/2041-8213/ab48f5
- Lančová, D., Yilmaz, A., Wielgus, M., et al., Spectra of puffy accretion discs: the kynbb fit. 2023, *Astronomische Nachrichten*, DOI: 10.1002/asna.20230023
- Lee, W. H., Abramowicz, M. A., & Kluźniak, W., Resonance in Forced Oscillations of an Accretion Disk and Kilohertz Quasi-periodic Oscillations. 2004, *Astrophys. J. Lett.*, **603**, L93, DOI: 10.1086/383245
- Levermore, C., Relating Eddington factors to flux limiters. 1984, *Journal of Quantitative Spectroscopy and Radiative Transfer*, **31**, 149 , DOI: [https://doi.org/10.1016/0022-4073\(84\)90112-2](https://doi.org/10.1016/0022-4073(84)90112-2)
- Li, L.-X., Zimmerman, E. R., Narayan, R., & McClintock, J. E., Multitemperature Blackbody Spectrum of a Thin Accretion Disk around a Kerr Black Hole: Model Computations and Comparison with Observations. 2005a, *Astrophys. J. Suppl. Ser.*, **157**, 335, DOI: 10.1086/428089
- Li, L.-X., Zimmerman, E. R., Narayan, R., & McClintock, J. E., Multitemperature Blackbody Spectrum of a Thin Accretion Disk around a Kerr Black Hole: Model Computations and Comparison with Observations. 2005b, *Astrophys. J. Suppl. Ser.*, **157**, 335, DOI: 10.1086/428089
- Li, S.-L. & Begelman, M. C., Thermal Stability of a Thin Disk with Magnetically Driven Winds. 2014, *Astrophys. J.*, **786**, 6, DOI: 10.1088/0004-637X/786/1/6
- Lightman, A. P. & Eardley, D. M., Black Holes in Binary Systems: Instability of Disk Accretion. 1974, *The Astrophysical Journal*, **187**, L1, DOI: 10.1086/181377
- Lin, D., Remillard, R. A., & Homan, J., Spectral States of XTE J1701 - 462: Link Between Z and Atoll Sources. 2009, *Astrophys. J.*, **696**, 1257, DOI: 10.1088/0004-637X/696/2/1257
- Liska, M., Tchekhovskoy, A., Ingram, A., & van der Klis, M., Bardeen-Peterson alignment, jets, and magnetic truncation in GRMHD simulations of tilted thin accretion discs. 2019, *Monthly Notices of the Royal Astronomical Society*, **487**, 550, DOI: 10.1093/mnras/stz834

- Liska, M. T. P., Chatterjee, K., Issa, D., et al., H-AMR: A New GPU-accelerated GRMHD Code for Exascale Computing with 3D Adaptive Mesh Refinement and Local Adaptive Time Stepping. 2022, *Astrophys. J. Suppl. Ser.*, **263**, 26, DOI: 10.3847/1538-4365/ac9966
- Löffler, F., Faber, J., Bentivegna, E., et al., The Einstein Toolkit: a community computational infrastructure for relativistic astrophysics. 2012, *Classical and Quantum Gravity*, **29**, 115001, DOI: 10.1088/0264-9381/29/11/115001
- Lynden-Bell, D., Galactic Nuclei as Collapsed Old Quasars. 1969, *Nature*, **223**, 690, DOI: 10.1038/223690a0
- Matuszková, M., Klimovičová, K., Urbancová, G., et al., Oscillations of non-slender tori in the external Hartle-Thorne geometry. 2022, *arXiv e-prints*, arXiv:2203.10653, DOI: 10.48550/arXiv.2203.10653
- Matuszková, M., Török, G., Klimovičová, K., et al. in preparation, in preparation
- McClintock, J. E., Narayan, R., & Steiner, J. F., Black Hole Spin via Continuum Fitting and the Role of Spin in Powering Transient Jets. 2014, *Space Sci. Rev.*, **183**, 295, DOI: 10.1007/s11214-013-0003-9
- McKinney, J. C. & Gammie, C. F., A Measurement of the Electromagnetic Luminosity of a Kerr Black Hole. 2004, *Astrophys. J.*, **611**, 977, DOI: 10.1086/422244
- McKinney, J. C., Tchekhovskoy, A., Sadowski, A., & Narayan, R., Three-dimensional general relativistic radiation magnetohydrodynamical simulation of super-Eddington accretion, using a new code HARMRAD with M1 closure. 2014, *Mon. Not. R. Astron. Soc.*, **441**, 3177, DOI: 10.1093/mnras/stu762
- Méndez, M. & Belloni, T. M., High-Frequency Variability in Neutron-Star Low-Mass X-ray Binaries. 2021, in *Astrophysics and Space Science Library*, Vol. **461**, *Timing Neutron Stars: Pulsations, Oscillations and Explosions*, ed. T. M. Belloni, M. Méndez, & C. Zhang, 263–331
- Méndez, M., Karpouzas, K., García, F., et al., Coupling between the accreting corona and the relativistic jet in the microquasar GRS 1915+105. 2022, *Nature Astronomy*, **6**, 577, DOI: 10.1038/s41550-022-01617-y
- Middleditch, J. & Priedhorsky, W. C., Discovery of Rapid Quasi-periodic Oscillations in Scorpius X-1. 1986, *Astrophys. J.*, **306**, 230, DOI: 10.1086/164335
- Mignone, A., Bodo, G., Massaglia, S., et al., PLUTO: A Numerical Code for Computational Astrophysics. 2007, *Astrophys. J. Suppl. Ser.*, **170**, 228, DOI: 10.1086/513316
- Mihalas, D. & Mihalas, B. W. 1984, *Foundations of radiation hydrodynamics* (Dover Books on Physics)
- Miller, M. C., Lamb, F. K., & Cook, G. B., Effects of Rapid Stellar Rotation on Equation-of-State Constraints Derived from Quasi-periodic Brightness Oscillations. 1998, *Astrophys. J.*, **509**, 793, DOI: 10.1086/306533
- Mirabel, I. F., Rodriguez, L. F., Cordier, B., Paul, J., & Lebrun, F., A double-sided

- radio jet from the compact Galactic Centre annihilator 1E1740.7-2942. 1992, *Nature*, **358**, 215, DOI: 10.1038/358215a0
- Mishra, B., Fragile, P. C., Anderson, J., et al., The Role of Strong Magnetic Fields in Stabilizing Highly Luminous Thin Disks. 2022, *The Astrophysical Journal*, **939**, 31, DOI: 10.3847/1538-4357/ac938b
- Mishra, B., Fragile, P. C., Johnson, L. C., & Kluźniak, W., Three-dimensional, global, radiative GRMHD simulations of a thermally unstable disc. 2016, *MNRAS*, **463**, 3437, DOI: 10.1093/mnras/stw2245
- Mishra, B., Kluźniak, W., & Fragile, P. C., Breathing Oscillations in a Global Simulation of a Thin Accretion Disk. 2019, *Mon. Not. R. Astron. Soc.*, **483**, 4811, DOI: 10.1093/mnras/sty3124
- Mishra, B., Kluźniak, W., & Fragile, P. C., Relativistic, axisymmetric, viscous, radiation hydrodynamic simulations of geometrically thin discs. II. Disc variability. 2020, *Monthly Notices of the Royal Astronomical Society*, **497**, 1066, DOI: 10.1093/mnras/staa1848
- Mishra, B., Vincent, F. H., Manousakis, A., et al., Quasi-periodic oscillations from relativistic ray-traced hydrodynamical tori. 2017, *Mon. Not. R. Astron. Soc.*, **467**, 4036, DOI: 10.1093/mnras/stx299
- Misner, C. W., Thorne, K. S., & Wheeler, J. A. 1973, *Gravitation* (Princeton University Press)
- Miyamoto, S., Kitamoto, S., Hayashida, K., & Egoshi, W., Large Hysteretic Behavior of Stellar Black Hole Candidate X-Ray Binaries. 1995, *Astrophys. J. Lett.*, **442**, L13, DOI: 10.1086/187804
- Motta, S. E., Belloni, T., Stella, L., et al., Black hole mass and spin measurements through the relativistic precession model: XTE J1859+226. 2022, *Mon. Not. R. Astron. Soc.*, **517**, 1469, DOI: 10.1093/mnras/stac2142
- Motta, S. E., Kajava, J. J. E., Giustini, M., et al., Observations of a radio-bright, X-ray obscured GRS 1915+105. 2021, *Mon. Not. R. Astron. Soc.*, **503**, 152, DOI: 10.1093/mnras/stab511
- Motta, S. E., Munoz-Darias, T., Sanna, A., et al., Black hole spin measurements through the relativistic precession model: XTE J1550-564. 2014, *Mon. Not. R. Astron. Soc.*, **439**, L65, DOI: 10.1093/mnrasl/slt181
- Muñoz-Darias, T., Fender, R. P., Motta, S. E., & Belloni, T. M., Black hole-like hysteresis and accretion states in neutron star low-mass X-ray binaries. 2014, *Mon. Not. R. Astron. Soc.*, **443**, 3270, DOI: 10.1093/mnras/stu1334
- Narayan, R. & McClintock, J. E., Advection-dominated accretion and the black hole event horizon. 2008, *New Astron. Rev.*, **51**, 733, DOI: 10.1016/j.newar.2008.03.002
- Narayan, R., Zhu, Y., Psaltis, D., & Sądowski, A., HEROIC: 3D general relativistic radiative post-processor with comptonization for black hole accretion discs. 2016, *Mon.*

- Not. R. Astron. Soc.*, **457**, 608, DOI: 10.1093/mnras/stv2979
- Neumann, M., Avakyan, A., Doroshenko, V., & Santangelo, A., XRBCats: Galactic High Mass X-ray Binary Catalogue. 2023, *arXiv e-prints*, arXiv:2303.16137, DOI: 10.48550/arXiv.2303.16137
- Noble, S. C., Gammie, C. F., McKinney, J. C., & Del Zanna, L., Primitive Variable Solvers for Conservative General Relativistic Magnetohydrodynamics. 2006, *Astrophys. J.*, **641**, 626, DOI: 10.1086/500349
- Novikov, I. D. & Thorne, K. S., Astrophysics of black holes. 1973, in *Black Holes (Les Astres Occlus)*, 343–450
- Nowak, M. A. & Wagoner, R. V., Diskoseismology: Probing Accretion Disks. I. Trapped Adiabatic Oscillations. 1991, *Astrophys. J.*, **378**, 656, DOI: 10.1086/170465
- Nowak, M. A. & Wagoner, R. V., Diskoseismology: Probing Accretion Disks. II. G-Modes, Gravitational Radiation Reaction, and Viscosity. 1992, *Astrophys. J.*, **393**, 697, DOI: 10.1086/171538
- Oda, H., Machida, M., Nakamura, K. E., & Matsumoto, R., Thermal Equilibria of Magnetically Supported Black Hole Accretion Disks. 2009, *Astrophys. J.*, **697**, 16, DOI: 10.1088/0004-637X/697/1/16
- Paczynski, B., Possible relation between the X-ray QPO phenomenon and general relativity. 1987, *Nature*, **327**, 303, DOI: 10.1038/327303a0
- Page, D. N. & Thorne, K. S., Disk-Accretion onto a Black Hole. Time-Averaged Structure of Accretion Disk. 1974, *Astrophys. J.*, **191**, 499, DOI: 10.1086/152990
- Papaloizou, J. C. B. & Pringle, J. E., The dynamical stability of differentially rotating discs with constant specific angular momentum. 1984, *Mon. Not. R. Astron. Soc.*, **208**, 721, DOI: 10.1093/mnras/208.4.721
- Pareschi, L., Puppo, G., & Russo, G., Central Runge-Kutta Schemes for Conservation Laws. 2005, *SIAM Journal on Scientific Computing*, **26**, 979, DOI: 10.1137/S1064827503420696
- Parker, E. N., Dynamics of the Interplanetary Gas and Magnetic Fields. 1958, *Astrophys. J.*, **128**, 664, DOI: 10.1086/146579
- Parthasarathy, V., Kluźniak, W., & Čemeljić, M., MHD simulations of oscillating cusp-filling tori around neutron stars - missing upper kHz QPO. 2017, *Mon. Not. R. Astron. Soc.*, **470**, L34, DOI: 10.1093/mnrasl/slx070
- Paugnat, H., Lupsasca, A., Vincent, F. H., & Wielgus, M., Photon ring test of the Kerr hypothesis: Variation in the ring shape. 2022, *Astron. Astrophys.*, **668**, A11, DOI: 10.1051/0004-6361/202244216
- Penna, R. F., Kulkarni, A., & Narayan, R., A new equilibrium torus solution and GRMHD initial conditions. 2013a, *Astron. Astrophys.*, **559**, A116, DOI: 10.1051/0004-6361/201219666
- Penna, R. F., McKinney, J. C., Narayan, R., et al., Simulations of magne-

- tized discs around black holes: effects of black hole spin, disc thickness and magnetic field geometry. 2010, *Mon. Not. R. Astron. Soc.*, **408**, 752, DOI: 10.1111/j.1365-2966.2010.17170.x
- Penna, R. F., Sądowski, A., Kulkarni, A. K., & Narayan, R., The Shakura-Sunyaev viscosity prescription with variable  $\alpha$  (r). 2013b, *Mon. Not. R. Astron. Soc.*, **428**, 2255, DOI: 10.1093/mnras/sts185
- Penna, R. F., Sądowski, A., Kulkarni, A. K., & Narayan, R., The Shakura-Sunyaev viscosity prescription with variable  $\alpha$  (r). 2013c, *MNRAS*, **428**, 2255, DOI: 10.1093/mnras/sts185
- Penna, R. F., Sądowski, A., & McKinney, J. C., Thin-disc theory with a non-zero-torque boundary condition and comparisons with simulations. 2012, *Mon. Not. R. Astron. Soc.*, **420**, 684, DOI: 10.1111/j.1365-2966.2011.20084.x
- Penrose, R. & Floyd, R. M., Extraction of Rotational Energy from a Black Hole. 1971, *Nature Physical Science*, **229**, 177, DOI: 10.1038/physci229177a0
- Pétri, J., A toy model for coupling accretion disk oscillations to the neutron star spin. 2005, *Astron. Astrophys.*, **443**, 777, DOI: 10.1051/0004-6361:20054119
- Podgorny, J., Marra, L., Muleri, F., et al., The first X-ray polarimetric observation of the black hole binary LMC X-1. 2023, *arXiv e-prints*, arXiv:2303.12034, DOI: 10.48550/arXiv.2303.12034
- Porth, O., Chatterjee, K., Narayan, R., et al., The Event Horizon General Relativistic Magnetohydrodynamic Code Comparison Project. 2019, *Astrophys. J. Suppl. Ser.*, **243**, 26, DOI: 10.3847/1538-4365/ab29fd
- Porth, O., Olivares, H., Mizuno, Y., et al., The black hole accretion code. 2017, *Computational Astrophysics and Cosmology*, **4**, 1, DOI: 10.1186/s40668-017-0020-2
- Prather, B. S., Dexter, J., Moscibrodzka, M., et al., Comparison of Polarized Radiative Transfer Codes Used by the EHT Collaboration. 2023, *Astrophys. J.*, **950**, 35, DOI: 10.3847/1538-4357/acc586
- Remillard, R. A. & McClintock, J. E., X-Ray Properties of Black-Hole Binaries. 2006, *Annu. Rev. Astron. Astrophys.*, **44**, 49, DOI: 10.1146/annurev.astro.44.051905.092532
- Ressler, S. M., Tchekhovskoy, A., Quataert, E., & Gammie, C. F., The disc-jet symbiosis emerges: modelling the emission of Sagittarius A\* with electron thermodynamics. 2017, *Mon. Not. R. Astron. Soc.*, **467**, 3604, DOI: 10.1093/mnras/stx364
- Revnivtsev, M., Churazov, E., Gilfanov, M., & Sunyaev, R., New class of low frequency QPOs: Signature of nuclear burning or accretion disk instabilities? 2001, *Astron. Astrophys.*, **372**, 138, DOI: 10.1051/0004-6361:20010434
- Reynolds, C. S., Observational Constraints on Black Hole Spin. 2021, *Annu. Rev. Astron. Astrophys.*, **59**, 117, DOI: 10.1146/annurev-astro-112420-035022
- Rezzolla, L., Yoshida, S., & Zanotti, O., Oscillations of vertically integrated relativistic tori - I. Axisymmetric modes in a Schwarzschild space-time. 2003, *Mon. Not. R.*

- Astron. Soc.*, **344**, 978, DOI: 10.1046/j.1365-8711.2003.07023.x
- Rhoades, C. E. & Ruffini, R., Maximum Mass of a Neutron Star. 1974, *Phys. Rev. Lett.*, **32**, 324, DOI: 10.1103/PhysRevLett.32.324
- Róžańska, A., Czerny, B., Życki, P. T., & Pojmański, G., Vertical structure of accretion discs with hot coronae in active galactic nuclei. 1999, *Mon. Not. R. Astron. Soc.*, **305**, 481, DOI: 10.1046/j.1365-8711.1999.02425.x
- Róžańska, A., Malzac, J., Belmont, R., Czerny, B., & Petrucci, P. O., Warm and optically thick dissipative coronae above accretion disks. 2015, *Astron. Astrophys.*, **580**, A77, DOI: 10.1051/0004-6361/201526288
- Salpeter, E. E., Accretion of Interstellar Matter by Massive Objects. 1964, *The Astrophysical Journal*, **140**, 796, DOI: 10.1086/147973
- Schmidt, M., 3C 273 : A Star-Like Object with Large Red-Shift. 1963, *Nature*, **197**, 1040, DOI: 10.1038/1971040a0
- Schnittman, J. D., Interpreting the High-Frequency Quasi-periodic Oscillation Power Spectra of Accreting Black Holes. 2005, *Astrophys. J.*, **621**, 940, DOI: 10.1086/427646
- Schnittman, J. D. & Bertschinger, E., The Harmonic Structure of High-Frequency Quasi-periodic Oscillations in Accreting Black Holes. 2004, *Astrophys. J.*, **606**, 1098, DOI: 10.1086/383180
- Schnittman, J. D., Homan, J., & Miller, J. M., A Precessing Ring Model for Low-Frequency Quasi-periodic Oscillations. 2006a, *Astrophys. J.*, **642**, 420, DOI: 10.1086/500923
- Schnittman, J. D., Krolik, J. H., & Hawley, J. F., Light Curves from an MHD Simulation of a Black Hole Accretion Disk. 2006b, *Astrophys. J.*, **651**, 1031, DOI: 10.1086/507421
- Schnittman, J. D. & Rezzolla, L., Quasi-periodic Oscillations in the X-Ray Light Curves from Relativistic Tori. 2006, *Astrophys. J. Lett.*, **637**, L113, DOI: 10.1086/500545
- Schwarzschild, K., On the Gravitational Field of a Mass Point According to Einstein's Theory. 1916, *Abh. Konigl. Preuss. Akad. Wissenschaften Jahre 1906,92, Berlin, 1907*, **1916**, 189
- Seguin, F. H., The stability of nonuniform rotation in relativistic stars. 1975, *Astrophys. J.*, **197**, 745, DOI: 10.1086/153563
- Seward, F. D. & Charles, P. A. 2010, *Exploring the X-ray Universe* (Cambridge University Press)
- Shafee, R., McKinney, J. C., Narayan, R., et al., Three-Dimensional Simulations of Magnetized Thin Accretion Disks around Black Holes: Stress in the Plunging Region. 2008, *Astrophys. J. Lett.*, **687**, L25, DOI: 10.1086/593148
- Shakura, N. I. & Sunyaev, R. A., Black Holes in Binary Systems: Observational Ap-



- pearances. 1973, in IAU Symposium, Vol. **55**, *X- and Gamma-Ray Astronomy*, 155
- Shakura, N. I. & Sunyaev, R. A., A theory of the instability of disk accretion on to black holes and the variability of binary X-ray sources, galactic nuclei and quasars. 1976, *MNRAS*, **175**, 613, DOI: 10.1093/mnras/175.3.613
- Sądowski, A., Thin accretion discs are stabilized by a strong magnetic field. 2016, *Monthly Notices of the Royal Astronomical Society*, **459**, 4397, DOI: 10.1093/mnras/stw913
- Sądowski, A., Slim Disks Around Kerr Black Holes Revisited. 2009, *Astrophys. J. Suppl. Ser.*, **183**, 171, DOI: 10.1088/0067-0049/183/2/171
- Sądowski, A. & Narayan, R., Photon-conserving Comptonization in simulations of accretion discs around black holes. 2015, *Monthly Notices of the Royal Astronomical Society*, **454**, 2372, DOI: 10.1093/mnras/stv2022
- Sądowski, A. & Narayan, R., Three-dimensional simulations of supercritical black hole accretion discs - luminosities, photon trapping and variability. 2016, *Mon. Not. R. Astron. Soc.*, **456**, 3929, DOI: 10.1093/mnras/stv2941
- Sądowski, A., Narayan, R., McKinney, J. C., & Tchekhovskoy, A., Numerical simulations of super-critical black hole accretion flows in general relativity. 2014, *MNRAS*, **439**, 503, DOI: 10.1093/mnras/stt2479
- Sądowski, A., Narayan, R., Tchekhovskoy, A., et al., Global simulations of axisymmetric radiative black hole accretion discs in general relativity with a mean-field magnetic dynamo. 2015, *Mon. Not. R. Astron. Soc.*, **447**, 49, DOI: 10.1093/mnras/stu2387
- Sądowski, A., Narayan, R., Tchekhovskoy, A., & Zhu, Y., Semi-implicit scheme for treating radiation under M1 closure in general relativistic conservative fluid dynamics codes. 2013, *MNRAS*, **429**, 3533, DOI: 10.1093/mnras/sts632
- Sądowski, A., Wielgus, M., Narayan, R., et al., Radiative, two-temperature simulations of low-luminosity black hole accretion flows in general relativity. 2017, *MNRAS*, **466**, 705, DOI: 10.1093/mnras/stw3116
- Sod, G. A., Review. A Survey of Several Finite Difference Methods for Systems of Nonlinear Hyperbolic Conservation Laws. 1978, *Journal of Computational Physics*, **27**, 1, DOI: 10.1016/0021-9991(78)90023-2
- Sorathia, K. A., Reynolds, C. S., Stone, J. M., & Beckwith, K., Global Simulations of Accretion Disks. I. Convergence and Comparisons with Local Models. 2012, *Astrophys. J.*, **749**, 189, DOI: 10.1088/0004-637X/749/2/189
- Šprňa, R., Falanga, M., Török, G., et al. in preparation, in preparation
- Šrámková, E., Torkelsson, U., & Abramowicz, M. A., Oscillations of tori in the pseudo-Newtonian potential. 2007, *Astron. Astrophys.*, **467**, 641, DOI: 10.1051/0004-6361:20065979
- Stahl, A., Wielgus, M., Abramowicz, M., Kluźniak, W., & Yu, W., Eddington capture sphere around luminous stars. 2012, *Astron. Astrophys.*, **546**, A54, DOI:

10.1051/0004-6361/201220187

Stella, L. & Vietri, M., kHz Quasiperiodic Oscillations in Low-Mass X-Ray Binaries as Probes of General Relativity in the Strong-Field Regime. 1999, *Phys. Rev. Lett.*, **82**, 17, DOI: 10.1103/PhysRevLett.82.17

Straub, O., Bursa, M., Sądowski, A., et al., Testing slim-disk models on the thermal spectra of LMC X-3. 2011, *Astron. Astrophys.*, **533**, A67, DOI: 10.1051/0004-6361/201117385

Straub, O. & Šrámková, E., Epicyclic oscillations of non-slender fluid tori around Kerr black holes. 2009, *Classical and Quantum Gravity*, **26**, 055011, DOI: 10.1088/0264-9381/26/5/055011

Strohmayer, T. E., Jahoda, K., Giles, A. B., & Lee, U., Millisecond Pulsations from a Low-Mass X-Ray Binary in the Galactic Center Region. 1997, *Astrophys. J.*, **486**, 355, DOI: 10.1086/304522

Strohmayer, T. E., Zhang, W., Swank, J. H., et al., Millisecond X-Ray Variability from an Accreting Neutron Star System. 1996, *Astrophys. J. Lett.*, **469**, L9, DOI: 10.1086/310261

Stuchlík, Z., Kotrlová, A., & Török, G., Multi-resonance orbital model of high-frequency quasi-periodic oscillations: possible high-precision determination of black hole and neutron star spin. 2013, *Astron. Astrophys.*, **552**, A10, DOI: 10.1051/0004-6361/201219724

Tchekhovskoy, A. 2019, HARMPI: 3D massively parallel general relativistic MHD code, Astrophysics Source Code Library, record ascl:1912.014

Tchekhovskoy, A., Narayan, R., & McKinney, J. C., Efficient generation of jets from magnetically arrested accretion on a rapidly spinning black hole. 2011, *Mon. Not. R. Astron. Soc.*, **418**, L79, DOI: 10.1111/j.1745-3933.2011.01147.x

Tetarenko, B. E., Sivakoff, G. R., Heinke, C. O., & Gladstone, J. C., WATCHDOG: A Comprehensive All-sky Database of Galactic Black Hole X-ray Binaries. 2016, *Astrophys. J. Suppl. Ser.*, **222**, 15, DOI: 10.3847/0067-0049/222/2/15

Toro, E. 2009, *Riemann Solvers and Numerical Methods for Fluid Dynamics: A Practical Introduction* (Springer)

Török, G., Abramowicz, M. A., Kluźniak, W., & Stuchlík, Z., The orbital resonance model for twin peak kHz quasi periodic oscillations in microquasars. 2005, *Astron. Astrophys.*, **436**, 1, DOI: 10.1051/0004-6361:20047115

Török, G., Bakala, P., Stuchlík, Z., & Čech, P., Modeling the Twin Peak QPO Distribution in the Atoll Source 4U 1636-53. 2008, *Acta Astron.*, **58**, 1

Török, G., Goluchová, K., Horák, J., et al., Twin peak quasi-periodic oscillations as signature of oscillating cusp torus. 2016a, *Mon. Not. R. Astron. Soc.*, **457**, L19, DOI: 10.1093/mnras/slv196

Török, G., Goluchová, K., Horák, J., et al., Twin peak quasi-periodic oscillations as

- signature of oscillating cusp torus. 2016b, *Mon. Not. R. Astron. Soc.*, **457**, L19, DOI: 10.1093/mnras/slv196
- Török, G., Goluchová, K., Šrámková, E., Urbanec, M., & Straub, O., Time-scale of twin-peak quasi-periodic oscillations and mass of accreting neutron stars. 2019, *Mon. Not. R. Astron. Soc.*, **488**, 3896, DOI: 10.1093/mnras/stz1929
- Török, G., Kotrlová, A., Matuszková, M., et al., Simple analytic formula relating the mass and spin of accreting compact objects to their rapid X-ray variability. 2022, *arXiv e-prints*, arXiv:2203.04787
- Tóth, G., The  $\nabla \cdot \mathbf{B} = 0$  Constraint in Shock-Capturing Magnetohydrodynamics Codes. 2000, *Journal of Computational Physics*, **161**, 605, DOI: 10.1006/jcph.2000.6519
- Treves, A., Turolla, R., Zane, S., & Colpi, M., Isolated Neutron Stars: Accretors and Coolers. 2000, *Publ. Astron. Soc. Pac.*, **112**, 297, DOI: 10.1086/316529
- Urbancová, G., Urbanec, M., Török, G., et al., Epicyclic Oscillations in the Hartle-Thorne External Geometry. 2019, *Astrophys. J.*, **877**, 66, DOI: 10.3847/1538-4357/ab1b4c
- Urbanec, M., Miller, J. C., & Stuchlík, Z., Quadrupole moments of rotating neutron stars and strange stars. 2013, *Mon. Not. R. Astron. Soc.*, **433**, 1903, DOI: 10.1093/mnras/stt858
- Urry, C. M. & Padovani, P., Unified Schemes for Radio-Loud Active Galactic Nuclei. 1995, *Publ. Astron. Soc. Pac.*, **107**, 803, DOI: 10.1086/133630
- van der Klis, M., A review of rapid X-ray variability in X-ray binaries. 2004, *arXiv e-prints*, astro, DOI: 10.48550/arXiv.astro-ph/0410551
- Van der Klis, M., Rapid X-ray variability. 2006, in *Compact stellar X-ray sources*, **39**, 39
- van Leer, B., Towards the Ultimate Conservative Difference Scheme. V. A Second-Order Sequel to Godunov's Method. 1979, *Journal of Computational Physics*, **32**, 101, DOI: 10.1016/0021-9991(79)90145-1
- Vincent, F. H., Paumard, T., Gourgoulhon, E., & Perrin, G., GYOTO: a new general relativistic ray-tracing code. 2011, *Classical and Quantum Gravity*, **28**, 225011, DOI: 10.1088/0264-9381/28/22/225011
- Vincentelli, F. M., Neilsen, J., Tetarenko, A. J., et al., A shared accretion instability for black holes and neutron stars. 2023, *Nature*, **615**, 45, DOI: 10.1038/s41586-022-05648-3
- von Zeipel, H., The radiative equilibrium of a rotating system of gaseous masses. 1924, *Mon. Not. R. Astron. Soc.*, **84**, 665, DOI: 10.1093/mnras/84.9.665
- Šrámková, E., Matuszková, M., Klimovičová, K., et al., Oscillations of fluid tori around neutron stars. 2023, *Astronomische Nachrichten*, **344**, e20220114, DOI: 10.1002/asna.20220114
- Wang, Q. D., Nowak, M. A., Markoff, S. B., et al., Dissecting X-ray-Emitting

- Gas Around the Center of Our Galaxy. 2013, *Science*, **341**, 981, DOI: 10.1126/science.1240755
- Webster, B. L. & Murdin, P., Cygnus X-1-a Spectroscopic Binary with a Heavy Companion ? 1972, *Nature*, **235**, 37, DOI: 10.1038/235037a0
- White, C. J., Stone, J. M., & Gammie, C. F., An Extension of the Athena++ Code Framework for GRMHD Based on Advanced Riemann Solvers and Staggered-mesh Constrained Transport. 2016, *Astrophys. J. Suppl. Ser.*, **225**, 22, DOI: 10.3847/0067-0049/225/2/22
- Wielgus, M., Horák, J., Vincent, F., & Abramowicz, M., Reflection-asymmetric wormholes and their double shadows. 2020, *Phys. Rev. D*, **102**, 084044, DOI: 10.1103/PhysRevD.102.084044
- Wielgus, M., Lančová, D., Straub, O., et al., Observational properties of puffy discs: radiative GRMHD spectra of mildly sub-Eddington accretion. 2022, *Monthly Notices of the Royal Astronomical Society*, **514**, 780, DOI: 10.1093/mnras/stac1317
- Wijnands, R. 1999, Millisecond phenomena in X-ray binaries, PhD thesis, -
- Zdziarski, A. A., Johnson, W. N., & Magdziarz, P., Broad-band  $\gamma$ -ray and X-ray spectra of NGC 4151 and their implications for physical processes and geometry. 1996, *Mon. Not. R. Astron. Soc.*, **283**, 193, DOI: 10.1093/mnras/283.1.193
- Zhang, S. N., Cui, W., & Chen, W., Black Hole Spin in X-Ray Binaries: Observational Consequences. 1997, *Astrophys. J. Lett.*, **482**, L155, DOI: 10.1086/310705
- Zhang, S. N., Feroci, M., Santangelo, A., et al., eXTP: Enhanced X-ray Timing and Polarization mission. 2016, in Society of Photo-Optical Instrumentation Engineers (SPIE) Conference Series, Vol. **9905**, *Space Telescopes and Instrumentation 2016: Ultraviolet to Gamma Ray*, ed. J.-W. A. den Herder, T. Takahashi, & M. Bautz, 99051Q
- Zhu, Y. & Narayan, R., Thermal stability in turbulent accretion discs. 2013, *Mon. Not. R. Astron. Soc.*, **434**, 2262, DOI: 10.1093/mnras/stt1161
- Zhu, Y., Narayan, R., Sądowski, A., & Psaltis, D., HERO - A 3D general relativistic radiative post-processor for accretion discs around black holes. 2015, *Mon. Not. R. Astron. Soc.*, **451**, 1661, DOI: 10.1093/mnras/stv1046
- Życki, P. T., Done, C., & Smith, D. A., The 1989 May outburst of the soft X-ray transient GS 2023+338 (V404 Cyg). 1999, *Mon. Not. R. Astron. Soc.*, **309**, 561, DOI: 10.1046/j.1365-8711.1999.02885.x

## Part II

# Collection of papers

*Note: The published papers are replaced by the abstracts and DOIs in the arXiv version of this dissertation.*



# Paper 1: Puffy Accretion Disks: Sub-Eddington, Optically Thick, and Stable

DOI: [10.3847/2041-8213/ab48f5](https://doi.org/10.3847/2041-8213/ab48f5)

## Abstract

We report on a new class of solutions of black hole accretion disks that we found through radiative magnetohydrodynamic global simulations. The presented solution has a near-Eddington luminosity  $0.6L_{\text{Edd}}$ . It combines features of the canonical thin, slim and thick disk models but differs in crucial respects from each of them. By the density scale-height measure it appears to be thin, having a high density core near the equatorial plane of height  $\sim 0.1r$ , but it is sandwiched by a highly advective, turbulent, optically thick, Keplerian inflow of substantial geometrical thickness  $H \sim r$ . It is partially supported by an advected poloidal magnetic field with  $\beta \sim 0.5$ , which makes the disk thermally stable.





# Paper 2: Observational properties of puffy discs: radiative GRMHD spectra of mildly sub-Eddington accretion

DOI: [10.1093/mnras/stac1317](https://doi.org/10.1093/mnras/stac1317)

## Abstract

Numerical general relativistic radiative magnetohydrodynamic simulations of accretion disks around a stellar mass black hole with a luminosity above 0.5 of the Eddington value reveal their stratified, elevated vertical structure. We refer to these thermally stable numerical solutions as puffy disks. Above a dense and geometrically thin core of dimensionless thickness  $h/r \sim 0.1$ , crudely resembling a classic thin accretion disk, a puffed-up, geometrically thick layer of lower density is formed. This puffy layer corresponds to  $h/r \sim 1.0$ , with a very limited dependence of the dimensionless thickness on the mass accretion rate. We discuss the observational properties of puffy disks, in particular the geometrical obscuration of the inner disk by the elevated puffy region at higher observing inclinations, and collimation of the radiation along the accretion disk spin axis, which may explain the apparent super-Eddington luminosity of some X-ray objects. We also present synthetic spectra of puffy disks, and show that they are qualitatively similar to those of a Comptonized thin disk. We demonstrate that the existing XSPEC spectral fitting models provide good fits to synthetic observations of puffy disks, but cannot correctly recover the input black hole spin. The puffy region remains optically thick to scattering; in its spectral properties the puffy disk roughly resembles that of a warm corona sandwiching the disk core. We suggest that puffy disks may correspond to X-ray binary systems of luminosities above 0.3 of the Eddington luminosity in the intermediate spectral states.



# Paper 3: Spectra of puffy accretion discs: the kynbb fit

DOI: [10.1002/asna.20230023](https://doi.org/10.1002/asna.20230023)

## Abstract

Puffy disc is a numerical model, expected to capture the properties of the accretion flow in X-ray black hole binaries in the luminous, mildly sub-Eddington state. We fit the `kerrbb` and `kynbb` spectral models in `XSPEC` to synthetic spectra of puffy accretion discs, obtained in general relativistic radiative magnetohydrodynamic simulations, to see if they correctly recover the black hole spin and mass accretion rate assumed in the numerical simulation. We conclude that neither of the two models is capable of correctly recovering the puffy disc parameters, which highlights a necessity to develop new, more accurate spectral models for the luminous regime of accretion in X-ray black hole binaries. We propose that such spectral models should be based on the results of numerical simulations of accretion.



# Paper 4: Models of high-frequency quasi-periodic oscillations and black hole spin estimates in Galactic microquasars

DOI: [10.1051/0004-6361/201937097](https://doi.org/10.1051/0004-6361/201937097)

## Abstract

We explore the influence of non-geodesic pressure forces that are present in an accretion disk on the frequencies of its axisymmetric and non-axisymmetric epicyclic oscillation modes. We discuss its implications for models of high frequency quasi-periodic oscillations (QPOs) that have been observed in the X-ray flux of accreting black holes (BHs) in the three Galactic microquasars, GRS 1915+105, GRO J1655–40 and XTE J1550–564. We focus on previously considered QPO models that deal with low azimuthal number epicyclic modes,  $|m| \leq 2$ , and outline the consequences for the estimations of BH spin,  $a \in [0, 1]$ . For four out of six examined models, we find only small, rather insignificant changes compared to the geodesic case. For the other two models, on the other hand, there is a fair increase of the estimated upper limit on the spin. Regarding the QPO model's falsifiability, we find that one particular model from the examined set is incompatible with the data. If the microquasar's spectral spin estimates that point to  $a > 0.65$  were fully confirmed, two more QPO models would be ruled out. Moreover, if two very different values of the spin, such as  $a \approx 0.65$  in GRO J1655–40 vs.  $a \approx 1$  in GRS 1915+105, were confirmed, all the models except one would remain unsupported by our results. Finally, we discuss the implications for a model recently proposed in the context of neutron star (NS) QPOs as a disk-oscillation-based modification of the relativistic precession model. This model provides overall better fits of the NS data and predicts more realistic values of the NS mass compared to the relativistic precession model. We conclude that it also implies a significantly higher upper limit on the microquasar's BH spin ( $a \sim 0.75$  vs.  $a \sim 0.55$ ).



# Paper 5: Simple Analytic Formula Relating the Mass and Spin of Accreting Compact Objects to Their Rapid X-Ray Variability

DOI: [10.3847/1538-4357/ac5ab6](https://doi.org/10.3847/1538-4357/ac5ab6)

## Abstract

Following the previous research on epicyclic oscillations of accretion disks around black holes (BHs) and neutron stars (NSs), a new model of high-frequency quasi-periodic oscillations (QPOs) has been proposed (CT model), which deals with oscillations of fluid in marginally overflowing accretion tori (i.e., tori terminated by cusps). According to preliminary investigations, the model provides better fits of the NS QPO data compared to the relativistic precession (RP) model. It also implies a significantly higher upper limit on the Galactic microquasars BH spin. A short analytic formula has been noticed to well reproduce the model's predictions on the QPO frequencies in Schwarzschild spacetimes. Here we derive an extended version of this formula that applies to rotating compact objects. We start with the consideration of Kerr spacetimes and derive a formula that is not restricted to a particular specific angular momentum distribution of the inner accretion flow, such as Keplerian or constant. Finally, we consider Hartle-Thorne spacetimes and include corrections implied by the NS oblateness. For a particular choice of a single parameter, our relation provides frequencies predicted by the CT model. For another value, it provides frequencies predicted by the RP model. We conclude that the formula is well applicable for rotating oblateness NSs and both models. We briefly illustrate application of our simple formula on several NS sources and confirm the expectation that the CT model is compatible with realistic values of the NS mass and provides better fits of data than the RP model.





# Paper 6: Oscillations of non-slender tori in the external Hartle-Thorne geometry

DOI: [10.48550/arXiv.2203.10653](https://doi.org/10.48550/arXiv.2203.10653)

## Abstract

We examine the influence of the quadrupole moment of a slowly rotating neutron star on the oscillations of non-slender accretion tori. We apply previously developed methods to perform analytical calculations of frequencies of the radial epicyclic mode of a torus in the specific case of the Hartle-Thorne geometry. We present here our preliminary results and provide a brief comparison between the calculated frequencies and the frequencies previously obtained assuming both standard and linearized Kerr geometry. Finally, we shortly discuss the consequences for models of high-frequency quasi-periodic oscillations observed in low-mass X-ray binaries.